J. Print Media Technol. Res. 9(2020)2
June 2020

2-2020

ISSN 2414-6250 (Online)
CODEN JPMTBI
UDC 665

Journal of Print and Media Technology Research

Scientific contributions

ISSN 2414-6250
9 772414 625001

Editor-in-Chief Gorazd Golob (Ljubljana)

Published by iarigai
www.iarigai.org
The International Association of Research Organizations for the Information, Media and Graphic Arts Industries

J. Print Media Technol. Res. 9(2020)2
June 2020
ISSN 2414-6250 (Online)
A print version is available on-demand
ISSN 2223-8905 (Print)

Journal of Print and Media Technology Research

A PEER-REVIEWED QUARTERLY

PUBLISHED BY
The International Association of Research Organizations
for the Information, Media and Graphic Arts Industries
Magdalenenstrasse 2, D-64288 Darmstadt, Germany
http://www.iarigai.org
journal@iarigai.org

A mission statement

To meet the need for a high quality scientific publishing platform in its field, the International Association of Research Organizations for the Information, Media and Graphic Arts Industries is publishing a quarterly peer-reviewed research journal.

The journal is fostering multidisciplinary research and scholarly discussion on scientific and technical issues in the field of graphic arts and media communication, thereby advancing scientific research, knowledge creation, and industry development. Its aim is to be the leading international scientific journal in the field, offering publishing opportunities and serving as a forum for knowledge exchange between all those interested in contributing to or learning from research in this field.

By regularly publishing peer-reviewed, high quality research articles, position papers, surveys, and case studies as well as review articles and topical communications, the journal is promoting original research, international collaboration, and the exchange of ideas and know-how. It also provides a multidisciplinary discussion on research issues within the field and on the effects of new scientific and technical developments on society, industry, and the individual. Thus, it intends to serve the entire research community as well as the global graphic arts and media industry.

The journal is covering fundamental and applied aspects of at least, but not limited to, the following topics:

Printing technology and related processes

- Conventional and special printing
- Packaging
- Fuel cells and other printed functionality
- Printing on biomaterials
- Textile and fabric printing
- Printed decorations
- Materials science
- Process control

Premedia technology and processes

- Colour reproduction and colour management
- Image and reproduction quality
- Image carriers (physical and virtual)
- Workflow and management

Emerging media and future trends

- Media industry developments
- Developing media communications value systems
- Online and mobile media development
- Cross-media publishing

Social impact

- Media in a sustainable society
- Environmental issues and sustainability
- Consumer perception and media use
- Social trends and their impact on media

Submissions to the Journal

Submissions are invited at any time and, if meeting the criteria for publication, will be rapidly submitted to peer-review and carefully evaluated, selected and edited. Once accepted and edited, the papers will be published as soon as possible.

✉ Contact the Editorial office: journal@iarigai.org

Journal of
Print and Media Technology
Research

2-2020

June 2020

J. Print Media Technol. Res. 9(2020)2, 59–130

Journal of Print and Media Technology Research is listed in:

Emerging Sources Citation Index

Scopus

Index Copernicus International

PiraBase (by Smithers Pira)

Paperbase (by Innventia and Centre Technique du Papier)

NSD – Norwegian Register for Scientific Journals, Series and Publishers

Printed in Slovenia by Collegium Graphicum, d. o. o. Ljubljana

Contents

Scientific contributions

Topicalities

Edited by Markéta Držková

A letter from the Editor

Gorazd Golob
Editor-in-Chief
E-mail: gorazd.golob@jpmtr.org
journal@iarigai.org

The present issue of the Journal comes at a time, despite different wishes and some predictions, marked by a pandemic. Fortunately, the authors, reviewers, and editors have been persistent, and this time we are publishing four papers.

The first two are classified as original scientific papers, as they are distinguished from the others by a strong theoretical basis and an original approach. The first paper discusses the mechanical behavior and loads of paper, what is interesting especially for experts who are researching the manipulation of several sheets of paper at the same time, and practical applicability of the study could be seen mainly in the field of bookbinding, which is rarely considered in research.

The second paper is devoted to the investigation of printing pad geometry, mainly the use of various methods for simulation and optimal determination of the shape of the key element in this widespread technique of indirect gravure printing.

The third article is a research paper and was chosen for publication despite some concerns due to the results of the experiment, based on which the authors conclude that the tested printed surface does not affect sound absorption, but this claim opens up some new challenges for future research.

The fourth, final paper is a case study. This is a result of unique, very extensive research, which would not be possible without strong industrial partner's support, access to the specially made cardboard with known characteristics, and a printing press in the otherwise not very widespread gravure cardboard printing technique equipped with appropriate measuring equipment. The challenges are mainly in conducting a similar study in a lab environment, where full reproducibility of the experiment can also be ensured.

In the Topicalities the Editor Markéta Držková (marketa.drzkova@jpmtr.org) is bringing news from Drupa, a new alliance of US printers, reports from European Intergraf and recent printing-related research projects from MIT and EU-funded Horizon 2020. In the Bookshelf, you can find an overview of books from the fields covering management, typography, intellectual property, history, new materials, and technologies beyond traditional printing.

Three doctoral theses are also presented in the Bookshelf. Chun-Ho Lin defended his thesis on perovskite synthesis, fabrication and characterization at the King Abdullah University in Thuwal, Kingdom of Saudi Arabia. At the TU Chemnitz, Germany, Chadha Bali defended her dissertation on the study of coffee-ring-effect used as self-assembly mechanism in inkjet printing of organic printed electronic elements. Stephan Behnke defended his thesis at the Technical University of Darmstadt, Germany. His research was oriented towards the optimization of the printing and manufacturing process of metal packaging.

In the Events section, a number of conferences, workshops, seminars, and other events are presented, however, many of them are postponed or adopted to the current situation with online sessions, access to tutorials, and some of them are even moved to new locations. Also some other changes can still occur.

The call for papers is open constantly and we received two or three manuscripts every month this year. In the preliminary assessment of suitability for publication, we follow the Journal's policy according to which only papers that are of high quality, interesting, showing interesting research results or open new dilemmas and questions are suitable for review, editing, and publication. I am pleased that, despite the relatively high standards for the acceptance and publication of submitted manuscripts, we are receiving more and more quality papers appropriate to fulfil our mission. Join us and submit the results of your research and scientific work for publication in the Journal. We will appreciate publishing them, of course after a successful review, audit, and editing process.

Ljubljana, June 2020

JPMTR 132 | 1910
DOI 10.14622/JPMTR-1910
UDC 676.2:538.3|53.07

Original scientific paper
Received: 2019-10-28
Accepted: 2020-05-28

An empirical model for describing the mechanical behavior of paper and paper stacks in the perpendicular to the in-plane direction

Jian Chen[1], *Dieter Spiehl*[2], *Edgar Dörsam*[2], *Arash Hakimi Tehrani*[2] *and Simon Weißenseel*[2]

[1] School of Mechanical Engineering, Yangzhou University,
Huayang Weststr. 196, 225127 Yangzhou, China
[2] Institute of Printing Science and Technology,
Technische Universität Darmstadt,
Magdalenenstr. 2, 64289 Darmstadt, Germany

chenjian.tud@hotmail.com
spiehl@idd.tu-darmstadt.de
doersam@idd.tu-darmstadt.de
arash.hakimi.t@gmail.com
simon.weissenseel@alcon.com

Abstract

The mechanical behavior of paper materials under compression in the out-of-plane direction is highly nonlinear. If the influence of the surface topography is not taken into account, the stress–strain curve of paper materials in the loading process is a typical example of materials with J-shaped compressive curves. When compression is released, the stress–strain curve in the unloading process is also nonlinear. The main purpose of this paper is to establish a suitable mathematical model and actualize the description of the compression curve for paper and paper stacks. The loading and unloading nonlinearities of paper stress–strain relations can be approximated by using different equations. In this paper, the loading curve of paper is calculated by using the sextic polynomial equation and the unloading curve is described by using the modified exponential function. All the used coefficients for determining the functions are expressed as the functions of the stress at the start point of unloading. The compressive behavior of paper under some given forces are also calculated by using the identified equation and verified by means of the experimental data. For multiple sheets, it is assumed that when the force is the same, the deformation of the paper stack is directly proportional to the number of sheets. Based on this assumption, the force–deformation relation of the paper stack is derived. The comparative analysis of the experimental results demonstrates the effectiveness of the description model.

Keywords: out-of-plane direction, loading and unloading stages, stress–strain relationship, force–deformation curve, paper and paper stacks

1. Introduction and background

The mechanical stress–strain curve of paper is obviously affected by many factors, such as: the surface roughness, temperature, humidity as well as compression speed, etc. The properties of paper have been studied in numerous papers. But until now, it is still very hard to build a unified model which can be perfectly used for paper or paper stack and consider all of these factors. According to different classification criteria, the paper models can be classified into various groups.

Depending on whether the surface topography is taken into account, the analysis models of paper can be divided into rough surface models and smooth solid models. Generally, the paper is modelled as smooth solid material; the ignorance of the surface roughness brings lots of convenience for analyzing the processes such as paper delivery and paper calendering (Eckstein, 2014, p. 140). An analytical model was developed by Litvinov and Farnood (2010) for the compression of coated substrates in a soft rolling nip, in which, the substrate was represented by a modified solid element. The surface topographical differences between the cross direction and the machine direction for newspaper and paperboard were investigated by Alam, et al. (2011). When compressing thin sheets, it is very important to be aware of the influence of surface roughness (Rättö, 2005). The surface topography plays an important role in obtaining the stress–strain curve of paper materials; different methods of calculating the contact area will lead to very different results (Chen, et al., 2016a). The influence of surface roughness was also discussed in some papers, for example, the paper surface topography under compression was studied by Teleman, et al. (2004). According to the surface topography, the paper body was considered as being composed of two rough surfaces and an internal structure (Schaffrath and Göttsching, 1991; Chen, Neumann and Dörsam, 2014), the force–deformation relationship of paper was derived by using the Newton formula.

Based on the law of the essential physical characteristic of materials, the models of paper materials can be divided into constitutive models (Ramasubramanian and Wang, 1999; Xia, Boyce and Parks, 2002; Stenberg, 2003) and non-constitutive models. For the constitutive models, the properties of paper such as elasticity, plasticity and viscosity were modelled by using spring, dry friction and dashpot elements, respectively (Agilar Ribeiro and Costa, 2007; Gavelin, 1949). According to those methods, the differences of these constitutive models mainly lie in the different combinations of these elements. A considerable number of free parameters have to be determined by doing experiments in these constitutive models. Moreover, most of these parameters are very difficult to be measured.

In addition, according to different research methods, the research of paper can also be classified as experimental, simulation or mathematical analysis, etc. Four different experimental methods were evaluated for characterizing the smoothness of the handsheets (Singh, 2008; Nygårds, et al., 2005; Pino and Pladellorens, 2009). Some references (Mäkelä and Östlund, 2003; Ramasubramanian and Wang, 2007; Nygårds, et al., 2005; Andersson, 2006, p. 73; Lavrykov, et al., 2012) attempted to establish the simulation model for paper and paperboard in finite element method (FEM) software. Creasing and folding of multiply paperboard were also simulated by Huang with co-workers (Huang and Nygårds, 2010; 2012; Huang, Hagman and Nygårds 2014). Hill (1950) established Hill material with isotropic hardening. An anisotropic in-plane and out-of-plane elasto-plasto continuum model for paperboard consistent with the laws of thermodynamics was built by Borgqvist with co-workers, the creasing (Borgqvist, et al., 2015) and folding (Borgqvist, et al., 2016) operations were studied and compared to experimental results. In addition, an elastic-plastic model and the cohesive zone model (CZM) was proposed by Li, Reese and Simon (2017) to simulate the paperboard creasing process. Chen et al. (2015) proposed that the simulation of paper in the perpendicular to the in-plane direction can be solved by using the gasket model and avoiding the difficult measurements required for obtaining the parameters in previous models.

Compared to the in-plane dimensions, the thickness of paper material is very thin. It may sometimes be hard to imagine the use for an out-of-plane material model (Stenberg, 2002, p. 18). However, the mechanical behavior of paper has a very close relationship with many operations in the papermaking or printing industries, such as paper calendering, folding, creasing, traditional printing, and so on. The research on multiple sheets is also closely related to many applications, such as the operations of moving and organizing of paper in the pre-printing stage, paper cutting, book binding and paper counting in the post-printing process, and so on. Most of these examples have been described in Stenberg (2002, p. 18) in detail. In these examples, the importance of the out-of-plane behavior is enhanced.

For multiple sheets, a characteristic equation for paper pile in exponential form was proposed by Pfeiffer (1981) and the *K1* and *K2* factors were measured for paper stacks. When the surface roughness of paper was taken into consideration (Schaffrath and Göttsching, 1991), the force–deformation behavior of paper stack was investigated. Based on the model proposed by Schaffrath and Göttsching (1991), a theoretical formula was built for paper pile (Arango Diaz, Pfirrmann and Schmitt, 2009) to show the relationship between height and number of sheets; the force–deformation behavior of multiple sheets was also investigated (Chen, et al., 2016b). However, the simulation work and the research about paper stacks are still not sufficient, and therefore should be one of the main research directions in the future.

According to the knowledge of the authors, the compressive curve of paper material is a typical example of materials with J-shaped stress–strain curves, which is very similar to gasket and biomaterials (DoITPoMS, 2004). The curve shows that initially, small increases in stress give large deformations, however, at larger deformations the material becomes stiffer and more difficult to be compressed. A mathematical description model for spiral wound gasket was proposed by Takaki and Fukuoka (2000), then the stress–strain relation for asbestos sheet gasket was proposed by Takaki and Fukuoka (2001) in the same way. After that, these models were widely used for calculating the stress–strain curve of gasket materials (Takaki and Fukuoka, 2002a, 2002b, 2003; Nagata, Shoji and Sawa, 2002; Fukuoka and Takaki, 2003; Fukuoka, et. al., 2007; Fukuoka, Nomura and Nishikawa, 2012), especially, for the FEM calculation of gasket materials. The same method was used in this paper for establishing the empirical model for paper materials.

The aim of this study is to establish the empirical model and actualize the description of the stress–strain curve of paper sheet under the out-of-plane compression.

By establishing the empirical model, the stress–strain behavior of paper under different compressive forces in the through-thickness direction will be deeply investigated. Based on the stress–strain relation, the model for describing the force–deformation curve of paper stacks will also be derived. Finally, a comparison of the modelling results will be carried out with the experimental data.

2. Materials and methods

2.1 Theoretical basis

The stress–strain curve of paper consists of two parts: the curve under loading condition and the curve under unloading condition. Because of the plasticity of the paper material, the analysis of the unloading curve is much more complicated than the loading curve, but anyway, both can be described by using curve fitting methods. Generally, the description models for J-shaped materials can be divided into linear and nonlinear models.

For the compression behavior of gasket material, Nagata, Shoji and Sawa (2002) proposed a simplified linear model, in which the nonlinearity of the gasket stress–strain relation was approximated by two elastic moduli in loading and unloading stages, respectively. The comparison of computing results between the simplified linear model and the nonlinear model was also provided. For the analysis of gasket stress distribution in bolted flange joints, the result of this simplified model gives a good agreement with the result of nonlinear model.

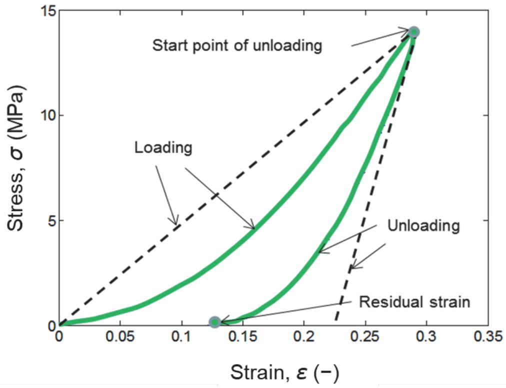

Figure 1: Typical stress–strain curve of paper shown in green color; the black dotted line is the simplified linear stress–strain curve of paper modelled with two elastic springs

The material behavior of paper in the out-of-plane direction (z-direction, ZD) can also be modelled with two linear springs (as shown in Figure 1), which provides convenient analysis of processes such as paper delivery and paper calendering (Eckstein, 2014, p. 140). As mentioned previously, a characteristic equation for paper pile in exponential form was proposed by Pfeiffer (1981), both of the stress–strain curves in loading and unloading stages were expressed by using exponential functions with coefficients of *K1* and *K2*.

In this paper, a polynomial function and a modified exponential function are used respectively for describing the stress–strain curve of paper on the loading condition and the unloading condition.

2.2 Numerical analysis

According to the model proposed by Takaki and Fukuoka (2000), the stress–strain curve of spiral wound gasket in the loading process can be described by using the sextic polynomial function:

$$\sigma = a_0 + a_1 \cdot \varepsilon + a_2 \cdot \varepsilon^2 + a_3 \cdot \varepsilon^3 + a_4 \cdot \varepsilon^4 + a_5 \cdot \varepsilon^5 + a_6 \cdot \varepsilon^6 \quad [\mathrm{MPa}] \qquad [1]$$

where σ and ε are the paper stress and strain, respectively. The a_i (i = 0, ..., 6) are constant values for identifying the polynomial function. Generally, $a_0 = 0$, but before the loading process, a preload is put on the specimen, so the corresponding value of a_0 is not 0.

For the unloading curve, the stress–strain relationship can be described by using the modified exponential function; the idea of constructing the model is to ensure that the established equation goes through the residual strain point (ε_r, 0):

$$\sigma = \alpha \cdot \exp(\beta \cdot \varepsilon) - \alpha \cdot \exp(\beta \cdot \varepsilon_r) \quad [\mathrm{MPa}] \qquad [2]$$

where:

$$\begin{aligned} \beta &= f_1(\varepsilon_{\mathrm{spu}}) = \mathrm{a} + \mathrm{b} \cdot \varepsilon_{\mathrm{spu}} + \mathrm{c} \cdot (\varepsilon_{\mathrm{spu}})^{\frac{1}{3}} \\ \varepsilon_r &= f_2(\varepsilon_{\mathrm{spu}}) = p \cdot \varepsilon_{\mathrm{spu}} + q \\ \alpha &= f_3(\varepsilon_{\mathrm{spu}}) = \frac{\sigma_{\mathrm{spu}}}{\exp(\beta \cdot \varepsilon_{\mathrm{spu}}) - \exp(\beta \cdot \varepsilon_r)} \end{aligned} \qquad [3]$$

In Equations [2] and [3], σ is the dependent variable and ε is the independent variable. The unloading curve is determined by the coefficients α and β. The σ_{spu} and $\varepsilon_{\mathrm{spu}}$ are the values of stress and strain at the start point of unloading, respectively. The value of σ_{spu} can be calculated according to Equation [1]. The a, b and c are the constants for identifying the relationship between β and $\varepsilon_{\mathrm{spu}}$. The p and q are the components of the equation between ε_r and $\varepsilon_{\mathrm{spu}}$. All of the coefficients α, β and ε_r can be expressed as a function of the independent variable $\varepsilon_{\mathrm{spu}}$.

Furthermore, the relationship between force and deformation can be converted from the stress–strain relation by using the following equations:

$$F = \sigma \cdot \pi \cdot \left(\frac{d_{\text{dia}}}{2}\right)^2 \quad [\text{N}] \qquad [4]$$
$$z = \varepsilon \cdot d_{\text{thi}} \quad [\text{mm}]$$

where, F is the force imposed on the paper specimen and z is the deformation of paper under the corresponding force F. The diameter of the cylindrical indenter is d_{dia}. The average thickness of paper is d_{thi}. According to Equations [1] to [4], the force–deformation relation of one sheet can be divided into two parts and expressed as:

$$F_{1,\,\text{loading}} = \left\{\sum_{i=0}^{6}\left[\left[a_i \cdot \left(\frac{z_{1,\,\text{loading}}}{d_{\text{thi}}}\right)^i\right]\right]\right\} \cdot \pi \cdot \left(\frac{d_{\text{dia}}}{2}\right)^2 \quad [\text{N}] \qquad [5]$$

$$F_{1,\,\text{unloading}} = \left\{\alpha \cdot \exp\left[\beta \cdot \left(\frac{z_{1,\,\text{unloading}}}{d_{\text{thi}}}\right)\right] - \alpha \cdot \exp(\beta \cdot \varepsilon_{\text{r}})\right\} \cdot \pi \cdot \left(\frac{d_{\text{dia}}}{2}\right)^2 \quad [\text{N}]$$

in which, $F_{1,\,\text{loading}}$ and $F_{1,\,\text{unloading}}$ are the forces in the loading stage and unloading stage, respectively, $z_{1,\,\text{loading}}$ and $z_{1,\,\text{unloading}}$ are the corresponding deformations, the subscript 1 corresponds to 1 sheet.

For multiple sheets, it is assumed that when the force is the same, the deformations of the paper stack $z_{n,\,\text{loading}}$ and $z_{n,\,\text{unloading}}$ are directly proportional to the number of sheets n. On the basis of this assumption, the force–deformation relation can be expressed as:

$$z^n_{\text{loading}} = k_{\text{loading}} \cdot n \quad [\text{mm}] \qquad [6]$$

$$z^1_{\text{unloading}} = k_{\text{unloading}} \cdot n \quad [\text{mm}]$$

In Equation [6], k_{loading} and $k_{\text{unloading}}$ are the slopes in the loading and unloading conditions, respectively, which are used for showing the relationship between deformation and number of paper sheets.

The values of k_{loading} and $k_{\text{unloading}}$ depend on the independent variable forces; when force changes, the values of k_{loading} and $k_{\text{unloading}}$ also change. The relationship between the slope and force can be expressed as the following equations:

$$k_{\text{loading}} = f_4\left(F^1_{\text{loading}}\right) \qquad [7]$$

$$k_{\text{unloading}} = f_5\left(F^1_{\text{unloading}}\right)$$

According to Equations [6] and [7], the force–deformation relation model of one sheet derived in Equation [5] can be extended to multiple sheets:

$$z_{n,\,\text{loading}} = f_4\left(F_{1,\,\text{loading}}\right) \cdot n \quad [\text{mm}] \qquad [8]$$
$$F_{n,\,\text{loading}} = F_{1,\,\text{loading}} \quad [\text{N}]$$
$$z_{n,\,\text{unloading}} = f_5\left(F_{1,\,\text{loading}}\right) \cdot n \quad [\text{mm}]$$
$$F_{n,\,\text{unloading}} = F_{1,\,\text{unloading}} \quad [\text{N}]$$

where $F_{n,\,\text{loading}}$ and $F_{n,\,\text{unloading}}$ are the forces applied to paper stack in the loading and unloading condition, respectively. For a better understanding, the force–deformation relation of multiple sheets can also be expressed as the converse equation of Equation [8]:

$$F_{\text{n, loading}} = f_4^{-1}\left(\frac{z_{\text{n, loading}}}{n}\right) \quad [\text{N}] \qquad [9]$$

$$F_{\text{n, unloading}} = f_5^{-1}\left(\frac{z_{\text{n, unloading}}}{n}\right) \quad [\text{N}]$$

2.3 Material and experimental setup

The paper used here for verifying the proposed model is the copy paper (Copy paper, DIN A4, 210 × 297 mm, 80 g/m^2), produced by the Steinbeis Paper GmbH in the year 2013. The actual average thickness is d = 84.7 µm.

The measurements were performed on the universal testing machine Zwick Z050, which can be utilized for strain, shear and bending tests with different substrates and machine components with high accuracy of the cross head speed (0.0005–2 000 mm/min), and position repetition accuracy (± 2 µm). The compression equipment is shown in Figure 2, which was designed by Kaulitz (2009, p. 179).

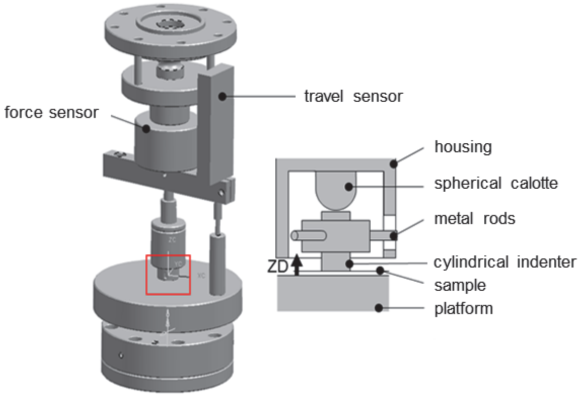

Figure 2: Test equipment for obtaining the force–deformation curve of the paper constructed by Kaulitz (Kaulitz, 2009, p. 179); the diameter of the cylindrical indenter (pressure head) is 6 mm

To eliminate the effect of climate conditions of the environment on the mechanical force–deformation behavior, the experimental studies were performed under standardized climatic conditions. The climate is specified in DIN 50014 and prescribed a range of 23 ± 0.5 °C for the temperature and a range of 50 ± 1.5 % for the relative humidity (Deutsche Institut für Normung, 2018).

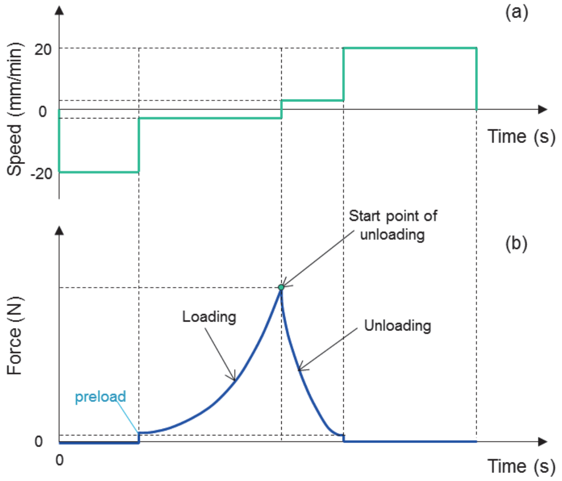

Figure 3: Schematic of the applied speed and force in loading cycle; (a) shows the changes of speed in a complete cycle, negative value means the speed is opposite to ZD direction, see Figure 2, (b) shows the corresponding forces; the strain rate is about 0.01

Figure 3 shows the settings of the loading speed and the corresponding force. At the beginning of the loading condition, the cylindrical indenter moves down from the original position at the speed of 20 mm/min, until the indenter comes into contact with the surface of the paper. The preload here is set to 1 N; when the change of force is 1 N, the compression process will begin with a velocity of 0.05 mm/min. After the force reaches the desired maximum force, the indenter will move up at the speed of 0.05 mm/min. When the force decreases to 1 N, the indenter returns back to the original position at the speed of 20 mm/min. The average thickness of paper is d = 84.7 µm, so, both in the loading and unloading process, the strain rate is equal to the loading speed divided by the thickness of paper; the value is about 0.01.

According to the size of the indenter (the diameter of the indenter is 6 mm) and paper thickness, the force–deformation curve can be easily transferred into the stress–strain curve by using Equation [4].

The obtained data of experiments can also be used for establishing the descriptive model for paper materials and comparing its results with the calculation results under different forces.

3. Results

3.1 Summary of the model for one sheet

For the loading process of one sheet, the stress–strain curve can be described by using the curve fitting method, by which, a set of experimental force–deformation data were needed. With the aid of suitable software, such as Matlab (Matlab Help, 2013), the constants which are used for identifying the loading curve of paper can be calculated automatically according to Equation [1]. All values of a_i coefficients are shown in Figure 4.

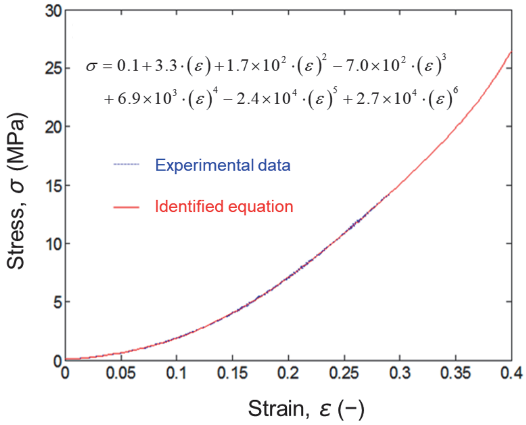

Figure 4: Stress–strain curve of paper in the loading condition; the blue curve is the experimental curve, the red one is the fitting curve by using the polynomial function; the coefficient of determination: R^2 = 1.0

From Figure 4, it can be seen that the stress–strain curve of paper in the loading stage can be described by using the polynomial function. The stress–strain curve under any desired strain can be obtained by the following identified equation.

$$\begin{aligned}\sigma &= 0.1 + 3.3\cdot\varepsilon + 1.7\times10^2\cdot\varepsilon^2 \\ &- 7.0\times10^2\cdot\varepsilon^3 + 6.9\times10^3\cdot\varepsilon^4 \\ &- 2.4\times10^4\cdot\varepsilon^5 + 2.7\times10^4\cdot\varepsilon^6 \quad [\text{MPa}]\end{aligned} \qquad [10]$$

For the unloading process, the model is built according to Equations [2] and [3]. There are three unknown variables, α, β and ε_r; the different values of ε_r under different forces can be directly obtained from the experimental data. Two more groups of point coordinates, (ε_{spu}, σ_{spu}) and (ε_m, σ_m), are selected for calculating the coefficients α and β. As shown in Figure 5, ε_{spu} and σ_{spu} are the strain and stress values at the start point of unloading. The point (ε_r, 0) represents the residual strain. The (ε_m, σ_m) is a random point selected in the unloading curve. With the help of these points, the values of α and β can be easily calculated.

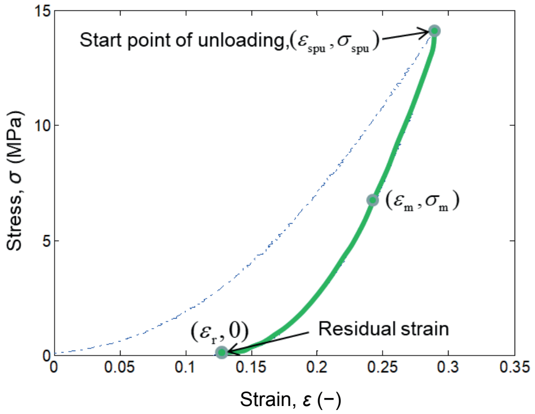

Figure 5: Selected points in the unloading stress–strain curve for calculating the components identifying the unloading function

3.2 Relationship between coefficient β and strain ε_{spu}

As mentioned above, three groups of point coordinates are needed for calculating the values of α and β. For instance, when the maximum force applied on the paper is 80 N, the value of ε_r can be obtained from the experiment. Then combined with the values at the start point of unloading (ε_{spu}, σ_{spu}) and the random point (ε_m, σ_m), the value of β can be calculated. The final calculation result of β under 80 N is 35.73. Other values of β can be calculated in the same way and the results are listed in Table 1.

Table 1: Values of ε_{spu} and β under different forces

Force (N)	ε_{spu} (−)	β (−)
20	0.0502	64.52
40	0.0880	43.03
80	0.1222	35.73
120	0.1547	25.97
200	0.2019	22.04
400	0.2904	14.36

According to the data obtained in Table 1, it can be observed that the values of β are decreasing with the increasing of ε_{spu} values; these discrete points have been plotted in the following coordinates in Figure 6.

As shown in Figure 6, the coefficient β is regarded as a dependent variable, which changes with the independent variable ε_y; the relation between them can be expressed by the following function:

$$\beta = f_1(\varepsilon_{spu}) = 206.64 + 339.76 \cdot \varepsilon_{spu} - 432.03 \cdot (\varepsilon_{spu})^{1/3} \quad [11]$$

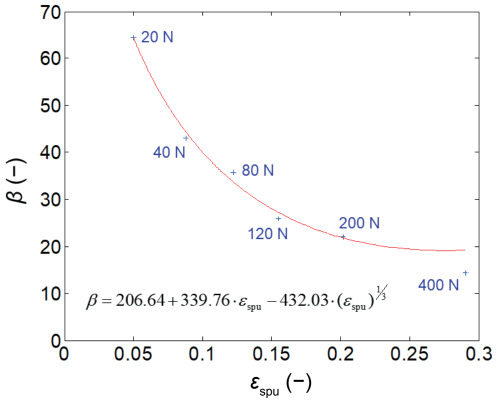

Figure 6: Relationship between the coefficients β and ε_{spu}; the discrete points are the points listed in Table 1, the red curve is calculated by using the curve fitting method

The function above consists of two parts: a linear polynomial function and a radical function. Here, the coefficients provided in Equation [3] are: a = 206.64, b = 339.76 and c = 432.03. The coefficient of determination is R^2 = 0.994. This function can also be expressed by using other functions, for example, the exponential function. The comparison between them will be implemented in the discussion chapter.

3.3 Relationship between strains ε_r and ε_{spu}

As mentioned previously, (ε_{spu}, σ_{spu}) represents the start point of unloading and (ε_r, 0) is the residual strain point. The values of ε_{spu} and ε_r can be directly obtained from the experimental data. The values under different forces are listed in Table 2.

Table 2: Values of ε_{spu} and ε_r under different forces, which have been obtained according to the experimental results

Force (N)	ε_{spu} (−)	ε_r (−)
20	0.0502	0.0024
40	0.0880	0.0159
80	0.1222	0.0272
120	0.1547	0.0460
200	0.2019	0.0756
400	0.2904	0.1216

On the basis of the data listed in Table 2, it can be seen that the values of ε_r are increasing with the increasing of ε_{spu} values; these discrete points were plotted in Figure 7. The values of ε_{spu} and ε_r are regarded as abscissa and ordinate, respectively.

From Figure 7, it can be seen that the relationship between ε_r and ε_{spu} is linear. By using the linear curve fitting method, the relationship between residual strain ε_r and the corresponding unloading strain ε_{spu} can be expressed as:

$$\varepsilon_r = f_2(\varepsilon_{spu}) = 0.49 \cdot \varepsilon_{spu} - 0.027 \qquad [12]$$

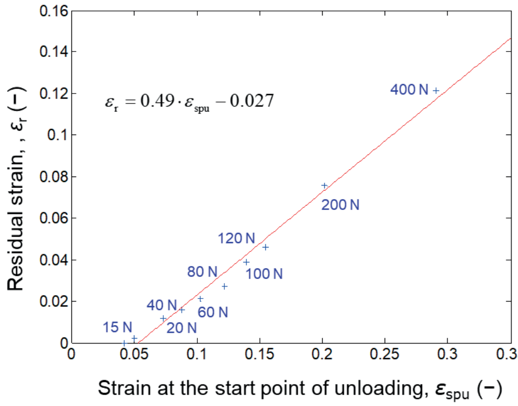

Figure 7: Relationship between the maximum strain and the residual strain; the red curve is calculated by using the linear curve fitting method

The coefficients of linear relation proposed in Equation [3] are: p = 0.49, q = −0.027. The coefficient of determination is R^2 = 0.990.

3.4 Relationship between coefficient α and strain ε_{spu}

According to Equation [3], the value of α is determined by the values of β and ε_r; the value of β can be calculated by using Equation [11], the value of ε_r is expressed as Equation [12]. The final function of α can be expressed as follows:

$$\alpha = f_3(\varepsilon_{spu}) = \frac{\varepsilon_{spu}}{\exp(\beta \cdot \varepsilon_{spu}) - \exp(\beta \cdot \varepsilon_r)} \qquad [13]$$

3.5 Relationship between $k_{loading}$ and $F_{loading}$

For multiple sheets, the description model was constructed on the assumption that when the force is the same, the deformation of paper stack ($z_{n,\ loading}$ and $z_{n,\ unloading}$) is proportional to the number of sheets n. This hypothesis was verified by the experimental data.

It can be seen from Figure 8 that, when the force is 100 N, the deformation of paper stacks at the start points of unloading shows a perfectly linear relationship with the sheet numbers.

For the curve fitting function, the coefficient of determination is R^2 = 0.999. For other forces, the experimental result is shown in Figure 9; the curve indicates linear relationship between deformation and sheet number.

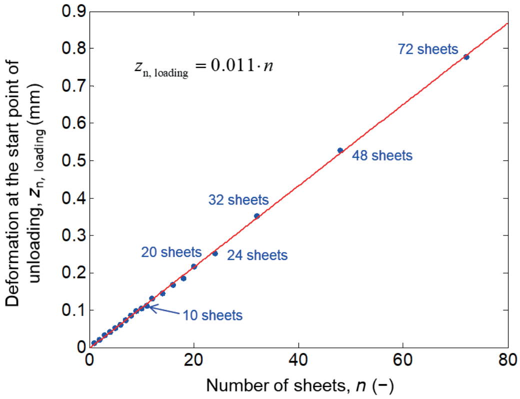

Figure 8: Deformation of different paper stacks under the same force; the force applied here is 100 N, the red curve is the linear curve fitting result

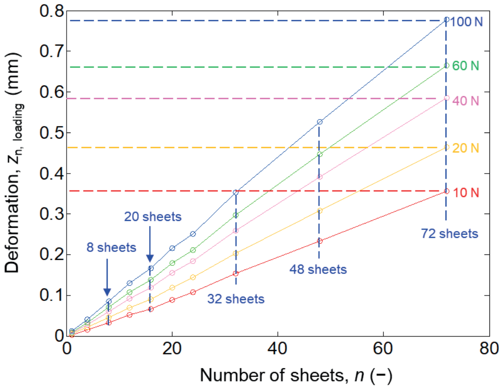

Figure 9: Experimental deformation of paper stacks under different loading forces

For different number of sheets, the statistical deformation value under different forces has been plotted in Figure 9, from which we can see the linear relationship between deformation and sheet number under different forces. The values of the slopes can be calculated and the values of forces and slopes are listed in Table 3.

Table 3: The values of $k_{loading}$ under seven groups of different loading forces

Group	$F_{loading}$ (N)	$k_{loading}$ (−)
1	5	0.0036
2	10	0.0050
3	20	0.0065
4	40	0.0082
5	60	0.0093
6	80	0.0100
7	100	0.0110

According to the listed slope values ($k_{loading}$) in Table 3, the values of slopes and forces were plotted in the same coordinate system; the value of $F_{loading}$ is regarded as the abscissa. The value of $k_{loading}$ is regarded as the ordinate. Then, the values of the slopes can be expressed as the function of forces.

Figure 10 displays that the value of k_{loading} is changing with force; the relationship between them can be approximated by using different functions.

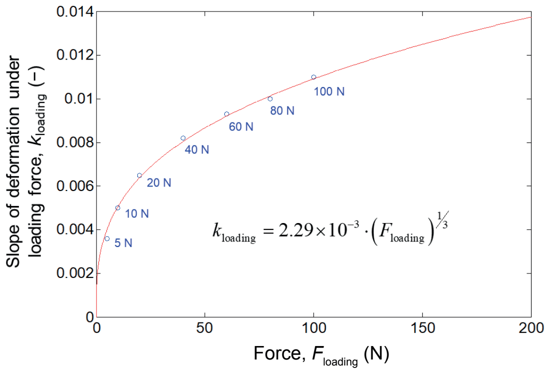

Figure 10: Relationship between the slopes and the forces in the loading condition; the discrete blue points are the values of $k_{loading}$ under different forces, the red curve is the approximation curve

A radical function was used here for describing the relationship between slope and force. The coefficient of the function can be calculated by using the curve fitting method. The coefficient of determination is $R^2 = 0.997$.

$$z_{n,\,\mathrm{loading}} = \left[2.29\times10^{-3}\cdot\left(F_{n,\,\mathrm{loading}}\right)^{1/3}\right]\cdot n\quad[\mathrm{mm}] \qquad [14]$$

3.6 Relationship between $k_{\mathrm{unloading}}$ and $F_{\mathrm{unloading}}$

The same as in the loading stage, for different forces, the slopes in the unloading stage are also constant values, which can be seen in Figure 11. However, because of the plasticity of the paper materials, a part of the deformation of paper in the unloading process cannot be recovered to the original shape, which is a non-reversible change of shape in response to applied force.

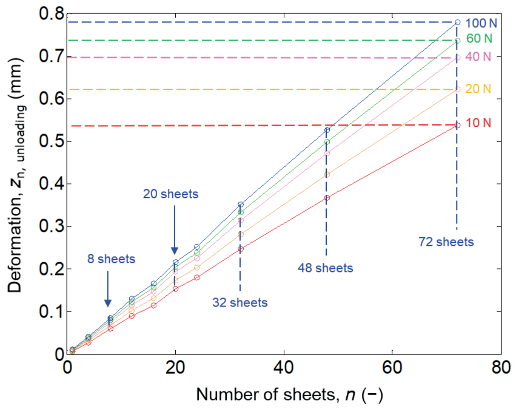

Figure 11: Experimental deformation of paper stacks under different unloading forces

The non-recoverable part shown in the force–deformation curve is called the residual deformation. The corresponding strain shown in the stress–strain curve is called the residual strain, which is shown in Figure 1 and Figure 5. Thus, in the unloading stage, when the force is decreasing to 0 N, the deformation of paper stacks cannot recover to 0 mm. But for simplifying the model, the influence from the residual deformation is ignored.

And the same, for different sheets, when the force is the same, the total deformation is directly proportional to the number of sheets; the values of the slopes under different groups of forces are shown in Table 4.

Table 4: The values of $k_{unloading}$ under seven groups of different loading forces

Group	$F_{\mathrm{unloading}}$ (N)	$k_{\mathrm{unloading}}$ (–)
1	5	0.0063
2	10	0.0076
3	20	0.0087
4	40	0.0098
5	60	0.0100
6	80	0.0110
7	100	0.0110

The values of slopes and forces listed in Table 4 are plotted in the same coordinate system; the values of $F_{\mathrm{unloading}}$ and $k_{\mathrm{unloading}}$ are regarded as the horizontal and ordinate axis, respectively. By using the curve fitting method, the values of the slopes can be expressed as the function of forces. The relation between $k_{\mathrm{unloading}}$ and $F_{\mathrm{unloading}}$ can be calculated according to the obtained function in Figure 12. The coefficients of the function are calculated by using the curve fitting method. Two radical functions are used for describing the relationship between slope and force. As mentioned above, the influence of the residual deformation is ignored; the values of slopes are regarded as changing from 0.

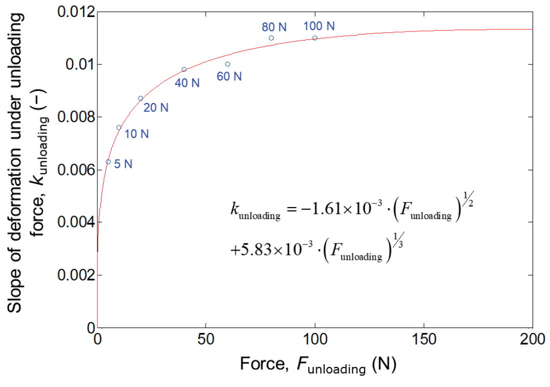

Figure 12: Relationship between the slopes and the forces in the unloading condition, the discrete blue points are the values of $k_{unloading}$ under $F_{unloading}$, the red curve is the fitting curve

The function of the unloading deformation can be expressed as:

$$z_{n,\,\text{unloading}} = \left[-1.61\times10^{-3}\cdot\left(F_{n,\,\text{unloading}}\right)^{1/2} + 5.83\times10^{-3}\cdot\left(F_{n,\,\text{unloading}}\right)^{1/3}\right]\cdot n \quad [\text{mm}] \qquad [15]$$

The coefficient of determination is $R^2 = 0.988$.

3.7 Final calculation model

The stress–strain relation of one sheet can be expressed by Equations [1] to [3] and [10] to [13]. The force–deformation relation of paper stack can be expressed by Equations [4] to [9] and [14] and [15].

3.8 Comparisons between the experimental data and the empirical results

In order to verify the applicability of the proposed model, some experiments on paper by using different maximum compression forces were performed; their results are shown in Figure 13. In the experimental process, the provided maximum forces were 20 N, 60 N, 80 N and 120 N.

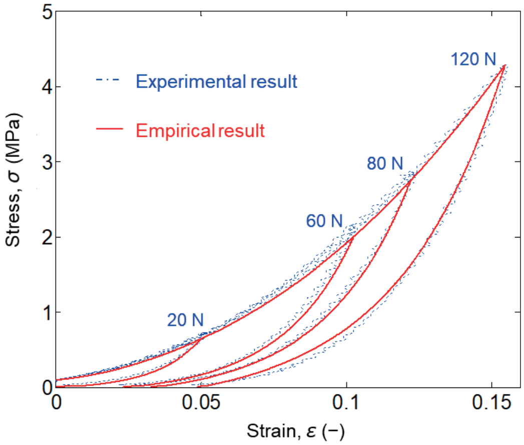

Figure 13: Comparisons between the experimental and empirical stress–strain curves of one sheet; the blue curves are the experimental results, the red curves were calculated by using the empirical model, using Equations [1] to[3] and [10] to [13]

Figure 13 shows the comparisons between the experimental and the calculated stress–strain curve of paper. The empirical and experimental results fit fairly well. The results show that this description model is capable of capturing the stress–strain behavior of paper at a wide range of strains.

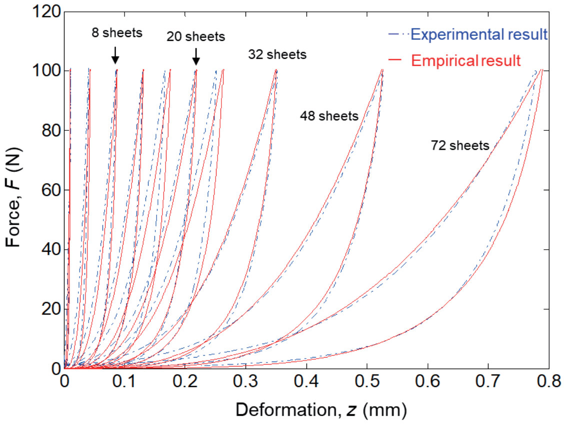

Figure 14: Comparisons between the experimental and empirical force–deformation curves of paper stacks; the blue curves are the experimental force–deformation data, the red curves were calculated by using the empirical model, Equations [4] to [9] and [14] and [15]

As shown in Figure 14, some experiments of multiple sheets (1, 4, 8, 12, 16, 20, 24, 32, 48, 72 sheets) with maximum force of 100 N were implemented. Comparison of the experimental results with empirical calculated results is shown in this figure. The deformations of paper stacks under the maximum force were selected for calculating the deviation.

The deviations for different numbers of sheets are listed in Table 5, with the largest values for 4, 16 and 24 sheets, but still within ±5 %. The model calculations give good fits to the experimental results.

Table 5: Comparisons of the force–deformation curves of paper pile between the experimental and empirical results, which is based on the deformation at the start point of unloading

Number of sheets	**Deformation at the start point of unloading (mm)**		**Deviation (%)**
	Experimental result	**Empirical result**	
4	0.042	0.044	−4.76
8	0.085	0.087	−2.35
12	0.130	0.131	−0.76
16	0.167	0.175	−4.79
20	0.216	0.219	−1.39
24	0.251	0.262	−4.38
32	0.352	0.350	+0.57
48	0.527	0.525	+0.38
72	0.778	0.787	−1.16

4. Discussion

4.1 Discussion about the stress–strain relation of one sheet

The loading process can be described by using not only polynomial function, but also exponential function defined in Equation [16] (Figure 15). The comparisons between them are discussed here.

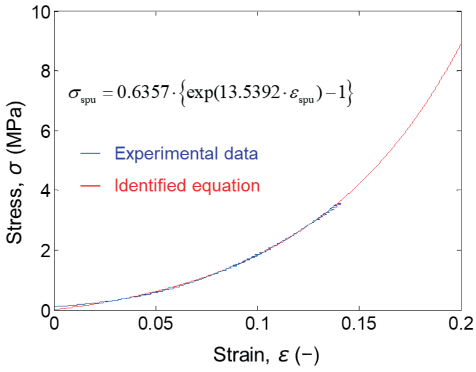

Figure 15: Stress–strain curve of paper in the loading stage; the blue curve is the experimental result, the red curve is calculated by using the exponential function

$$\sigma = p_1 \cdot [\exp(q_1 \cdot \varepsilon) - 1] \quad [\text{MPa}] \qquad [16]$$

where p_1 and q_1 are the coefficients for determining the loading exponential function, which can be calculated by using the curve fitting method; the result is shown in Equation [17]. The coefficient of determination is $R^2 = 0.998$.

$$\sigma_{\text{spu}} = 0.6357 \cdot [\exp(13.5392 \cdot \varepsilon_{\text{spu}}) - 1] \quad [\text{MPa}] \qquad [17]$$

In addition, the relationship between the coefficient β and unloading strain ε_{spu}, shown in Figure 16, can also be expressed by the exponential function.

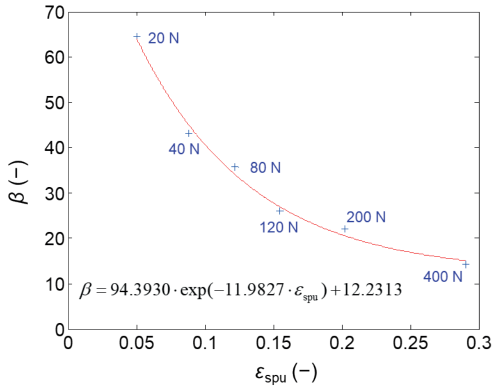

Figure 16: Relationship between the coefficients β and ε_{spu}. The discrete points are the points listed in Table 1, the red curve is the curve of the exponential function calculated by using the curve fitting method

The new function for β can be expressed as:

$$\beta = p_2 \cdot \exp(q_2 \cdot \varepsilon_{\text{spu}}) + c_2 \qquad [18]$$

where p_2, q_2 and c_2 are the coefficients for determining the unloading exponential function; the result is shown in Equation [19]. The coefficient of determination is $R^2 = 0.996$.

$$\beta = 94.3930 \cdot \exp(-11.9827 \cdot \varepsilon_{\text{spu}}) + 12.2313 \qquad [19]$$

When describing both the loading curve and the coefficient β using the exponential function, the stress–strain relation of paper can also be expressed by Equations [2] and [16] with coefficients described by Equations [12], [13], [17] and [19].

The calculation results were validated again by comparing with the experimental results.

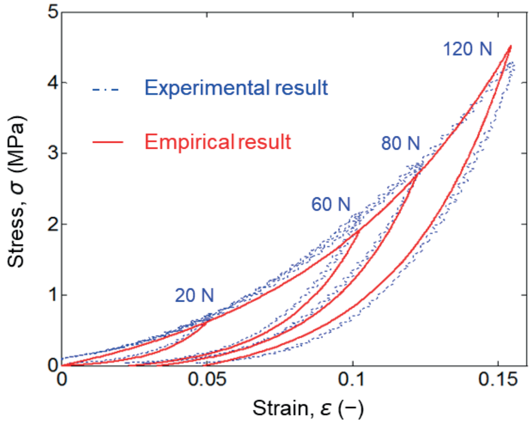

Figure 17: Comparisons between the experimental and the modified empirical stress–strain curves of paper, calculated by Equations [2], [12], [13], [16], [17] and [19]

As shown in Figure 17, the comparison results show that both of these two methods can be used for calculating the out-of-plane stress–strain relationship of paper materials; however, the fit with the former method is better (Figure 13). The calculated results based on polynomial function and exponential functions are compared in Figure 18.

It can be seen from Figure 18 that the difference between the results calculated based on the polynomial function and the exponential function is relatively small. Both of them can be used for calculating the stress–strain curve of a single sheet. Only when the stress is bigger than 4 MPa, the difference between the two curves increases.

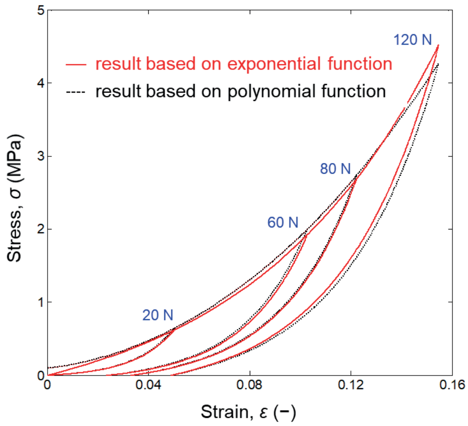

Figure 18: Comparisons of the results calculated based on polynomial function and exponential functions; the red curves are the results based on the exponential function (see Figure 17), the dashed black curves are the results based on the polynomial function, which are the red lines in Figure 13; the nominal area of the indenter is about 28.27 mm², a pressure of 3.5 MPa corresponds to about 100 N

4.2 Discussion about the force–deformation relation of multiple sheets

The described model can be used for calculating the force–deformation curve of multiple sheets. But for more sheets, the maximum number of sheets which can be calculated based on this model should be further investigated. In the following, we will discuss about the upper limit value of this model. More experiments were implemented to compare with the calculated results. The numbers of selected sheets are 72, 80, 90, 100, 110, 120, 130, 140 and 150. The comparative results between the experiment and calculation are shown in Figure 19.

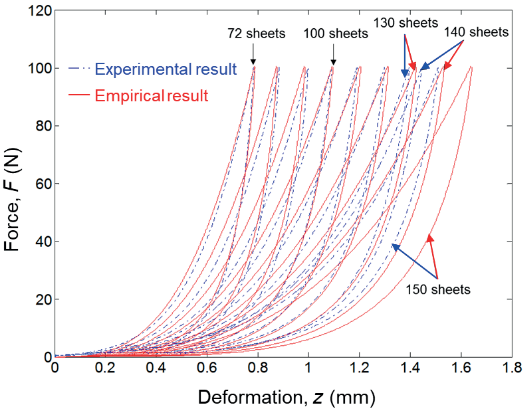

Figure 19: Comparisons of the experimental and empirical force–deformation curves of paper pile; the blue curves are the experimental data, the red curves are the force–deformation curves calculated by using the identified Equations [4] to [9] and [14] and [15]

From Figure 19 and Table 6, it can be seen that when the imposed force on the paper pile is 100 N, the maximum number of sheets which can be calculated by using this model is around 130 sheets. For further increasing the number of sheets, the deviation is increasing.

Table 6: Comparison of the force–deformation curves of paper pile between the experimental and empirical results, which is based on the deformation at the start point of unloading

Number of sheets	Deformation at the start point of unloading (mm)		Deviation (%)
	Experimental result	Empirical result	
72	0.78	0.79	−1.28
80	0.88	0.87	+1.14
90	1.00	0.98	+2.00
100	1.09	1.09	0.00
110	1.19	1.20	−0.84
120	1.30	1.31	−0.77
130	1.40	1.42	−1.43
140	1.44	1.52	−5.56
150	1.51	1.64	−8.60

In Table 6, the deviation of the deformation at the starting point of unloading has been calculated. According to Table 6, for paper piles with less than 130 sheets, the deviation between the experimental result and empirical result is smaller than 2.0 %, but when the number of sheets is 140, the deviation is increasing to about 5.6 %.

Based on the conclusion obtained above, we can redraw Figure 9 for more sheets and more forces; the new result is shown in Figure 20.

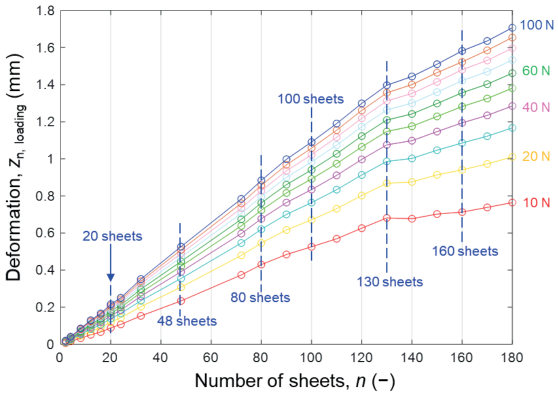

Figure 20: Experimental deformation of paper stacks under different loading forces

Figure 20 shows that when the sheet number is smaller than 130, the slopes of all curves are approximately constant values. But when the number of sheets is more than 130, the slopes will change to another constant values. This figure can also prove that 130 sheets is a turning point. When compressing paper stacks, what happens when the sheet number exceeds 130, it will be another interesting research subject. But as a speculation, the authors think that with increasing the sheet number, the stress really imposed on the paper lying in the lower layer is dispersed. When the number is more than 130, the remaining part of stack (the part more than 130) probably will not be affected by the force (or pressure). The maximum force imposed here is 100 N; if the force imposed on paper stack is bigger, the maximum number of sheets that can be calculated with the proposed model will be further extended.

5. Conclusions

The mechanical behavior of paper and paper stack in the out-of-plane direction was deeply investigated in the presented study. Three main aspects of mechanical behavior of paper and paper stacks were completed, which can be summarized as follows.

Firstly, the stress–strain description model of one sheet was established and the stress–strain curves of paper under some desired strains were obtained; the comparison between the experimental result and the calculation result shows the practicability of this model.

Secondly, the stress–strain model of one sheet can perfectly be extended to calculate the force–deformation behavior of paper stacks. This aspect is based on the assumption of direct relationship between the sheet number and deformation of paper stacks at same force. The verification result under 100 N shows that the maximum number of sheets which can be calculated by this model is around 130 sheets. For other forces, the force–deformation relationship in the loading stage can be calculated by using this model, but because of the deviation of the curve fitting methods, the accuracy of the unloading calculation is not enough.

Thirdly, the model proposed for one sheet can probably be extended to some other materials (other copy paper, newsprint, paperboard, etc.) with J-shaped force–deformation curves. Some specific studies related to mechanical behavior in out-of-plane direction can be carried out according to this method. However, compared to the thickness of paperboard, paper is much thinner and the structure of paper and paperboard is also very different, which lead to some differences between the studies of paper and paperboard.

Not all models which can be used for paperboard can also be well used for thin papers, and vice versa. Therefore, the applicability of the presented model to other materials has to be verified.

Acknowledgements

The authors gratefully acknowledge the financial support from the Jiangsu Science and Technology Department (Project Number: BK20190873) as well as the Lvyang Jinfeng plan for excellent doctors of Yangzhou city. All experiments mentioned in this paper were implemented by using the testing machine ZWICK Z050 in IDD (Institute of Printing Science and Technology, Technische Universität Darmstadt).

List of Abbreviations

a_i (i = 0, ..., 6)	coefficients of the polynomial loading function
a, b, c	coefficients of the equation between β and $\varepsilon_{\mathrm{spu}}$
d_{dia}	diameter of the indenter
d_{thi}	thickness of the paper
F	force
F_{loading}	force applied in the loading stage
$F_{\mathrm{unloading}}$	force applied in the unloading stage
$F_{1,\mathrm{\ loading}}$	force applied to one sheet in the loading stage
$F_{1,\mathrm{\ unloading}}$	force applied to one sheet in the unloading stage
$F_{n,\mathrm{\ loading}}$	force applied to n sheets in the loading stage
$F_{n,\mathrm{\ unloading}}$	force applied to n sheets in the unloading stage
k_{loading}	slope in loading stage used for showing the relationship between deformation and number of paper stacks
$k_{\mathrm{unloading}}$	slope in unloading stage used for showing the relationship between deformation and number of paper stacks
n	number of sheets
p, q	coefficients of the equation between ε_{r} and $\varepsilon_{\mathrm{spu}}$
p_1, q_1	coefficients of the modified loading function
p_2, q_2, c_2	coefficients of the new equation between β and $\varepsilon_{\mathrm{spu}}$
z	total deformation
$z_{1,\mathrm{\ loading}}$	deformation of one sheet in the loading stage
$z_{1,\mathrm{\ unloading}}$	deformation of one sheet in the unloading stage
$z_{n,\mathrm{\ loading}}$	deformation of n sheets in the loading stage
$z_{n,\mathrm{\ unloading}}$	deformation of n sheets in the unloading stage
α, β	coefficients of the exponential unloading function
σ	stress
σ_{spu}	stress at the start point of unloading
ε	strain
ε_{r}	residual strain
$\varepsilon_{\mathrm{spu}}$	strain at the start point of unloading

References

Agilar Ribeiro, H. and Costa, C.A.V., 2007. Modelling and simulation of the nonlinear behaviour of paper: a cellular materials approach. *Chemical Engineering Science,* 62(23), pp. 6696–6708. https://doi.org/10.1016/j.ces.2007.07.053.

Alam, A., Thim, J., Manuiskiy, A., O'Nils, M., Westland, C., Lindgren, J. and Linden, J., 2011. Mechanical pulping: investigation of the surface topographical differences between the cross direction and the machine direction for newspaper and paperboard. *Nordic Pulp & Paper Research Journal*, 26(4), pp. 468–475. https://doi.org/10.3183/npprj-2011-26-04-p468-475.

Andersson, T., 2006. *A small deformation model for the elasto-plastic behaviour of paper and paperboard*. Master's thesis. Lund University.

Arango Diaz, J.M., Pfirrmann, J. and Schmitt, N., 2009. *Konzept zur blattgenauen Mengenbestimmung eines Stapels blattförmigen Materials mittels Druckstempel*. Technische Universität Darmstadt.

Borgqvist, E., Wallin, M., Ristinmaa, M. and Tryding, J., 2015. An anisotropic in-plane and out-of-plane elasto-plastic continuum model for paperboard. *Composite Structures*, 126, pp. 184–195. https://doi.org/10.1016/j.compstruct.2015.02.067.

Borgqvist, E., Wallin, M., Tryding, J., Ristinmaa, M. and Tudisco, E., 2016. Localized deformation in compression and folding of paperboard. *Packaging Technology and Science,* 29(7), pp. 397–414. https://doi.org/10.1002/pts.2218.

Chen, J., Neumann, J. and Dörsam, E., 2014. Investigation on deformation behavior of paper in Z-direction. In: *Proceedings of the Progress in Paper Physics Seminar 2014.* Raleigh, North Carolina, USA, 8–12 September 2014.

Chen, J., Neumann, J., Sauer, H.M. and Dörsam, E., 2015. A new FEM simulation method of paper materials by using a gasket model. In: P. Gane, ed. *Advances in Printing and Madia Technology: Proceedings of the 42nd International Research Conference of iarigai.* Helsinki, Finnland, 6–9 September 2015. Darmstadt, Germany: iarigai.

Chen, J., Dörsam, E., Spiehl, D., Hakimi Tehrani, A. and Da, J., 2016a. Stress–strain behavior of paper affected by the actual contact area. In: *Proceedings of the Progress in Paper Physics Seminar 2016.* Darmstadt, Germany, 23–26 August, 2016.

Chen, J., Dörsam, E., Spiehl, D., Hakimi Tehrani, A., 2016b. Elastic model of paper stacks by considering the paper structure. *Nordic Pulp and Paper Research Journal*, 31(4), pp. 648–658. https://doi.org/10.3183/NPPRJ-2016-31-04-p648-658.

DoITPoMS*,* 2004. Descriptions of J-shaped curves*. DoITPoMS*, [online] University od Cambridge. Available at: <http://www.doitpoms.ac.uk/tlplib/bioelasticity/j-shaped-curves.php> [Accessed May 2020].

Deutsche Institut für Normung, 2018. DIN 50014:2018-04 *Normalklimate für Vorbehandlung und/oder Prüfung – Festlegungen.* Berlin: DIN.

Eckstein, M., 2014. *Instabilities and wear propagation in calenders: interactions with structural dynamics and contact kinematics*. Doctoral thesis. Technische Universität Darmstadt.

Fukuoka, T., Takaki, T., 2003. Finite element simulation of bolt-up process of pipe flange connections with spiral wound gasket. *Journal of Pressure Vessel Technology,* 125(4), pp. 371–378. https://doi.org/10.1115/1.1613304.

Fukuoka, T., Nomura, M., Hata, Y. and Nishikawa, T., 2007. Development of test equipment for measuring compression characteristics of sheet gaskets at elevated temperature. In: *Proceedings of the ASME PVP 2007/CREEP8 Pressure Vessels and Piping Conference and The Eighth International Conference on Creep and Fatigue at Elevated Temperatures*. San Antonio, Texas, USA, 22–26 July 2007.

Fukuoka, T., Nomura, M. and Nishikawa, T., 2012. Analysis of thermal and mechanical behavior of pipe flange connections by taking account of gasket compression characteristics at elevated temperature. *Journal of Pressure Vessel Technology,* 134(2): 021202. https://doi.org/10.1115/1.4005388.

Gavelin, G., 1949. The compressibility of newsprint. *Svensk Papperstidning*, 52, pp. 413–419.

Hill, R., 1950. *The mathematical theory of plasticity*. Oxford, United Kingdom: Clarendon Press.

Huang, H. and Nygårds, M., 2010. A simplified material model for finite element analysis of paperboard creasing. *Nordic Pulp and Paper Research Journal*, 25(4), pp. 505–512. https://doi.org/10.3183/npprj-2010-25-04-p502-509.

Huang, H. and Nygårds, M., 2012. Numerical investigation of paperboard forming. *Nordic Pulp and Paper Research Journal*, 27(2), pp. 211–225. https://doi.org/10.3183/NPPRJ-2012-27-02-p211-225.

Huang, H., Hagman, A. and Nygårds, M., 2014. Quasi static analysis of creasing and folding for three paperboards. *Mechanics of Materials*, 69(1), pp. 11–34. https://doi.org/10.1016/j.mechmat.2013.09.016.

Kaulitz, T., 2009. *Bilden von Schneidlagen unter Ausnutzung des Nipinduzierten Effekts für die Druckweiterverarbeitung*. Doctoral thesis. Technische Universität Darmstadt.

Lavrykov, S., Ramarao, B.V., Lindström, S.B. and Singh, K.M., 2012. 3D network simulations of paper structure. *Nordic Pulp and Paper Research Journal,* 27(2), pp. 256–263. https://doi.org/10.3183/npprj-2012-27-02-p256-263.

Li, Y., Reese, S. and Simon, J.-W., 2017. Modelling the anisotropic deformation and delamination in laminated paperboard. In*: Proceedings of the 21st International Conference on Composite Materials, ICCM21*. Xi'an, China, 20–25 August 2017.

Litvinov, V. and Farnood, R., 2010. Modeling of the compression of coated papers in a soft rolling nip. *Journal of Materials Science*. 45(1), pp. 216–226. https://doi.org/10.1007/s10853-009-3921-x.

MATLAB Help, 2013. *Image processing toolbox: user's guide – R2013b*. [pdf] MathWorks. Available at: <http://www.mathworks.com/downloads> [Accessed May 2020].

Mäkelä, P. and Östlund, S., 2003. Orthotropic elastic-plastic material model for paper materials. *International Journal of Solids and Structures*, 40(21), pp. 5599–5620. https://doi.org/10.1016/S0020-7683(03)00318-4.

Nagata, S., Shoji, Y. and Sawa, T., 2002. A simplified modelling of gasket stress–strain curve for FEM analysis in bolted flange joint design. In: *Proceedings of the ASME 2002 Pressure Vessels and Piping Conference.* Vancouver, BC, Canada, 5–9 August 2002. ASME, pp. 53–58. https://doi.org/10.1115/PVP2002-1082.

Nygårds, M., Hallbäck, N., Just, M. and Tryding, J., 2005. A finite element model for simulations of creasing and folding of paperboard. In: *Proceedings of the 2005 ABAQUS Users' Conference.* Stockholm, Sweden, 18–20 May 2005, pp 373–387.

Pfeiffer, J.D., 1981. Measurement of the K2 factor for paper. *Tappi Journal,* 64(4), pp. 105–106.

Pino, A. and Pladellorens, J., 2009. Measure of roughness of paper using speckle. In: P.S. Huang, T. Yoshizawa and K.G. Harding, eds. *Proceedings of SPIE Vol. 7432: Optical Inspection and Metrology for Non-Optics Industries, the International Society for Optical Engineering*, San Diego, California, USA, 2–6 August 2009. SPIE. https://doi.org/10.1117/12.825072.

Ramasubramanian, M. K. and Wang, Y.Y., 1999. Constitutive models for paper and other ribbon-like nonwovens – a literature review. In: R. Perkins, ed. *Mechanics of Cellulosic Materials, AMD-vol. 231, MD-vol. 85*. New York, USA: American Society of Mechanical Engineers, pp. 31–42.

Ramasubramanian, M.K. and Wang, Y., 2007. A computational micromechanics constitutive model for the unloading behavior of paper. *International Journal of Solids and Structures,* 44(22–23), pp. 7615–7632. https://doi.org/10.1016/j.ijsolstr.2007.05.002.

Rättö, P., 2005. The influence of surface roughness on the compressive behaviour of paper. *Nordic Pulp and Paper Research Journal,* 20(3), pp. 304–307. https://doi.org/10.3183/npprj-2005-20-03-p304-307.

Schaffrath, H.-J., and Göttsching, L., 1991. The behaviour of paper under compression in z-direction. In: *Proceedings of the 1991 International Paper Physics Conference*. Kona, Hawaii, USA, 22–26 September 1991. Atlanta, USA: TAPPI Press, pp. 489–510.

Singh, S.P., 2008. A comparison of different methods of paper surface smoothness evaluation. *BioResources,* 3(2), pp. 503–516.

Stenberg, N., 2002. *On the out-of-plane mechanical behaviour of paper materials*. Doctoral thesis. Royal Institute of Technology.

Stenberg, N., 2003. A model for the through-thickness elastic-plastic behaviour of paper. *International Journal of Solids and Structures,* 40(26), pp. 7483–7498. https://doi.org/10.1016/j.ijsolstr.2003.09.003.

Takaki, T. and Fukuoka, T., 2000. Bolt-up strategy for pipe flange connections using finite element analysis. In: *Proceedings of the PVP 2000 ASME ASME Pressure Vessels and Piping Conference: Analysis of Bolted Joints*. Seattle, WA, US, 23–27 July 2000. ASME, pp. 143–150.

Takaki, T. and Fukuoka, T., 2001. Finite element analyses of bolt-up operations for pipe flange connections. In: *Proceedings of the PVP 2001 ASME Pressure Vessels and Piping Conference: Analysis of Bolted Joints.* Atlanta, GA, USA, 23–26 July 2001. ASME, pp. 141–148.

Takaki, T. and Fukuoka, T., 2002a. Systematical FE analysis of bolt assembly process of pipe flange connections. In: *Proceedings of the PVP 2002 ASME Pressure Vessels and Piping Conference: Analysis of Bolted Joints.* Vancouver, BC, Canada, 5–9 August 2002. ASME, pp. 147–152. https://doi.org/10.1115/PVP2002-1092.

Takaki, T. and Fukuoka, T., 2002b. Three-dimensional finite element analysis of pipe flange connections: the case of using compressed asbestos sheet gasket. In: *Proceedings of the ASME 2002 Pressure Vessels and Piping Conference: Analysis of Bolted Joints.* Vancouver, BC, Canada, 5–9 August 2002. ASME, pp. 171–177. https://doi.org/10.1115/PVP2002-1095.

Takaki, T. and Fukuoka, T., 2003. Methodical guideline for bolt-up operation of pipe flange connections: a case using sheet gasket and spiral wound gasket. In: *Proceedings of the ASME 2003 Pressure Vessels and Piping Conference: Analysis of Bolted Joints.* Cleveland, Ohio, USA, 20–24 July 2003. ASME, pp. 23–30. https://doi.org/10.1115/PVP2003-1869.

Teleman, A., Östlund, C., Nordström, J.-E., Johansson, P.-Å. and Vomhoff, H., 2004. *Analysis of paper surface topography under compression: STFI report CW217*. Stockholm, Sweden: STFI.

Xia, Q.S., Boyce, M.C. and Parks, D. M., 2002. A constitutive model for the anisotropic elastic-plastic deformation of paper and paperboard. *International Journal of Solids and Structures,* 39(15), pp. 4053–4071. https://doi.org/10.1016/S0020-7683(02)00238-X.

JPMTR 133 | 1913
DOI 10.14622/JPMTR-1913
UDC 655.1:517.9+004.92

Original scientific paper
Received: 2019-12-11
Accepted: 2020-05-31

Investigation of printing pad geometry by using FEM simulation

Ahmad Al Aboud, Edgar Dörsam and Dieter Spiehl

Technische Universität Darmstadt,
Institute of Printing Science and Technology,
Magdalenenstr. 2, 64289 Darmstadt, Germany

aboud@idd.tu-darmstadt.de
doersam@idd.tu-darmstadt.de
spiehl@idd.tu-darmstadt.de

Abstract

Pad printing is an indirect gravure printing for printing on objects with complicated geometries or rough surfaces. Although pad printing is a proven and widely used printing process, there are few scientific studies on the shape and hardness of printing pads and their influence on printing quality. The shape and hardness of printing pads are therefore still determined today by experience. Even in the age of digitalization, the manufacturing of printing pads is still a manual process. So far, no modern tools are known to support this manufacturing process. In this paper, using simulations with commercially available finite element method (FEM) software (Abaqus) or open source software (Salome-Meca) as possible development tools for silicone rubber printing pads is investigated. The FEM simulation of this hyperelastic material requires various input parameters such as material model, special material parameters as well as mesh types and sizes. This paper shows how these parameters are determined, which material tests are necessary and how sensitive the simulation result is to these input parameters. Based on the comparison with experimental data, the results show that silicone rubber printing pads with small deformations can be simulated very well with both the commercial FEM software Abaqus and the free open source FEM software Salome-Meca. Mooney–Rivlin or the polynomial material equations are used. Finally, a workflow is shown with which the geometry of a printing pad can be evaluated and optimized.

Keywords: pad printing, pad geometry, silicone rubber, hyperelastic material, mesh

1. Introduction and background

Indirect gravure printing is a printing process in which a pad transfers the ink from an engraved printing form (cliché) to a substrate. In some literature, it is called pad printing (Hahne, 2001; Kipphan, 2001). The indirect gravure printing method has an acceptable accuracy and a resolution of 20 μm to print, e.g., high accuracy electronic devices (Pudas, Hagberg and Leppävuori, 2004).

Figure 1: Examples of products printed with pad printing; photo from Hakimi Tehrani (2018)

One of the main advantages of pad printing is that it can be used to print on three-dimensional surfaces and products of all shapes and sizes. It does not matter whether the articles are curved or have an uneven surface, with this printing process a high-quality print is nevertheless achieved. If we have to print fine motifs, we will find that the resolution of pad printing is much better than that of screen printing (Tampo Canada, 2018). Figure 1 shows printed examples made by pad printing technology.

The printing pads are made of a liquid mixture of silicone rubber and silicone oil. The shape of the printing pad should be suitable for the substrate to be printed on. This is why there are countless different qualities, sizes, shapes and hardnesses of printing pads on the market. The mixing ratio of silicone rubber and silicone oil determines the surface free energy and the surface hardness of the printing pad, measured in Shore A. Hardnesses from 0 Shore A (soft) to 18 Shore A (very hard) are common. The print quality varies depending on the shape of the substrate to be printed, the printing pad and its hardness (Al Aboud, et al., 2018). For almost every special printing task it is possible to produce a suitable printing pad to optimize the printing result. Therefore, every manufacturer of printing pads should have several hundred different printing pads on offer (Kipphan, 2001). Today, the choice of printing pad form and hardness is based completely on the expert knowledge of those involved.

In this study the material of the printing pad is described as hyperelastic material. Hyperelastic materials have a clearly different mechanical behavior than, for example, metals, which are also called linear elastic materials. The differences between hyperelastic and linear elastic materials are summarized in Table 1. A more detailed description with explanations can be found in Antman (2004).

Table 1: Difference between hyperelastic and linear elastic material; where σ is tensile stress, E is Young's modulus, ε is extensional strain

Linear elastic material (metal)	**Hyperelastic material (printing pad)**
$\sigma = E \cdot \varepsilon$ Simple linear relationship between stress and strain.	$\sigma \neq E \cdot \varepsilon$ Complex mathematical equations are used (see section 2).
Very large forces of 9.9 kN to 29.9 kN (1 to 3 tons) cause small deformations.	Small forces of 40 N to 350 N cause large deformations.
Take on a permanently deformed shape after unloading from the plastic deformation.	The material returns to the original form after unloading.
Hardness is measured in Vickers (HV) or Rockwell (HR).	Hardness is measured in Shore A.

In previous investigation, a finite element method (FEM) simulation validation of a printing pad was shown (Al Aboud, et al., 2018). This research concentrates on the sensitivity analysis of the FEM simulation results using the example of a given printing pad made of silicone rubber with 6 Shore A hardness. This 6 Shore A hardness is a medium hardness for printing pads. In order to obtain test specimens with the same specifications (Shore A hardness, material and mixing ratio) as the printing pads, the company Tampo-Technik GmbH was commissioned to manufacture the test specimens and the printing pads.

As shown in (Al Aboud, et al., 2018), the FEM can be a method to study printing pad shapes and loads. The FEM is a numerical method for solving technical problems by calculating the mechanical equation of a real technical operation on the computer. Typical problems solved by FEM are structural analysis, heat transfer, fluid flow, and acoustics (Shih, 2014). Abaqus (Dassault Systèmes Simulia, 2011) is a very comprehensive FEM program, which has already been used in many studies and simulations (Jungh, et al., 2017). It is a very powerful, but also complex software that requires experienced engineers for modeling. Because of the high licensing costs, it is usually used in large companies or specialized engineering offices. Our approach is to first use Abaqus to investigate the influence of material equations (material model), mesh types, and sizes on the reaction forces. For this investigation, a printing pad with a simple rectangular shape on a flat surface was used, which makes validation very easy (Velten, 2009). For validation, we compared the measured reaction forces on this planar surface of the printing pad from the experiment with the simulated reaction forces from the Abaqus simulation. In a second step, we then used the open source simulation software Salome-Meca and compared the simulation results with the results from Abaqus.

The parameters of the material to be investigated are required for the FEM simulation. For many standard materials these parameters are already available in the FEM software. However, the material properties of silicone rubber printing pads, a hyperelastic material, are unknown. Abaqus can calculate the material constants for the complex behavior of silicone rubber based on the three standardized material characterization methods. These methods are described in the section 2.

2. Determination of mechanical properties

As stated above, printing pads are made of silicone rubber, which is mixed with silicone oil to get a suitable Shore A hardness; that mixture is a kind of an elastomer (Rinnbauer, Stein and Pererseim, 2008). This type of mixing gives the printing pad different mechanical properties, including hardness. Besides the known value of Shore A hardness of the material, it is necessary to determine also the other mechanical properties of silicone rubber to solve the equations of the material deformation. The mechanical properties of this printing pad material should be determined by the Poisson test, volumetric compression test and mechanical tests. Therefore, we have characterized various silicone rubber samples in a Zwick Z050 test machine to obtain the following results.

Poisson's ratio is defined by the ratio of strain in "passive" direction (normal to load) to the "active" strain in length direction (ASTM International, 2014). The Poisson's ratio is calculated according to Equation [1]. The strain in transverse and axial directions is measured with a video extensometer system during the uniaxial tensile test execution at the same time. The value of 0.49 was calculated for silicone rubber test specimens with hardness of 6 Shore A.

$$\text{Poisson's ratio} = \left|\frac{\text{Strain in transverse}}{\text{Strain in axial}}\right| \qquad [1]$$

The uniaxial tensile, compression and planar tensile tests should be executed to get the stress–strain diagram of the silicone rubber material, which is produced under the same boundary conditions as the printing pad with hardness of 6 Shore A. Here, the Zwick Z050 test machine with ± 2 µm position repetition and 27 nm travel resolution accuracy was used to execute the tests. The uniaxial tensile test was performed according to ASTM D412-98a (ASTM International, 1998) and ISO 37 (International Organization for Standardization, 2005) standards. In this case, the dumb-bell shape test specimen type 1 was selected and the test length of 25 ± 0.25 mm on test specimens was marked. A video extensometer system measured the marked area length changes to calculate the strain values in the test process. Force values were measured during the test execution to calculate the stress. Every specimen was loaded and unloaded three times, and the average load curve was used for the FEM simulation to account for slight deviations between them. Figure 2 shows the specimen.

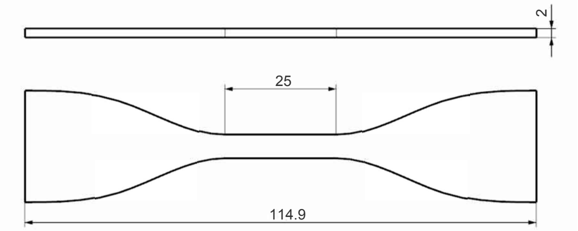

Figure 2: Uniaxial tensile test specimen in accordance to ISO 37 (International Organization for Standardization, 2005), 6 Shore A; size is in mm

The planar tensile test was applied in the same standard till the maximum strain of 55 % with a rectangular test specimen. In this case, the test specimen is a silicone rubber sheet with the test length of 8 mm and width of 60 mm.

The compression test method is defined in ISO 7743 standard (International Organization for Standardization, 2011). The test type B was performed according to this standard on a cylindrical test specimen with diameter of 17.8 ± 0.15 mm and height of 25 ± 0.25 mm.

The experimental results of tensile, planar and compression tests for silicon rubber of 6 Shore A are presented in Figures 3 to 5. The strain and stress loading–unloading behavior of silicone rubber with 6 Shore A hardness are clarified here.

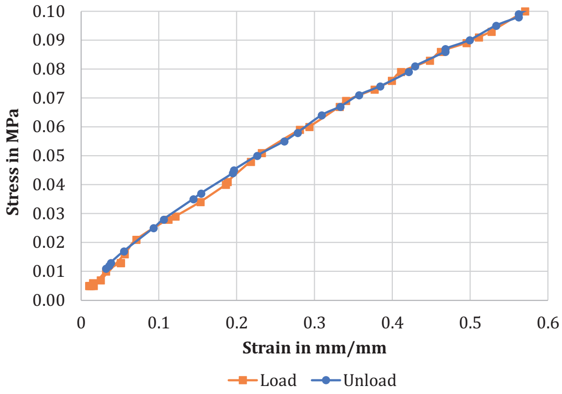

Figure 3: Tensile stress–strain curve (loading–unloading) for 6 Shore A silicone rubber

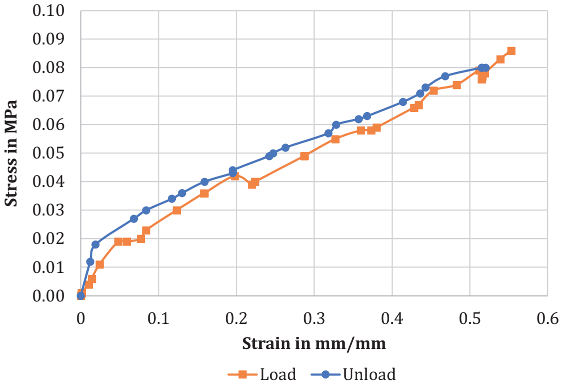

Figure 4: Planar stress–strain curve (loading–unloading) for 6 Shore A silicone rubber

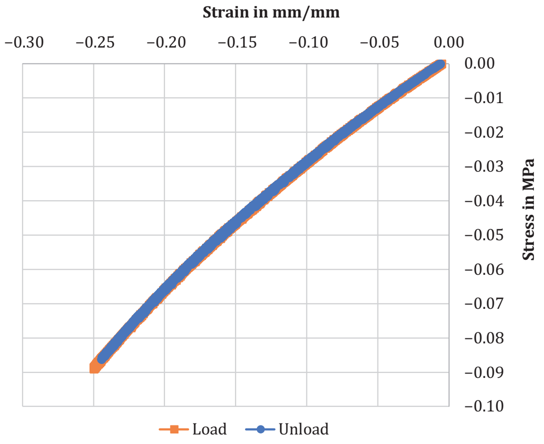

Figure 5: Compression stress–strain curve (loading–unloading) for 6 Shore A silicone rubber

These data were entered into the FEM software Abaqus as parameters for the printing pad material. Thus, all requirements for a simulation are met, only if the mathematical approximation for the behavior of the silicone material is known. It can be described by

Korochkina, et al., (2008) in a strain energy potential W Equation [2].

$$W(\bar{I}_1,\bar{I}_2,J) = \sum_{i+j=1}^{N} C_{ij}(\bar{I}_1-3)^i\,(\bar{I}_2-3)^j+\sum_{i=1}^{N}\frac{1}{D_i}(J-1)^{2i} \qquad [2]$$

Where C_{ij} and D_i are material parameters, and J is the elastic volume ratio. These parameters can be obtained by curve fitting to stress–strain data from the mechanical tests (Korochkina, et al., 2008).

For a good engineering approximation, rubber can be considered as incompressible. If the silicone rubber can nevertheless be compressed, a (further) volumetric compression test must be carried out. Equation [2] has only two independent strain invariants, which are $\bar{I}_1$ and $\bar{I}_2$. They are the first and second invariants of the deviatoric left Cauchy-Green deformation tensor (Korochkina, et al., 2008).

If all parameters of Equation [2] are now known via the material tests, then it can be solved by the FEM software. There are several methods for this. Mooney–Rivlin or polynomial equations are mathematical models to define the strain energy equation during deformation of the silicone rubber. They are often used for silicone rubber materials or other hyperelastic materials (Korochkina, et al., 2008). The polynomial equation is selected for all following simulations.

The relation between stress and strain for an incompressible hyperelastic material under tension/compression is elucidated in Equation [3] (Rivlin, 1956)

$$\sigma_e = 2\cdot(\lambda-\lambda^{-2})\cdot\left(\frac{\partial W}{\partial I_1}+\frac{1}{\lambda}\frac{\partial W}{\partial I_2}\right) \qquad [3]$$

where σ_e is tension or compression stress, and λ is strain, parallel to σ_e.

Equation 4 shows the relation between stress and strain for an incompressible hyperelastic material under simple shear (Rivlin, 1956).

$$\tau = 2\cdot\gamma\cdot\left(\frac{\partial W}{\partial I_1}+\frac{\partial W}{\partial I_2}\right) \qquad [4]$$

Where τ ist shear stress, and γ is shear strain.

From stress–strain values of the planar, biaxial test, Poisson test, volumetric compression test and tensile tests the software Abaqus is able to calculate the Mooney–Rivlin or polynomial constants. The calculations are based on a curve fitting method between the measured stress values from experimental tests and the calculated stress from the models for hyperelastic material (Equations [3] and [4]). These constants can also be used later in the open source FEM software Salome-Meca.

3. FEM simulations

We used Abaqus to create an accurate FEM simulation. To approximate the printing pad geometry a three-dimensional mesh is generated by the FEM software. The mesh element type and size play important roles in simulation results (Tadepalli, Erdemir and Cavanagh, 2011). In general, three-dimensional meshes

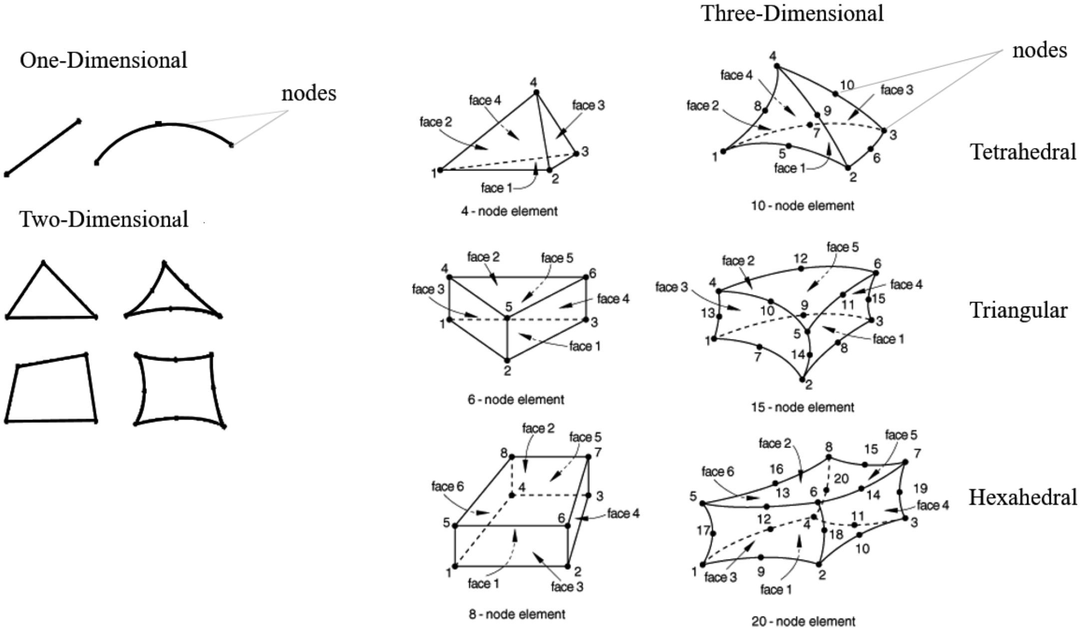

Figure 6: Mesh element types in Abaqus with their nodes, adapted from Dassault Systèmes Simulia (2008)

for finite element analysis must consist of tetrahedra, pyramids, prisms or hexahedra. Figure 6 illustrates the mesh types with their nodes. Only three-dimensional mesh types can be used to approximate the pad geometry.

In accordance with the Abaqus manual (Dassault Systèmes Simulia, 2011), the following can be said about the problem at hand: for the given printing pad geometry, only three of the three-dimensional mesh types are possible. These are Tetrahedra (C3D10) with 10 nodes or 4 nodes, Triangular (C3D15) with 15 nodes or 6 nodes and Hexahedra (C3D20) with 20 nodes or 8 nodes. A three-dimensional mesh type is proposed for the mechanical response of two-dimensional heterogeneous materials (Zhang and Katsube, 1995). They are in this simulation silicone rubber (printing pad) against steel (substrate table). Hybrid mesh elements C3D10H are primarily intended for simulating incompressible materials, e.g. hyperelastic behavior modeling with rubber (Dassault Systèmes Simulia, 2011). For the geometry of the silicone rubber printing pads, the mesh element type C3D10MH and C3D10H are used in this simulation, where (M) means the modified mesh element type of C3D10 (Dassault Systèmes Simulia, 2011). In literature (Tadepalli, Erdemir and Cavanagh, 2011) the mesh element type C3D10MH has been used for the simulation of incompressible neo-Hookean material and it has given very good results (Guo, et al., 2016). Reduced integration and modified mesh element types are used in this simulation. This causes buckling of the mesh element with one node. This problem is called hourglassing. In these places of the geometry the mesh density must be increased (Brown, 1997). Table 2 shows the element types used with their properties.

Table 2: Mesh element types used

Mesh element type	Description
C3D10MH	10 nodes, modified mesh element tetrahedron, with hourglass control, hybrid
C3D10H	10 nodes tetrahedron, with hourglass control, hybrid
C3D20H	20 nodes hexahedral, hybrid

The mesh element size is the maximum length of the mesh element in mm. This parameter determines the density of the mesh of the geometry. The mesh element size in this simulation is chosen between 2 mm and 8 mm. Figure 7 shows an example of the mesh with a mesh element size of 5 mm of a printing pad with mesh element type C3D10MH and the flat steel surface with mesh element type C3D20H.

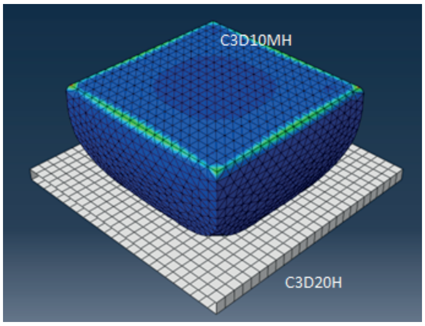

Figure 7: Mesh of a printing pad (74 mm × 72 mm × 52 mm) on a flat steel surface, the mesh element size is 5 mm; mesh element type C3D10MH is used for the printing pad (blue) and mesh element type C3D20H for the flat steel surface

4. Results of the simulation

The Abaqus FEM simulation gives good results close to measured values of displacement (pad deformation path) and the reaction force during printing. The displacement indicates how a small volume element on the printing pad surface shifts due to the deformation caused by the reaction force; the force sensor has a measuring range from 0.1961 N to 980.665 N. The FEM simulation results were validated by means of experimental investigations. An improved pad printing machine (Hakimi Tehrani, Dörsam and Neumann, 2016; Hakimi Tehrani, 2018) is used to monitor the printing pad displacement and reaction force during printing by the use of sensors and it stores the data for analysis. Afterwards, the measured parameters are compared with the simulation results; where in all the diagrams, displacement is the deformation path of the printing pad in the vertical direction on the printing pad base during printing.

Figure 8 illustrates the simulated and measured reaction forces during printing. At the zero point, the top of the pad just touches the flat steel surface. With increasing vertical movement, the reaction forces increase. They do not increase linearly. Figure 8 shows a little difference between the experimental data and the result of simulation of the different mesh elements sizes. This difference is acceptable because the simulation results usually are not exactly matching the experimental results (Tadepalli, Erdemir and Cavanagh, 2011). The simulation results of three different mesh sizes (2 mm, 4 mm, 8 mm) clarify the effect of the size on the simulation results. We can note that the simulation took a very long time for 2 mm elements (about 12 hours) while other sizes 4 mm and 8 mm had nearby the same result with far less time of about 20 minutes. So, we can say that the mesh sizes in this range do not play a significant role in improving the simulation result in this case.

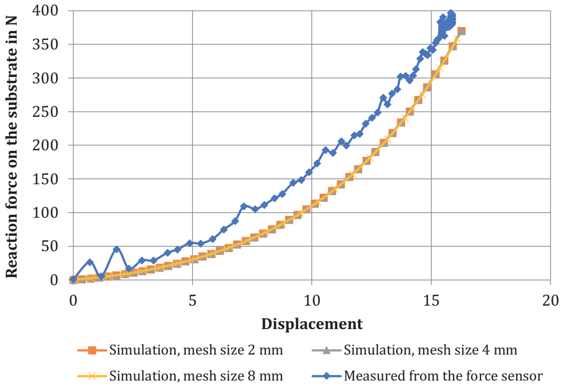

Figure 8: Comparison of the force–displacement diagram from experimental data and the simulation results obtained with Abaqus with three different mesh element sizes

Figure 9 shows the simulation results of different mesh element types with the mesh element size of 4 mm. The mesh element type of C3D10H is compared with C3D10MH. The mesh element type 3D10MH is a modified formulated meshing method (see Table 2). Both mesh element types are compared with the experimental results.

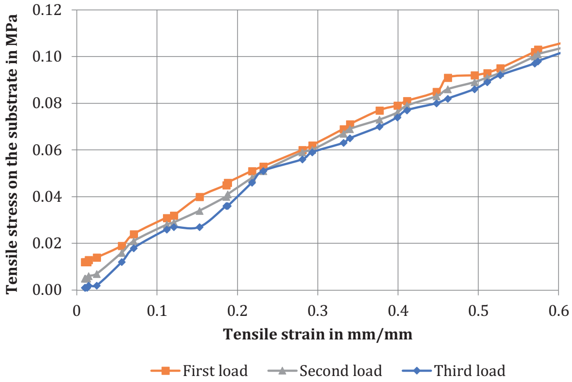

Figure 9: Comparison of the force–displacement diagram from the machine and the Abaqus simulation results with two different mesh element types C3D10H and C3D10MH

Figure 9 shows that the mesh element type C3D10MH does not lead to any improvements. The Abaqus simulation results of both mesh types are identical. It can be concluded that the mesh element type does not play an effective role in the accuracy of the simulation results in this application.

5. Sensitivity analysis of FEM simulation

As mentioned before, the force values from the simulation and the measurement do not match exactly. Small difference between the experimental data and the calculated data depends on the simulation parameters, especially, the material parameters. In the following, a sensitivity analysis is performed to determine the influence of the parameters.

Sensitivity analysis is a method for estimating the range of variation of the results by varying the simulation input variables. In this paper, the input variables are the mechanical properties of the printing pad material and the mathematical models of the hyperelastic material. The sensitivity analysis deals with the assumption: if the simulation results remain stable even with changed input variables, it can be determined how the target function value changes with the variation of input variables and which input variables have what influence on the resulting target function values (reaction force on the substrate during printing) (Schwenk, 2007).

The sensitivity analysis is performed by changing the simulation parameters of the FEM simulation, or by changing the material properties to improve the validation of the FEM simulation. Important input variables are the measured values of the test for characterization of the material by the uniaxial and planar tensile tests and the compression test (see section 2). These tests are performed several times for statistical purposes. In the following we will consider the sensitivity of the simulation in Abaqus from three individually performed tests. Finally, we will investigate the influence of the chosen mathematical model on the accuracy of the Abaqus simulation.

5.1 Effect of the error in the uniaxial and the planar tensile test

The uniaxial and the planar tensile test are considered in this study for the investigation of the error influence by the determination of the material characteristic values.

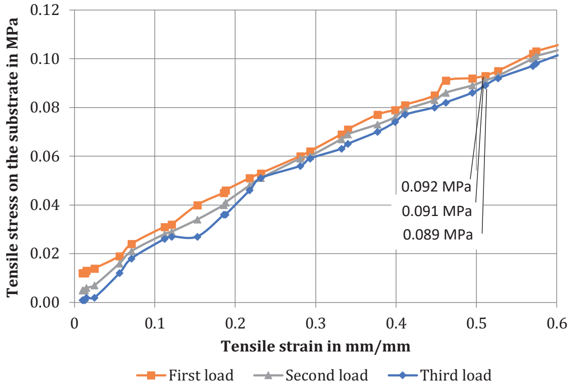

Figure 10: The uniaxial tensile test for one specimen made from 6 Shore A silicone rubber stressed in three cycles, only the load is taken from each cycle

The tensile test was carried out three times on the same tensile specimen with 6 Shore A hardness, and produced three fluctuating datasets. Figure 10 shows the stress–strain diagram for the first, second and third load applied on the tensile specimen.

The datasets are used as input parameters for three Abaqus FEM simulations and thus give three different results for the reaction force. These are shown in Figure 11. A slight divergence can be noticed between the three curves. Figure 11 shows the increased reaction force by increasing the deformation of the printing pad from the simulations.

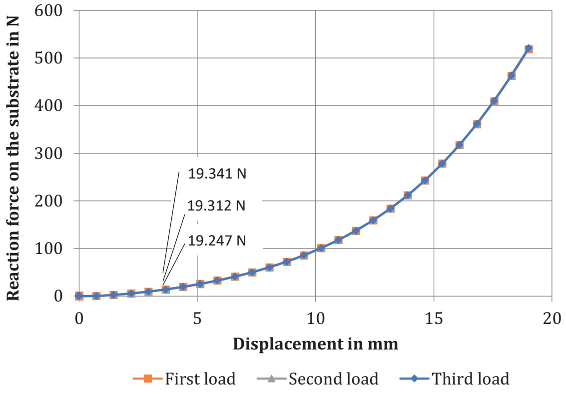

Figure 11: Abaqus simulation results based on the three tensile tests shown in Figure 10, reaction force over the deformation path (displacement) on the printing pad; the mesh element type is C3D10H and the mesh size is 2 mm; the first, second and third simulation is based on the first, second and third tensile stress measurement, respectively

To sum this up, an increase in tensile stress from 0.089 MPa to 0.092 MPa at a strain of 0.5 mm/mm leads to a difference in reaction forces of about 0.1 N at a deformation of 4.3 mm. So, the influence of the tensile test result is very small (see Figures 10 and 11).

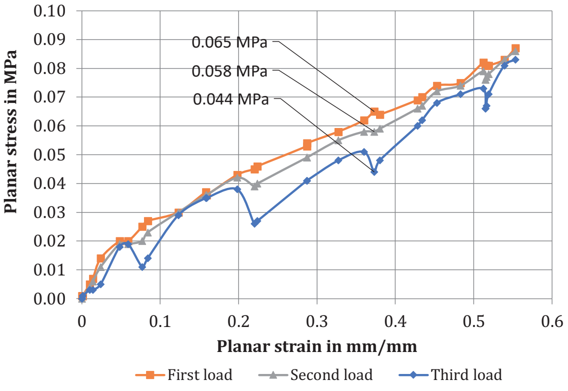

Figure 12: The planar tensile test for one specimen made from 6 Shore A silicone rubber stressed in three cycles, only the load is taken from each cycle

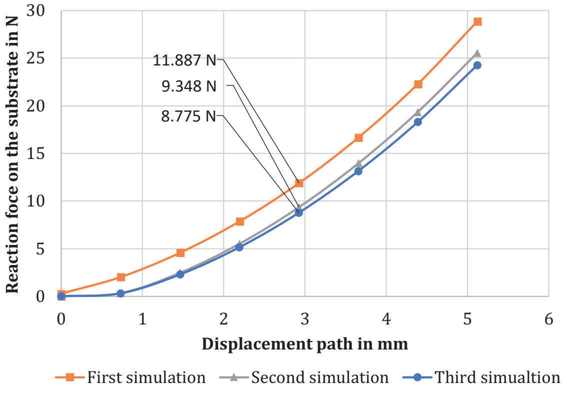

Figure 13: Abaqus simulation results for the three planar tensile tests, reaction force over the deformation path on the printing pad, the mesh element type is C3D10H and the mesh size is 2 mm; the first, second and third simulation is based on the first, second and third planar stress measurement

Let us now look in a similar way at the planar tensile test. The planar specimen is loaded three times. As Figure 12 shows, the fluctuations of the measured values between the individual loads are much bigger than in Figure 10. Somewhat unexpectedly Figure 13 shows that the deviations between the individual loads do not seem as large as the variations in Figure 12 might suggest.

To sum this up, an increase in tensile planar stress from 0.044 MPa to 0.065 MPa at a strain of 0.37 mm/mm leads to a difference in reaction forces of about 3.1 N at a deformation of 2.9 mm. So, the influence of the planar tensile test result is not small. The deviation of the reaction force at a deformation of 2.9 mm is 35.6 % (see Figures 12 and 13).

Nevertheless, the deviations of the different loads in Figure 13 are of great importance for the simulation. The errors in the planar tensile test change the calculated Mooney–Rivlin constants or the calculated polynomial constants, and these change the properties of matter in the simulation. As explained in section 2, these equations define the hyperelastic material for the FEM software. Let us first look at the behavior in compressibility for further understanding.

5.2 Effect of the volumetric compression test

Silicone rubber is normally considered to be incompressible. This is equivalent to a Poisson's ratio of 0.5. Since the determination of the Poisson's ratio is complex, the volumetric compression tests have been used, to provide a dataset of silicone rubber material compressibility.

This test differs from the normal compression test in that the strain on the specimen in this test is a volumetric strain and not a longitudinal strain. We get from volumetric compression test the bulk modulus B.

In volumetric compression test, a cylindrical specimen is pressed into a closed cylinder while the values of the volume change and the associated compression stress is measured. Figure 14 shows the changes in volume ΔV in relation to the total volume due to pressure. The slope of the compression curve is a measure of compressibility and can be described with the bulk modulus. The bulk modulus B is calculated with the Equation [5] (Brotzman and Eichinger, 1982):

$$B = \frac{\Delta P}{\Delta V/V} \qquad [5]$$

Where ΔP is the pressure difference between two points on the curve in Figure 14. The calculated bulk modulus is 500 MPa and the material is, therefore, incompressible.

In Salome-Meca the bulk modulus is calculated from the Poisson's ratio and the constants in the Mooney–Rivlin equation using Equation [6]:

$$B = 2 \cdot (\mathrm{C01} + \mathrm{C10})/(1 - 2 \cdot \nu) \qquad [6]$$

where C01 and C10 are Mooney–Rivlin constants and ν is the Poisson ratio (Gehrmann, et al., 2017).

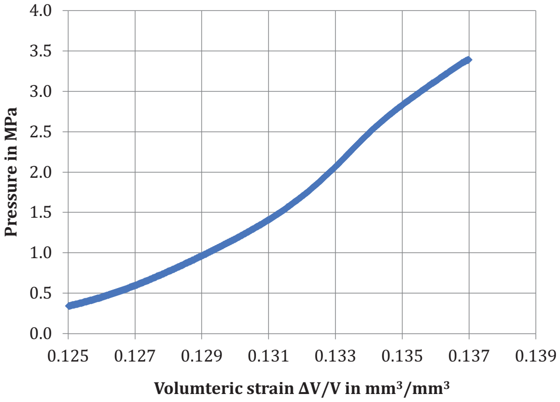

Figure 14: The measured results of the volumetric compression test; the volumetric change ΔV as a result of the pressure in relation to the total volume V is plotted

Moreover, the influence of the volumetric compression test on the simulation results is relatively small, as shown in Figure 15. In the next step, the datasets of the volumetric compression tests are compared with the theoretical data using a Poisson's ratio of 0.5. The Abaqus simulation results are shown in Figure 15. There is no difference between the simulation results based on the data from the volumetric compression test and the theoretical values with a Poisson's ratio of 0.5. For our study the low compressibility of the printing pad material can therefore be ignored in the simulation. However, it can also be observed that the simulated deformations deviate from the measured values and are always larger at the same force.

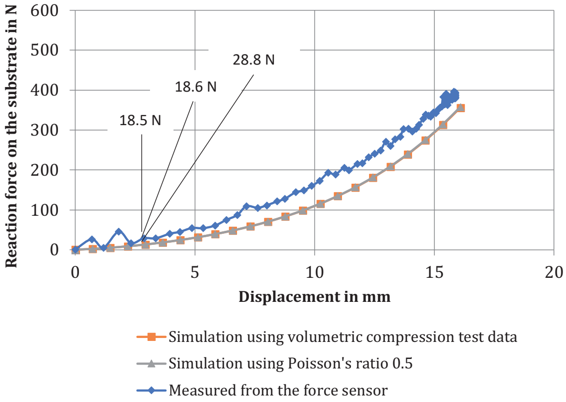

Figure 15: Comparison of resultant reaction forces versus displacement using the compression test and Abaqus simulation (mesh element type is C3D10H and the mesh size is 2 mm) for a Poisson's ratio of 0.5 and for using the data from the compression test; a measurement is shown for comparison

To sum this up, the use of measurement results from the volumetric compression test in the simulation leads to a small increase of the reaction force at a deformation of 2.9 mm by 0.1 N. The simulation results of both simulations are almost identical. However, the simulated deformations deviate from the measured values and are always greater with the same force (see Figure 15).

5.3 Effect of the biaxial test

From the data of the compression test and the other previous tests (see Figure 5), Abaqus can calculate the Mooney–Rivlin or polynomial constants for the material. Therefore, the compression test is usually performed. The uniaxial compression stress and biaxial stress are considered in small deformations equal (Hakimi Tehrani, 2018). The uniaxial compression test setup is simple and it can be performed quickly (see section 2). With hyperelastic materials, however, the calculation of the constants becomes often much more accurate when another test is done, the so called biaxial tensile test. This test is much more complex than the compression test. However, it has the advantage that the achievable strains are less limited.

The biaxial tensile test is similar to the uniaxial tensile test. However, the specimen is drawn simultaneously in two spatial directions. A cross-shaped flat specimen is loaded on four sides. This test requires a special test bench with complex measuring technology (Seibert, Scheffer and Diebels, 2014). Therefore, it should always be considered whether the biaxial tensile test is really needed.

Without conducting the biaxial tensile test, we would like to make some considerations for the usefulness of the test. For this we used the results of the compression test from Figure 5 (see section 2). Here we see that the simulation results (reaction force on the substrate with displacement) differ from the measured values from the force sensor (see Figure 16). We therefore want to look into the question of which influence the measured data have on the determination of the Mooney–Rivlin or polynomial constants. If the measured compression stress values are multiplied by a constant factor, the specimen shows a stiffer behavior. For further consideration the compression stress values of Figure 5 were multiplied by 1.5 and entered as input parameters in the Abaqus simulation. The results are given in Figure 16. The graph for the compression test from Figure 5 and the measured values of the reaction force from Figure 16 are shown. Furthermore, the Abaqus simulation results are plotted with the multiplied values (modified compression test values). To our surprise these simulated values correspond very well with the measured values from Figure 5 up to a deformation of 10 mm. This means that with a stiffer material the behavior of the printing pads can be described much better. A better description of the material can be achieved by determining the constants more precisely. This is made possible by a biaxial tensile test. For further investigations, the biaxial tensile test should therefore be carried out for the simulation of silicone rubber printing pads. For deformations up to 10 mm we could also use the results from the modified compression test (see Figure 16) as a first approximation.

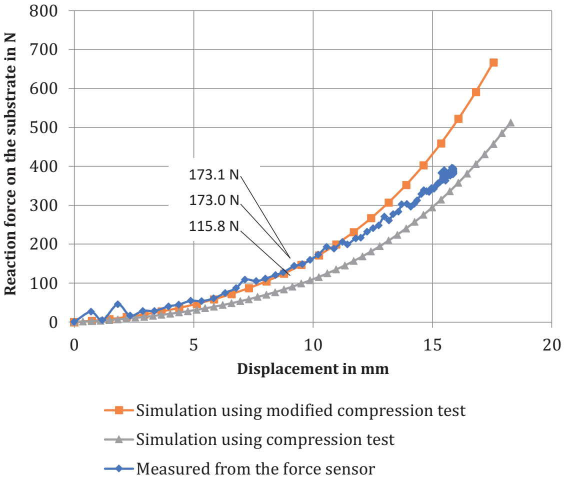

Figure 16: Abaqus simulation (mesh element type is C3D10H and the mesh size is 2 mm) using data from the compression test and from a modified compression test compared to experimental data

To sum this up, the deviation of the reaction force at a deformation of 9 mm is 0.05 % for the simulation with modified compression test and 33 % for the simulation with compression test (see Figure 16).

To get more effective results, we developed the biaxial clamps to fit the available Zwick Z050 test machine and silicone rubber material, and use this results in the simulation. The experimental result of biaxial tensile test for silicon rubber of 6 Shore A is presented in Figure 17.

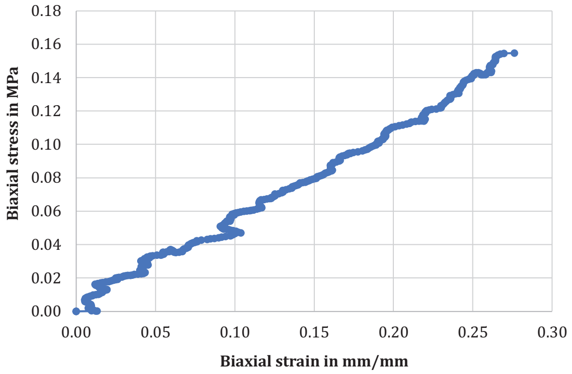

Figure 17: Measured results of the biaxial tensile test for 6 Shore A silicone rubber

By comparing the absolute results in Figure 17 with Figure 5 at strain 0.25, we get 1.5 times more stress at the same point in Figure 5.

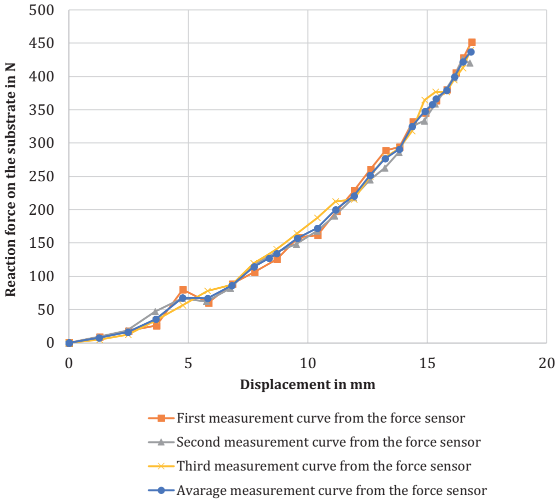

Figure 18: Measured results of the force sensor

After that, we performed three measurements on the force sensor to confirm previous measurements result and took the average curve, in consideration that all measurements begin at the touching point between the printing pad surface and the substrate, which is 145 mm on the servo motor (0 mm displacement), and keep servo motor going on until 162 mm (17 mm displacement), see Figure 18.

Finally, we compare simulation using biaxial test and simulation using compression test with average measurement curve from the force sensor, to find that our simulation using biaxial test is more reliable and effective (see Figure 19).

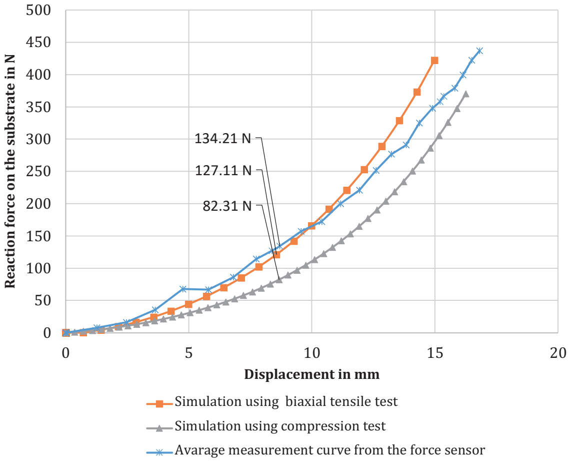

Figure 19: Abaqus simulation (mesh element type is C3D10H and the mesh size is 2 mm) using data from the compression test and from biaxial tensile test compared to average measurement curve from the force sensor

In summary, it can be said that the deviation of the reaction force at a deformation of 8.5 mm is 5 % in the simulation with biaxial tensile test and 34 % in the simulation with compression test (see Figure 19). The use of the biaxial tensile test therefore leads to a better simulation result of printing pads.

5.4 Effect of the mathematical model

The behavior of the deformed material is described by material models (equations); these models are the basis for every FEM simulation. As already explained in section 2, the polynomial equation is selected for all previous simulations. There are many mathematical models to describe the material behavior of silicone rubber. In the following, three simulations with three different mathematical models are carried out. These models are Mooney–Rivlin, polynomial and neo-Hooke (see section 2).

Figure 20 shows the reaction force over the deformation path for the three simulations and the experimental data resultant from the force sensor. As shown in Figure 20, the neo-Hooke simulation does not fit the experimental data at all. This shows how important the correct selection of equations is. As Figure 20 also shows, the simulation results of the Mooney–Rivlin and polynomial equations for small deformations are approximately equivalent. For further investigations, the simulation quality can be further improved by better material tests, i.e. in particular by an additional biaxial tensile test.

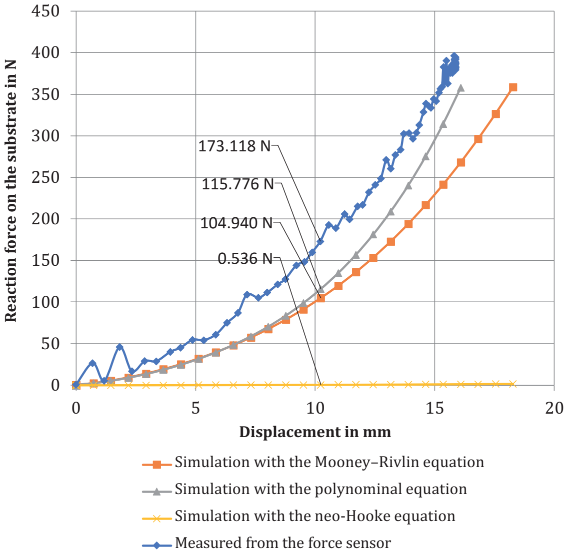

Figure 20: Abaqus simulation (mesh element type is C3D10H and the mesh size is 2 mm) using Mooney–Rivlin equation, polynomial equation and neo-Hooke equation compared to experimental data

The concavity of the resulting curve from polynomial model is very similar to the measured curve from force sensor. When the pad is stiffer, as shown in Figure 16, the two curves are the same.

6. Workflow for improving the printing pad geometry

For small deformations, as they will occur for printing pads, a development tool for the investigation and design of silicone rubber printing pads has been found. In principle it is now possible to investigate and optimize the geometry of a printing pad using FEM simulation. The necessary workflow is shown in Figure 21. For the realization of an FEM based geometry optimization of printing pads already certain basic knowledge in the use of FEM software is recommended.

The first step is to load the geometry of the substrate to be printed in the FEM software and create an FEM model. The FEM model also includes the material data of the silicone rubber, which must be determined beforehand with the described material tests (see section 2). Furthermore, it is recommended to use either the polynomial or Mooney–Rivlin equations. In the second step, the user has to select a pad geometry, which should be optimized, and start the FEM simulation. Based on the calculated results, the user can then decide whether the results meet the requirements or whether a different or modified printing pad geometry should be simulated. The most important requirement for a good pad geometry is the zero displacement on the printing surface of the printing pad. The second requirement is to keep the internal pressure low, because very high pressures lead to permanent deformation of the pad material after a period of time. After going through several iterations, the printing pad geometry can be determined with the desired requirements.

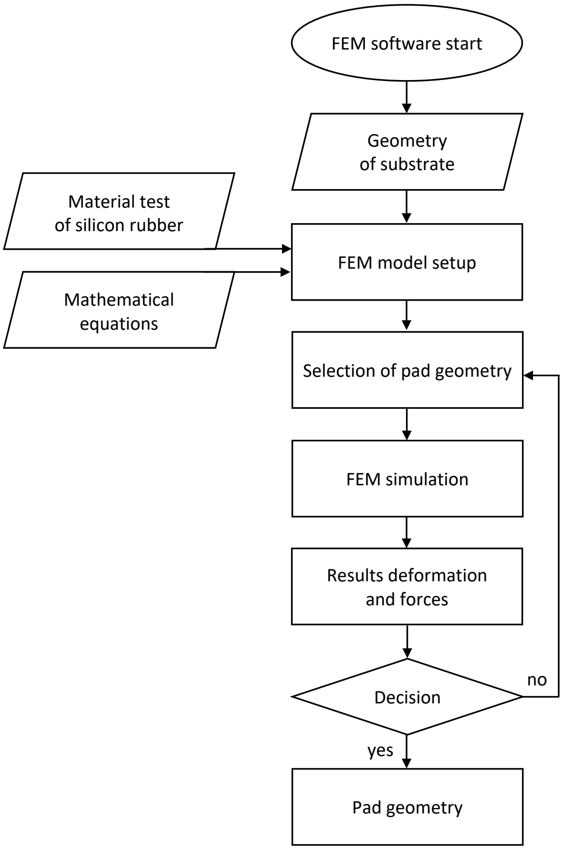

Figure 21: Workflow for investigation of printing pad geometry by using FEM simulation

It should be noted that the geometry of the printing pad cannot yet be calculated automatically with this workflow. The pad printing process is too complex for this. In the future, however, further investigations will lead to the step-by-step development of further tools.

7. Comparison of Abaqus and Salome-Meca software

As mentioned before, printing pad manufacturers are often rather small companies and therefore cannot afford the high license fees of Abaqus. Therefore, a first study will be conducted to check whether the open source FEM software Salome-Meca is also suitable for a simulation of printing pads. The FEM software Salome-Meca can also simulate hyperelastic materials using polynomial and Mooney–Rivlin equations. Similar to Figure 20, the reaction force on the substrate was therefore simulated as a function of the displacement (deformation path of the pad) and compared with the measured values.

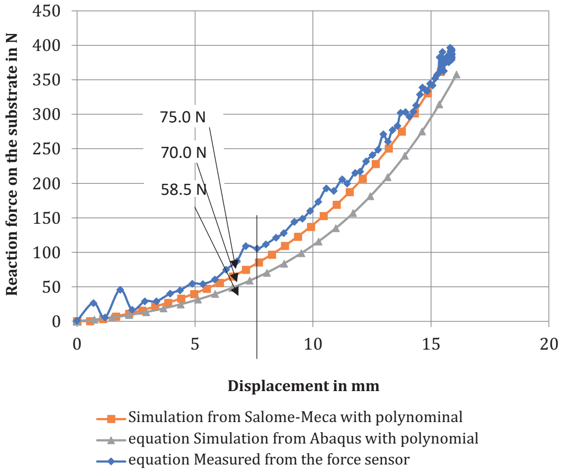

Figure 22: Abaqus and Salome-Meca simulations with polynomial equations compared to measured data

Figure 22 shows the measured reaction forces and the simulation by Abaqus and Salome-Meca. In both simulations the polynomial equation was used. The constants of the polynomial equation were calculated from the material tests with Abaqus software to use these constants in Salome-Meca software. The open source software Salome-Meca achieves good results. The graph is much closer to the measured values than the results of Abaqus. This is especially important for the expected small deformations of printing pads. The difference in Salome-Meca from Abaqus is that Salome-Meca calculates the bulk modulus from the constants of Mooney–Rivlin equation and Poisson's ratio.

From the Abaqus and Salome-Meca simulations we can plot the displacement field in x direction and z direction of the surface of the printing pad.

Figure 23 shows that the results from both software are very similar and in the center of the printing pad the displacement is at its lowest. It is recommended to place the print image as close as possible to the center of the printing pad. With this type of graphics, a user can see whether the allowed deformation in a particular, interesting area of a layout is met or exceeded.

If the displacement during the printing process is known from the simulation, we can learn more about the deformation of the print image in any direction.

The precision of printing sharp edges in pad printing is a problem due to the expandability of the pad surface. This makes it difficult for printing of microelectronics (Bodenstein, et al., 2019). The shape of the printing pad can be developed in such a way that we achieve the smallest possible deformation of the surface of the printing pad.

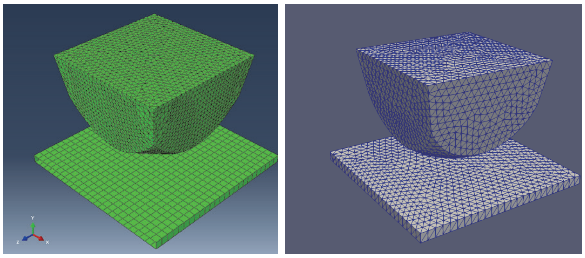

Mesh–model from Abaqus *Mesh–model from Salome-Meca*

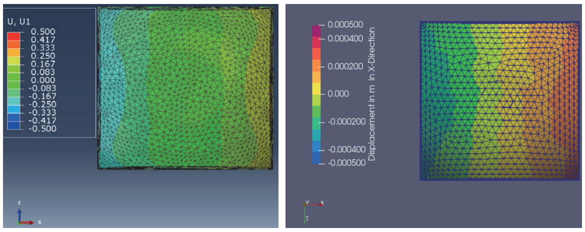

Displacement field in x-direction in mm from Abaqus *Displacement field in x-direction in m from Salome-Meca*

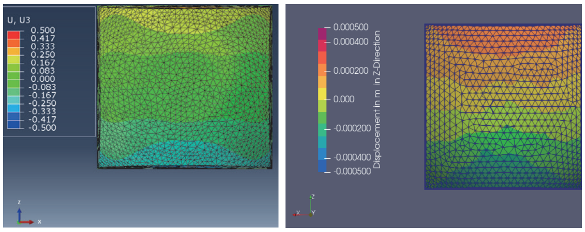

Displacement field in z-direction in mm from Abaqus *Displacement field in z-direction in m from Salome-Meca*

Figure 23: Comparison between simulation results from Abaqus and Salome-Meca of the same printing pad (74 mm × 72 mm × 52 mm) on a flat steel surface at a displacement of 3 mm, the mesh element size is 4 mm, and Mesh element type C3D10MH (please note that the results from Abaqus are plotted in mm and that of Salome-Meca in m)

The differences between the FEM software Abaqus and Salome-Meca have been clarified. However, it is pleasing to note that the free open source software Salome-Meca is basically suitable for the optimization of silicone rubber printing pads.

8. Conclusion and outlook

Even in the age of digitalization, the manufacturing of printing pads is still a manual process. So far, no modern tools are known to support this manufacturing process. In this paper we focus on how FEM software can be used to optimize the geometry of a silicone rubber printing pad. Silicone rubber is a polymeric, elastic material, whose data are not available in the usual FEM programs. Therefore, uniaxial tensile, planar tensile and compression tests have to be performed. After all, suitable equations have to be found for the FEM model setup.

In this study, investigations were performed with the FEM software Abaqus and the Mooney–Rivlin and polynomial constants were determined. The simulation results for a given printing pad were compared with measured deformations and forces. A comparison shows deviations, especially for larger deformations. A sensitivity analysis shows that an additional biaxial tensile test is a possibility to determine the material properties more accurately. The results also show that a simulation is well possible for small deformations. A workflow is shown how a geometry of a printing pad can be simulated and optimized. Finally, it is shown that the open source FEM software Salome-Meca can be used to simulate and optimize silicone rubber printing pads.

This study is an introduction to modern development tools for the design of printing pads. Basically, the FEM method is suitable to support the design and optimization of printing pads. Nevertheless, some open questions remain, which should be clarified in further investigations. For example, the biaxial tensile test should be validated in addition to the characterization of the materials. Thus, the Mooney–Rivlin and polynomial constants can be determined more precisely and the deviations from experimental data can be reduced. The surprising differences between the Abacus and Salome-Meca simulations should also be investigated.

Acknowledgements

D. S. likes to thank Merck KGaA for financial support through the Merck Lab @ TU Darmstadt.

References

Al Aboud, A., Dörsam, E., Hakimi Tehrani, A. and Spiehl, D., 2018. Using FEM simulation as a tool to develop pad printing. In: P. Gane, ed. *Advances in Printing and Media Technology: Proceedings of the 45th International Research Conference of iarigai*. Warsaw, Poland, October 2018. Darmstadt, Germany: iarigai.

Antman, S.S. ed., 2004. *The non-linear field theories of mechanics*. 3rd ed. Berlin, Heidelberg, Germany: Springer.

ASTM International, 1998. *ASTM D412-98a Standard test methods for vulcanized rubber and thermoplastic rubbers and thermoplastic elastomers-tension.* West Conshohocken, PA, USA: ASTM International.

ASTM International, 2014. *ASTM D638-14 Standard test method for tensile properties of plastics.* West Conshohocken, PA, USA: ASTM International.

Brown, J., 1997. Characterization of MSC/NASTRAN & MSC/ABAQUS elements for turbine engine blade frequency analysis. In: *MSC Aerospace Users' Conference Proceedings*. Newport Beach, CA, USA, 17–20 November 1997.

Brotzman, R.W. and Eichinger, B.E., 1982. Volume dependence of the elastic equation of state. 3. Bulk-cured poly (dimethylsiloxane)*. Macromolecules*, 15(2), pp. 531–535. https://doi.org/10.1021/ma00230a061.

Bodenstein, C., Sauer, H.M., Fernandes, F. and Dörsam, E., 2019. Assessing and improving edge roughness in pad-printing by using outlines in a one-step exposure process for the printing form. *Journal of Print and Media Technology Research*, 8(1), pp. 19–27. https://doi.org/10.14622/JPMTR-1903.

Gehrmann, O., Kröger, N.H., Erren, P. and Juhre, D., 2017. Estimation of the compression modulus of a technical rubber via cyclic volumetric compression tests. *Technische Mechanik*. 37(1), pp. 28–36. https://doi.org/10.24352/UB.OVGU-2017-048.

Guo, Z., Chen, Y., Peng, X., Shi, X., Li, H. and Chen, Y., 2016. Shear stiffness of neo-Hookean materials with spherical voids*. Composite Structures*, 150, pp. 21–27. https://doi.org/10.1016/j.compstruct.2016.04.046.

Hakimi Tehrani, A., Dörsam, E. and Neumann, J., 2016. Improving automation and process control of an indirect gravure (pad) printing machine. *Acta Polytechnica Hungarica*, 13(4), pp. 221–240. https://doi.org/10.12700/APH.13.4.2016.4.14.

Hakimi Tehrani, A., 2018. *Automation improvement of indirect gravure printing with a focus on the mechanical characteristics of silicone rubber pads.* Dr.-Ing. Dissertation. Technische Universität Darmstadt.

Hahne, P., 2001. *Innovative Drucktechnologien: Siebdruck-Tampondruck..* Lübeck, Germany: Verlag Der Siebdruck.

International Organization for Standardization, 2005. *ISO 37:2005 Rubber, vulcanized or thermoplastic – Determination of tensile stress–strain properties*. Geneva, Switzerland: ISO.

International Organization for Standardization, 2011. *ISO 7743:2011 Rubber, vulcanized or thermoplastic – Determination of compression stress–strain properties.* Geneva, Switzerland: ISO.

Jungh, T., Glasenapp, T., Fraas, M., Schulz, A. and Bauer, H.-J, 2017. Durchführung von FEM Simulationen zur Anwendung des Superpositionsprinzips der Filmkühlung. In: *Proceedins of Deutscher Luft- und Raumfahrtkongress 2017*. München, Germany, 5–7 September 2017. Bonn, Germany: Deutsche Gesellschaft für Luft- und Raumfahrt.

Kipphan, H. ed., 2001. *Handbook of print media*. Heidelberg, Germany: Springer.

Korochkina, T.V., Jewell, E.H., Claypole, T.C. and Gethin, D.T., 2008. Experimental and numerical investigation into nonlinear deformation of silicone rubber pads during ink transfer process*. Polymer Testing*, 27(6), pp. 778–791. https://doi.org/10.1016/j.polymertesting.2008.06.003.

Pudas, M., Hagberg, J. and Leppävuori, S., 2004. Printing parameters and ink components affecting ultra-fine-line gravure-offset printing for electronics applications. *Journal of the European Ceramic Society*, 24(10–11), pp. 2943–2950. https://doi.org/10.1016/j.jeurceramsoc.2003.11.011.

Rinnbauer, M., Stein, G., Peterseim, V., 2008. Elastomere. In. H. Domininghaus, P. Elsner, P. Eyerer and T. Hirth, eds. *Kunststoffe: Eigenschaften und Anwendungen*. Berlin, Germany: Springer.

Rivlin, R.S., 1956. Large elastic deformations. In F.R. Eirich, ed. *Rheology*. New York: Academic Press, pp. 351–385.

Schwenk, C., 2007. *FE-Simulation des Schweißverzugs laserstrahlgeschweißter dünner Bleche Sensitivitätsanalyse durch Variation der Werkstoffkennwerte.* Dr.-Ing. Dissertation. Technische Universität Berlin.

Seibert, H., Scheffer, T. and Diebels, S., 2014. Biaxial testing of elastomers: experimental setup, measurement and experimental optimisation of specimen's shape*. Technische Mechanik*, 34(2), pp. 72–89. https://doi.org/10.24352/UB.OVGU-2017-054.

Shih, R., 2014. *Introduction to finite element analysis using SolidWorks simulation.* Klamath Falls, OR, USA: SDC Publications.

Dassault Systèmes Simulia, 2008. *Abaqus analysis user's manual*. [online] Providence. RI, USA: Dassault Systèmes Simulia Corp. Available at: <http://130.149.89.49:2080/v6.8/books/usb/default.htm?startat=pt06ch23s01ael01.html> [Accessed December 2019].

Dassault Systèmes Simulia, 2011. *Abaqus 6.11 theory manual*. [pdf] Providence. RI, USA: Dassault Systèmes Simulia Corp. Available at: <http://130.149.89.49:2080/v6.11/pdf_books/THEORY.pdf> [Accessed December 2019].

Tadepalli, S.C., Erdemir, A. and Cavanagh, P.R., 2011. Comparison of hexahedral and tetrahedral elements in finite element analysis of the foot and footwear. *Journal of Biomechanics*, 44(12), pp. 2337–2343. https://doi.org/10.1016/j.jbiomech.2011.05.006.

Tampo Canada, 2018. *Pad printing vs. screen printing – the differences explained.* Tampo Canada Inc. [online] Available at: <https://www.tampocanada.com/pad-printing-vs-screen-printing> [Accessed December 2019].

Velten, K., 2009. *Mathematical modeling and simulation: introduction for scientists and engineers.* Weinheim, Germany: Wiley-VCH.

Zhang, J. and Katsube, N., 1995. A hybrid finite element method for heterogeneous materials with randomly dispersed rigid inclusions. *International Journal for Numerical Methods in Engineering*, 38(10), pp. 1635–1653. https://doi.org/10.1002/nme.1620381004.

JPMTR 134 | 2003
DOI 10.14622/JPMTR-2003
UDC 667.5:534.2

Research paper
Received: 2020-03-26
Accepted: 2020-06-24

Impact of printing surfaces with UV-curable inks on sound absorption

Vlado Kitanovski[1]*, Jonny Nersveen*[2]*, Anton Strand*[3] *and Marius Pedersen*[1]

[1] Department of Computer Science,
Norwegian University of Science and Technology, Building A,
Teknologiveien 22, 2815 Gjøvik, Norway
[2] Department of Manufacturing and Civil Engineering,
Norwegian University of Science and Technology, Building B,
Teknologiveien 22, 2815 Gjøvik, Norway
[3] Canon Norway AS, P.O. Box 33, Holmlia N-1201, Oslo, Norway

vlado.kitanovski@ntnu.no
jonny.nersveen@ntnu.no
anton.strand@canon.no
marius.pedersen@ntnu.no

Abstract

The recent UV-curable inks, used in modern inkjet printing systems, bring several advantages and therefore a potential to expand to new applications, including décor printing. In this work, we investigate the impact of printing with UV-curable inks on sound absorption. The sound absorption curves of three different sound-absorbing decorative wall plates are calculated from the reverberation times measured in a reverberation room. The comparison between the sound absorption from unprinted and printed decorative plates showed that printing with UV-curable inks has no significant impact on the sound absorbing characteristics of materials.

Keywords: sound-absorbing plate, reverberation time measurement, décor printing, UV-curable inkjet printing

1. Introduction

Inkjet printing and UV-curing technologies have developed in parallel since the 1950s (Cahill, 2001). Inkjet printing systems based on UV-curable inks enable print service providers to offer additional value to their customers and allow designers to create more stylish and impactful finishes on various types of surfaces (Canon, 2018). They have expanded the inkjet printing technology into alternative fields and applications like packaging, publishing, décor, textile design, and outdoor display (Parraman and Ortiz Segovia, 2018, p. 96). The base of the UV-curable inks is composed of fluid monomers that, when exposed to UV radiation, polymerize into a hardened dry ink containing the pigment (Parraman, 2012).

The UV-cured inks bring several advantages: they are more reliable and have better sustainability ratings, they support extended gamut printing, they are tolerant and applicable to a variety of printing surfaces (Taylor and Cahill, 2015), and they can be used to produce a surface texture (Parraman and Ortiz Segovia, 2018, p. 96).

In this work, the focus is on the décor application, e.g., printing on materials used for decorative indoor walls or ceilings. The large surface area of walls and ceilings impacts the acoustic characteristics of the indoor space (Harris, 1991, pp. 64–66). Therefore, decorative walls and ceilings may require having certain sound-absorbing characteristics. These characteristics are closely related to the reverberation time of the indoor space, which is the time needed for the sound pressure level (SPL) to decay 60 dB after the source of the sound has stopped (Beranek and Mellow, 2012, p. 470). Several studies have been made to investigate the acoustic impact of different decorative surface coatings of objects in indoor spaces. Martellotta and Castiglione (2011) investigated the use of paintings and tapestries as sound-absorbing materials, where they among others looked at the combined effect of painted canvases covering porous materials. They found that impermeable treatments, from using oil or acrylic color, mostly influenced high-frequency absorption. Ivanova, Vitchev, and Hristodorova (2018) investigated the influence of different surface coatings on sound absorption of wood. They showed that coating improved sound absorption properties of the wood. Chrisler (1941) did measurements for sound absorption of different materials and paint, including different number of coats. The results indicated differences between the materials, as some could be painted with just one or two coats of paint before a decrease in sound absorption was detected, while others could be painted multiple times before a decrease was found. Xu, et al. (2020) investigated polyurethane coating thickness in sound absorption for four different wood species, where the results of the sound absorption is dependent on the wood species and coating thickness. Sayako and Yamamoto (2018) in their patent proposed a surface treatment liquid for porous sound-absorbing materials. The main goal was to add decorative elements to sound-absorbing materials without impairing the sound absorption capabilities of the surface. The surface treatment was in terms of an aqueous ink. Most examples showed small differences in an air permeability evaluation compared to unprinted samples.

In summary, the previous related works show that the sound-absorbing characteristic of a material can be influenced by the surface of that material. It is interesting to see whether depositing hardened UV-cured inks on indoor décor surfaces has an impact on the sound absorption, and therefore, on the acoustic characteristics of the indoor space. In fact, the potential of using UV-curable inks for printing on a wide range of materials used for decorative walls or ceilings is connected to their acoustic impact. To the best of our efforts, we were unable to find a study regarding the acoustic impact of surfaces printed with hardened UV-cured inks. One of the reasons for that could be the interdisciplinarity of the issue. The main goal of this work is to investigate this impact, i.e., to answer the question whether printing with UV-cured inks influences the sound-absorbing property of a material.

2. Methodology

The evaluation of the acoustic impact from printed surfaces is based on comparing the sound absorption between unprinted and printed sound-absorbing materials. When sound propagates in a closed space, the level to which the sound builds up as well as the decay of the reverberant sound after the sound source is stopped depends on the sound-absorbing characteristics of the boundary surfaces and objects filling the closed space (International Organization for Standardization, 2003). A closed space that is specifically designed so that the average sound pressure level is essentially uniform, i.e., the sound field is diffuse, is referred to as reverberation room (Vér and Beranek, 2006, p. 85). Measurement of the sound absorption of a given material is performed by measuring the reverberation time when the material is mounted in a reverberation room (International Organization for Standardization, 2003). As mentioned before, the reverberation time itself is a measure of the time needed for the stationary and diffuse sound to fade out, or more accurately, for the SPL to fall 60 dB after the sound source has stopped (Beranek and Mellow, 2012, p. 470). In the following subsections, the materials and equipment used for the measurements as well as the method for calculating the sound absorption are described.

2.1 Materials and equipment

We used three different sound-absorbing materials for the evaluation, Ecophon Akusto™ wall Super G™, Ecophon Akusto™ wall Texona, and Ecophon Akusto™ wall Akutex™ FT. They are to be used as decorative wall plates, and they are all made of glass wool but with different front-facing surface finishing. In the rest of the text we refer to them as three different quality types, from one to three. Their dimensions are 2.4 m × 1.2 m × 0.04 m (cut from the original 2.7 m × 1.2 m × 0.04 m), and their main purpose is providing thermal isolation and sound absorption in indoor spaces (Ecophon, 2020). The printer we used is a flatbed Canon Arizona 2280XT, enabled with the VarioDot technology for variable size of the deposited ink drops (Canon, 2020a), and the Touchstone elevated (also known as 2.5D) printing technology (Canon, 2020b). It is a piezoelectric inkjet system; it uses the IJC-257 inks that are polymerized (cured) using UV light right after being deposited on the printing substrate. The elevated print production is achieved through adding up ink layers in several print-and-cure cycles (Canon, 2018). In this work, we investigate the acoustic impact from only one ink layer – as in the con-

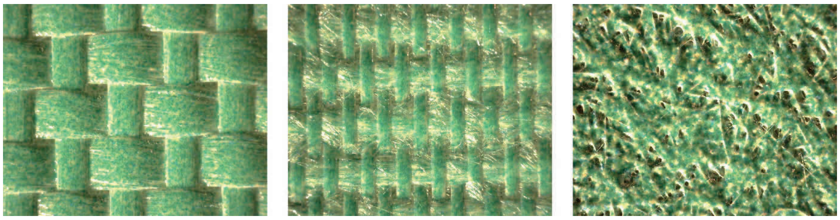
1 2 3

Figure 1: Microscopic surface of the printed sound-absorbing plates of three quality types marked 1, 2, and 3; the physical size of the area shown in all three images is 8 mm × 6 mm

ventional 2D print reproduction. The whole area of the testing plates was printed with one layer of uniform green at 200 % ink – we used full coverage levels of both cyan and yellow. The amount of deposited ink was selected so that it emulates 2D prints with moderate-to-high ink coverage; the uniformity of the print was to ensure uniform sound-absorbing properties of the printed surface and contribute towards reducing the measurement noise. Figure 1 shows microscopic view of each of the three printed plates.

For the sound absorption measurement, we followed guidelines from the ISO 354:2003 standard (International Organization for Standardization, 2003). This standard specifies the room characteristics, the mounting of the measured plates, the methods for measurement of the reverberation time as well as the subsequent calculation of the sound absorption curve. The size of our reverberation room is 2.7 m × 3.84 m, and it is 2.6 m high. The testing plates were mounted on a wall in the reverberation room by tiling two plates to an effective area of 2.4 m × 2.4 m. Metal fasteners were used to ensure they fit tightly to the wall. An example of the mounted plates in the reverberation room is shown in Figure 2.

Figure 2: One of the printed plates mounted on the wall in the reverberation room; the omnidirectional loudspeaker and microphone are also shown

The volume of the reverberation room (27 m^3) is considerably below the recommended minimum of 150 m^3 (International Organization for Standardization, 2003) and it is the main limitation of our measurement setup. While the measurements of the reverberation time in this work may therefore not be absolutely correct, we believe that this has limited impact on our study – it is a comparative analysis of sound absorption of different materials, calculated using repeated measurements in the same conditions. Furthermore, given that “the minimum volume of the room depends on how low in frequency valid measurements are to be taken” (Vér and Beranek, 2006, p. 85), the potential measurement errors due to spatial non-uniformities in the sound intensity are expected for the lower frequencies. For example, if measurements are to be done down to the 200 Hz band, then a room volume of 70 m^3 would be acceptable (Vér and Beranek, 2006, p. 85).

The reverberation time is measured using the interrupted noise method (International Organization for Standardization, 2003). The reverberation room is excited for around 5 s with a pink noise with continuous spectrum from an omnidirectional loudspeaker, Norsonic Nor276, driven by the power amplifier Norsonic Nor280, to create a diffuse sound field in the room. A free-field microphone, Norsonic Nor1225, coupled with the sound analyzer Norsonic Nor140, is used to record the SPL during the excitation and for 10 s after the excitation stops. The sound analyzer estimates the decay curve of the SPL and subsequently the reverberation time. As recommended in the ISO 354:2003 standard, we used 20 dB as an evaluation range for the SPL decay; therefore, we label the measured reverberation time as T_{20dB}. The reverberation time itself is normally dependent on frequency. As recommended in the ISO 354:2003 standard, we performed measurements at 18 third-octave frequency bands, ranging from 100 Hz to 5 000 Hz. During the measurements, both temperature and humidity were controlled to reduce variability in sound absorption caused by air at different atmospheric conditions. The number of spatially independent measured reverberation times is six – we used two different positions for the loudspeaker and three different positions for the microphone. In order to reduce the occurrence of acoustical resonances, there were no spatial symmetries regarding the loudspeaker and microphone positions, and their distance from each other and to the surrounding walls, for all of the six different configurations. To obtain statistically independent measurements and avoid non-representative measurements, the microphone positions should be at least half-wavelength apart (for the lowest measured frequency) from each other and also half-wavelength away from any reflecting objects (Vér and Beranek, 2006, p. 210). In our six different configurations, the minimum of the distances between the different microphone positions and between the microphone positions and the nearest reflecting objects was 0.6 m – which is the half-wavelength of a wave at frequency of approximately 286 Hz. According to this requirement, our measurements of the reverberation time for the frequency bands lower than 286 Hz may not be representative.

2.2 Calculation of the sound absorption curve

The reverberation time is calculated as an average of the reverberation times measured for the six different loudspeaker/microphone positions. For calculation of the sound absorption coefficient at each frequency band, two different measurements of the reverberation time are needed – one of an empty reverberation room, and another with the testing plate mounted inside the room. The sound absorption curve $\alpha(f)$ is calculated as a ratio between the equivalent sound-absorbing area, $A_T(f)$, and the actual area of the testing plate, S:

$$\alpha(f) = \frac{A_T(f)}{S} \qquad [1]$$

The equivalent sound-absorbing area of the testing plate is calculated (International Organization for Standardization, 2003) as

$$A_T(f) = 55.3V\left(\frac{1}{c(t_2)T_2(f)} - \frac{1}{c(t_1)T_1(f)}\right) - 4V(m_2 - m_1) \qquad [2]$$

In Equation [2], V is the volume of the reverberation room, expressed in m^3; $c(t_1)$ and $c(t_2)$ are the speed of sound in air at the measurement room temperatures t_1 (during the measurement of an empty room) and t_2 (during the measurement with the testing plates mounted), expressed in m/s. For temperatures t in the range of 15 °C to 30 °C, the speed of sound c is calculated as: $c = 331(1 + 0.6t)$ (International Organization for Standardization, 2003). Furthermore, $T_1(f)$ is the measured reverberation time (T_{20dB}) of the empty room at frequency f, while $T_2(f)$ is the measured reverberation time with the testing plates mounted, both expressed in s. The variables m_1 and m_2 are power attenuation coefficients (expressed in m^{-1}) that account for the climatic conditions in the empty room and with the testing plate mounted, respectively (International Organization for Standardization, 1993). If the climatic conditions in the room (temperature, relative humidity) remain constant during the two measurements, then m_1 and m_2 will cancel out in Equation [2].

In order to reduce the measurement uncertainty, we performed ten measurements of the reverberation time for each loudspeaker/microphone position in all measurement scenarios for the three different plates, i.e., empty room, an unprinted plate mounted, and a printed plate mounted in the room. The average reverberation time of these repeated measurements was used in Equations [1] and [2] for calculating the sound absorption as a function of frequency.

3. Measurement procedure, results, and discussion

The T_{20dB} reverberation time was measured in seven different measurement settings: one for the empty reverberation room, three for the three types of the unprinted sound-absorbing plates mounted on the measurement wall, and another three for the printed ones. The measurements were performed ten times for each of the six different loudspeaker/microphone positions, and for the following third-octave bands (Hz): 100, 125, 160, 200, 250, 315, 400, 500, 630, 800, 1000, 1250, 1600, 2000, 2500, 3150, 4000, and 5000. The total measurement time including mounting/dismounting the plates in the reverberation room was around 3.5 hours. For a very small number of measurements at the lowest two frequency bands (100 Hz and 125 Hz), the sound analyzer did not report the T_{20dB} times, or the reported times were unusually very high (at least twice the median value) – those measurements were not included in the analysis. The reason for this could lie in the size of our reverberation room – as mentioned before, its volume is below the recommended minimum. This may have resulted in a non-diffuse sound field for the lower frequencies during the excitation (Vér and Beranek, 2006, p. 85), and subsequently, in errors for the estimated reverberation times at these frequency bands.

The average of all 60 measured T_{20dB} times per frequency band for each of the seven setups was used in Equations [1] and [2] for calculating the sound absorption curve. In order to determine the measurement uncertainty, we calculated 10 different sound absorption curves using the average T_{20dB} time for the six loudspeaker/microphone positions; these 10 values were assumed to be samples of a Student's t-distribution, and the confidence intervals were calculated at a 95 % confidence level. The sound absorption curves for the unprinted and printed plates are shown separately for the three quality types of plates in Figures 3–5, respectively. The confidence intervals at each measured frequency band are denoted with dots. They are noticeably larger for the lowest two frequency bands mostly because of the excluded measurements for the reverberation time, which lead to less than 10 calculated values for the sound absorption. In general, for all of the six absorption curves plotted in Figures 3–5, the confidence intervals calculated for the frequency bands in the lower half are larger than those for the higher half. Therefore, we can infer that measurements for the higher frequencies were made with higher precision. It can be seen that the two sound absorption curves for the unprinted and printed plates are very close to each other for each of the three quality types. The confidence intervals overlap at each measured frequency band, and therefore, there is no significant difference in the sound absorption of the plates due to the printing one layer with two inks at full coverage. The same conclusion can be obtained using another test – we performed a two-sided sign test to check whether the difference in sound absorption between unprinted and printed plates came from a distribution whose median is not zero. For all three quality types, the sign test could not reject the null hypothesis ("the median difference is zero") as the *p*-values were above 0.7 in all three cases.

As previously mentioned, due to the small distances between the microphone locations and the surrounding reflective walls in the room, our measurements for the bands lower than 286 Hz may not be representative. Another property of our room that indicates inaccurate measurements for the lower bands is the Schroeder frequency (Schroeder, 1962). This frequency is considered as a transition frequency between the low-frequency region, where acoustical resonances in the form of standing waves at the discrete room's natural frequencies are dominant, and the high-frequency region, where the sound field is spatially more uniform and can be statistically described (Vér and Beranek, 2006, p. 209). The reverberation time of our empty room averaged over 10 measurements and all frequency bands is 3.05 s, resulting in an estimated Schroeder frequency of 673 Hz. This value is relatively high mostly because of the small room volume that is used in the calculation. For small rooms, the statistical properties of the frequency response even at half of the Schroeder frequency can be indistinguishable from that of the high-frequency region (Skålevik, 2011). However, the impact of acoustical resonances in our room appears to be significant, and it may be the reason behind the larger differences in measured sound absorption between adjacent bands lower than 800 Hz, which can be observed for all six plates in Figures 3–5. These differences are similarly distributed across the low-frequency region for all of the plates – most probably because of the same measurement conditions (regarding the positions of the plates, the loudspeaker and the microphone) which resulted in specific and consistent statistical properties of the sound field during our measurements.

In general, non-diffuse sound field is the reason behind high variability in sound absorption measurements according to the ISO 354:2003 standard (Vercammen and Lautenbach, 2016). This variability can be reduced, e.g., by calibration that uses a reference absorber (Vercammen, 2010). While not meeting the recommendations from the ISO 354:2003 standard regarding the size of our room may have led to incorrect values calculated for the absorption curves, we think that this has limited relevance for our goal – we are comparing the absorption curves between printed and unprinted plates, i.e., investigating the difference between them.

Even though our measurements were not performed in fully diffuse conditions, we believe that the statistical properties of the non-diffuse sound field did not vary significantly between and during both measurements – as they were performed in the same conditions regarding the positioning of materials and equipment. The average error we make in absolute sense due to the non-diffuse conditions during the measurements of $T_{20\mathrm{dB}}$, and therefore on the sound absorption coefficients, are expected to be the same for both measurements and effectively cancel out in our analysis that looks only at the difference in sound absorptions. The small and insignificant differences in sound absorption between printed and unprinted plates for the higher frequencies (for which the small size of the room had less contribution to a non-diffuse sound field, and therefore, to inaccurate measurements of the reverberation time) was also observed for the lower frequencies (that are more affected by the small size of the room). From our measurement setup and analysis, we do not have a strong reason to believe that there might be a significant difference in sound absorption for the lower frequencies, which was not able to be detected with our limited setup. However, such claim can be supported by performing the measurements in full compliance with the ISO 354:2003 standard.

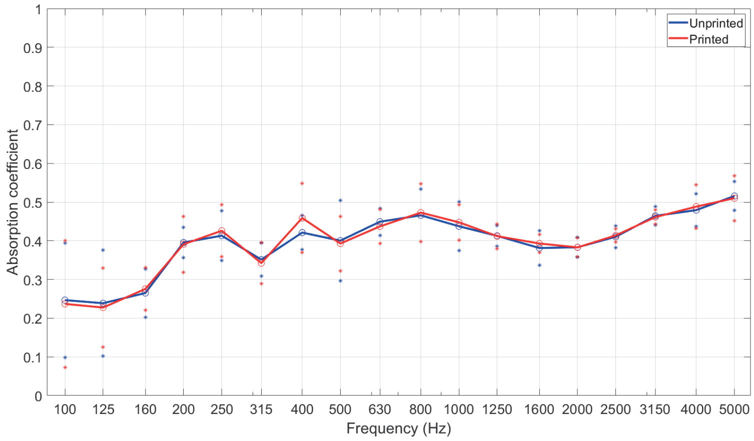

Figure 3: Average sound absorption coefficients with 95 % confidence intervals for the unprinted and printed plates for quality type 1; the averaged measured values are shown with circles

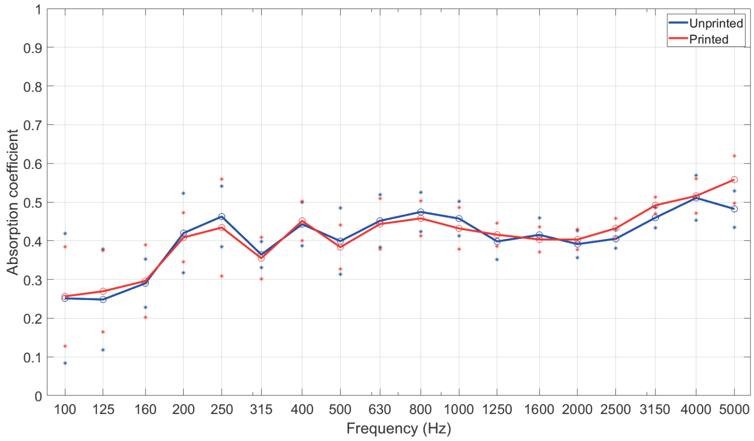

Figure 4: Average sound absorption coefficients with 95 % confidence intervals for the unprinted and printed plates for quality type 2; the averaged measured values are shown with circles

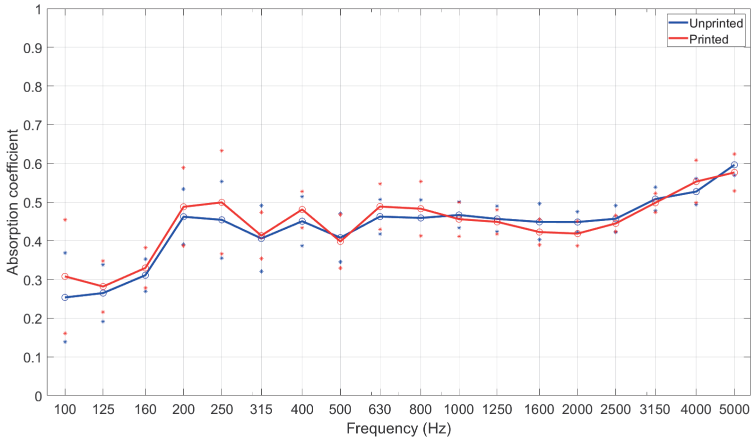

Figure 5: Average sound absorption coefficients with 95 % confidence intervals for the unprinted and printed plates for quality type 3; the averaged measured values are shown with circles

4. Conclusion

In this work, we investigated the impact on sound absorption from printed UV-cured inks on sound-absorbing plates with three different types of surface finishing. We printed only one layer with moderate ink amount – which is sufficient for creating colored décor designs. The sound absorption curves for both printed and unprinted plates were calculated from the reverberation times that were measured in a reverberation room. Our measurement setup was not in full compliance with the ISO 354:2003 standard for measurement of sound absorption, and therefore, the sound absorption measurements are not accurate in absolute sense. However, due to the same measurement conditions, the difference in sound absorption between printed and unprinted plates should still be valid. It was found to be very small, and according to our analysis not significant. We conclude that there is no impact on sound absorption from printing one layer with UV-cured inks.

Potential directions for future work may be taken towards confirming our conclusion in other reverberation rooms, or towards investigating the impact of printing elevated designs using multiple layers of UV-cured ink on sound absorption.

Acknowledgements

We would like to thank Alf Dalby for providing logistics support regarding the reverberation time measurement, to Pål Jacobsen for providing us with the printing equipment, and to Odd Kr. Pettersen and Guillaume Dutilleux for the useful discussions regarding sound absorption measurement.

References

Beranek, L.L. and Mellow, T.J., 2012. *Acoustics: sound fields and transducers*. Oxford, UK: Academic Press.

Cahill, V.J., 2001. *A short history and current development of UV-curing for ink jet printing*. [pdf] Waynesboro, PA, USA: VCE Solutions. Available at: <http://www.vcesolutions.com/wp-content/uploads/2014/09/A-Short-History-and-Current-Development-of-UV-Curing-for-Ink-Jet-Printing.pdf> [Accessed June 2020].

Canon, 2018. *Canon launches Océ Touchstone elevated printing solution at FESPA 2018*. [online] Available at: <https://www.canon-europe.com/press-centre/press-releases/2018/05/oce-touchstone/> [Accessed 23 March 2020].

Canon, 2020a. *Arizona 2280 XT specifications*. [online] Available at: <https://www.canon-europe.com/for_work/products/large_format_printers/displaygraphics/arizona_2280_xt/specification.html> [Accessed 07 June 2020].

Canon, 2020b. *Canon Touchstone specifications*. [online] Available at: <https://www.canon-europe.com/business-printers-and-faxes/touchstone/specifications/> [Accessed 07 June 2020].

Chrisler, V.L., 1941. Effect of painting on the sound absorption of acoustic materials*. The Journal of the Acoustical Society of America*, 12(3), p. 465. https://doi.org/10.1121/1.1902192.

Ecophon, 2020. *Ecophon Akusto™ Wall Edge A*. [online] Available at: <https://www.ecophon.com/uk/products/Vertical-applications/Akusto/Akusto--Wall-A/> [Accessed 07 June 2020].

Harris, D.A., ed. 1991. Noise control manual: guidelines for problem-solving in the industrial/commercial acoustical environment. New York, USA: Springer.

International Organization for Standardization, 1993. *ISO 9613-1:1993 Acoustics — Attenuation of sound during propagation outdoors — Part 1: Calculation of the absorption of sound by the atmosphere.* Geneva: ISO.

International Organization for Standardization, 2003. *ISO 354:2003 Acoustics — Measurement of sound absorption in a reverberation room*. Geneva: ISO.

Ivanova, Y., Vitchev, P. and Hristodorova, D., 2018. Study on the influence of some factors on the sound absorption characteristics of wood from Scots pine. *Chip and Chipless Woodworking Processes*, 11(1), pp. 65–72.

Martellotta, F. and Castiglione, M.L., 2011. On the use of paintings and tapestries as sound absorbing materials. In: *Proceedings of Forum Acusticum 2011*. Aalborg, Denmark, 27 June – 01 July 2011. European Acoustical Association.

Parraman, C., 2012. Colour print workflow and methods for multilayering of colour and decorative inks using UV inkjet for fine art printing. In: *Proceedings SPIE 8292, Color Imaging XVII: Displaying, Processing, Hardcopy, and Applications*. Burlingame, USA, 24–26 January 2012. SPIE. https://doi.org/10.1117/12.909864.

Parraman, C. and Ortiz Segovia, M.V., 2018. *2.5D printing: bridging the gap between 2D and 3D applications*. Hoboken, NJ, USA: John Wiley & Sons.

Sayako, A. and Yamamoto, H., Riso Kagaku Corporation, 2018. *Surface treatment liquid for porous sound-absorbing material, aqueous inkjet ink for porous sound-absorbing material, and uses therefor*., U.S. Pat. 9,937,709.

Schroeder, M.R., 1962. Frequency-correlation functions of frequency responses in rooms. *The Journal of the Acoustical Society of America*, 34(12), pp. 1819–1823. https://doi.org/10.1121/1.1909136.

Skålevik, M., 2011. Schroeder frequency revisited. In: *Proceedings of Forum Acusticum 2011*. Aalborg, Denmark, 27 June – 01 July 2011. European Acoustical Association.

Taylor, D.H. and Cahill, V., 2015. Energy curing: UV/EB printing for food packaging. In: *Converting & Package Printing Expo Conference Series 2015.* Chicago, IL, USA, 13–16 September 2015. http://dx.doi.org/10.13140/RG.2.1.4886.8887.

Vercammen, M.L.S., 2010. Improving the accuracy of sound absorption measurement according to ISO 354. In: *Proceedings of the International Symposium on Room Acoustics, ISRA 2010*. Melbourne, Australia, 29–31 August 2010. Melbourne, Victoria, Australia: Australian Acoustical Society.

Vercammen, M. and Lautenbach, M., 2016. Non diffuse sound field in the reverberation room. In: F. Miyara, E. Accolti, V. Pasch and N. Vechiatti, eds. *Proceedings of the 22nd International Congress on Acoustics*. Buenos Aires, Argentina, 5–9 September 2016. Buenos Aires, Argentina: Asociación de Acústicos Argentinos.

Vér, I.L. and Beranek, L.L., eds. 2006. *Noise and vibration control engineering: principles and applications*. 2nd ed. Hoboken, NJ, USA: John Wiley & Sons.

Xu, W., Fang, X., Han, J., Wu, Z. and Zhang, J., 2020. Effect of coating thickness on sound absorption property of four wood species commonly used for piano soundboards. *Wood and Fiber Science*, 52(1), pp. 28–43. https://doi.org/10.22382/wfs-2020-004.

JPMTR 135 | 2009
DOI 10.14622/JPMTR-2009
UDC 676.22-023.881-021.465

Case study
Received: 2020-05-04
Accepted: 2020-06-16

Influence of paperboard production on web movement and register quality in printing process

Tobias Enk[1], *Peter Urban*[1], *Michael Dattner*[2], *Hannes Vomhoff*[3] *and Axel Heise*[4]

[1] University of Wuppertal, School of Electrical, Information and Media Engineering,
Rainer-Gruenter-Straße 21, D-42119 Wuppertal
[2] Beuth University of Applied Sciences Berlin,
School of Information Technology and Media,
Luxemburger Straße 10, D-13353 Berlin
[3] Holmen AB, Strandvägen 1, SE-114 84 Stockholm
[4] Gundlach Verpackung GmbH,
Hellweg 21-25, D-33813 Oerlinghausen

toenk@uni-wuppertal.de
purban@uni-wuppertal.de
michael.dattner@beuth-hochschule.de
hannes.vomhoff@holmen.com
axel.heise@gundlach.de

Abstract

Register quality is often influenced by challenging web runnability. For fiber-based materials like paperboard it can be originated in the boardmaking process and tried to be compensated by web guiding and register control systems in printing process. Within an interdisciplinary research cooperation with different participants along the value chain of paperboard packaging production, the influence of different paperboard production conditions and register control strategies on web movement and register quality in a production scale gravure printing machine was performed in this study. Based on different boardmaking conditions, 13 different paperboard qualities were produced and each printed with 3 different register control strategies. The resulting register quality in cross direction (CD) and machine direction (MD) were measured as well as web movement, web tension and web moisture with several sensors along the printing machine. To assign the root causes of paperboard-induced web movement to boardmaking conditions, mechanical properties like tensile stiffness index in MD and CD and tensile stiffness orientation of the paperboard material have been measured and compared with data on web movement in the printing press. Further, web edge data were analyzed in frequency domain, to assign characteristic frequency components to their different mechanical root causes in boardmaking and printing process. It was found that CD position on tambour is the most influential board side parameter on lateral web movement and register quality. The lateral web shift differs significantly for middle and edge reels. Main reason for misregister in this study was attributed to board side slow lateral web movements with increasing amplitudes along the printing press. A register control strategy with an increasing gain per printing unit was most effective to improve register quality for this runnability behavior.

Keywords: board production conditions, register control strategies, web runnability, lateral web movement, misregister

1. Introduction and background

A key quality parameter of a printing product is its register quality. It means printing the right color at the right place. The register quality affects sharpness and color appearance of a multicolor print. The visibility of misregister is dependent on various influences like ink color, image or screening technology. In general, misregister can be defined as a relative misalignment of printing cylinder to the moving web and the previous printed pattern in cross direction and in machine direction (Kang, Lee and Shin, 2010). This two-dimensional alignment is the task of the register control system in a printing machine in order to get a printed image of high quality. In gravure printing machines, typically, the register controller aligns the printing units to the web, based on register mark measurements.

Most of previous case studies regarding paper web runnability have been carried out for offset printing processes with light-weight coated (LWC), uncoated and super-calendered (SC) papers for newsprint or commercial print goods.

Parent and Hamel (2013) presented how paper mills have worked on improving paper properties to reduce web lateral instability in different case studies with different paper grades and trials in pressrooms and in laboratory.

In two case studies from Parola, et al. (2003), and Paukku, Parola and Vuorinen (2004), data from different paper mills and one printing press were gathered and combined into reel specific key figures and analyzed with a proprietary data mining software. They focus on clarifying the reasons for runnability issues with special attention to lateral web movement and web widening.

Shields, et al. (2018) studied papermaking reasons for lateral shift of a moving paper web made from one particular paper machine on a specific heatset web offset printing press. They tested 11 different paper qualities regarding runnability in this press and regarding water absorption in laboratory. Fiber orientation was found as the most important factor affecting lateral web movement in printing press.

Case studies on gravure printing presses were perfomed by Parola with coworkers but even with SC and LWC paper grades. They found that the cross direction (CD) position of the reel in paper machine is one of the most influential feature regarding variations in web tension profiles and runnability issues (Parola and Beletski, 1999; Parola, et al., 1999).

To accommodate certain reel to reel variability in daily print production, it is a common practice that printers sort the reels by its CD position in paper machine and running them in sequence if they have this information from the producer. Paukku, Parola and Vuorinen (2004) argue that issues with paper side uniformity in machine direction (MD) within a reel have to be solved in paper mills.

Unlike in other studies, in this publication both web runnability and register quality were analyzed. Substrate side and register controller side reasons on register quality were separated through a corresponding experiment design. Further, our study was performed at a production-scale gravure printing press and with multiply paperboard material for folding boxes. To our knowledge, this type of study has not been performed before. Due to its thickness, stiffness and multiply structure it is assumed that this web material has probably different mechanical properties and interaction within the printing process than thin offset papers.

2. Materials and methods

2.1 Substrate manufacturing

The printing trials were performed with a 722 mm width, 3-ply solid bleached board, based on chemical pulp with a grammage of 240 g/m^2, a thickness of 305 µm and a one side coating of approx. 20 g/m^2. The outer plies consist of a virgin fiber hardwood/softwood mixture, while the middle ply comprises a virgin fiber mixture of softwood and broke. In contrast to normal cardboard production run, for the print trials two process conditions in board machine were varied experimentally during the production of the board:

- In order to variate the tensile stiffness (fiber) orientation (TSO_{Angle}) and the tensile stiffness index (TSI) ratio between MD and CD, the speed differ-

Table 1: Specification of reference reel (reel 1)

Specification	Value	Tolerances	Method
Grammage (g/m^2)	240	± 5	ISO 536
Thickness (µm)	305	± 5	ISO 534
Front surface roughness (µm)	1.1	≤ 1.4	ISO 8791-4
Back surface roughness (µm)	4	≤ 5.5	ISO 8791-4
Moisture Content (%)	5.7	± 1	ISO 287
Bending stiffness L&W 5° MD (mN)	18.5	–	ISO 5628
Bending stiffness L&W 5° CD (mN)	7.8	–	ISO 5628
Bending resistance L&W 15° MD (mN)	215	−15	ISO 2493
Bending resistance L&W 15° CD (mN)	90	−15	ISO 2493
Bending moment Traber 15° MD (mNm)	10.4	−15	ISO 2493
Bending moment Traber 15° CD (mNm)	4.3	−15	ISO 2493
Tensile strength MD (kN/m)	18.5	–	ISO 1924-2
Tensile strength CD (kN/m)	10	–	ISO 1924-2
Tearing resistance MD (mN)	2 750	–	ISO 1974
Tearing resistance CD (mN)	3 100	–	ISO 1974

ence between suspension jet flow and forming wire (Δv) were set at three levels: low (2 m/min), medium (6 m/min) and high (10 m/min).

- In order to influence the homogeneity of the fiber distribution, a wire shaker on the middle ply was operated with a frequency of approximately 8 Hz at a production speed of 500 m/min.
- For each of the above 6 combinations of process conditions, one roll from the edge and one from the middle of the board machine were taken.

In addition, a reference reel (reel 1) from a normal board production run was evaluated. In total, 13 different reels were evaluated.

The MD variation of the web properties TSI_{MD}, TSI_{CD}, TSO_{Angle}, thickness, and grammage are most important for the behavior of the web in the printing press (Parent, 2015). These properties were measured over the last 200 m of three of the randomly chosen roll qualities at the mill every 40 mm (corresponding to a wavenumber of 25 m^{-1}) according to the measurement principle described in Loewen (2004).

The experimental cardboard is based on a reference production (reel 1) with specifications (measured in test climate 23 °C and 50 % relative humidity) listed in Table 1. Experimental cardboard reels differ from this standard production. So the specifications are not fully valid for experimental cardboard reels used in the print trials. The table only gives a rough impression of the structure and nature of the used substrates.

2.2 Printing machine

Trials were run on a 178 m long production scale roll-to-sheet rotogravure press with 11 printing units (PU), numbered 2 to 12, and embossing unit (EMB) which is driven by a mechanical line shaft (Figure 1). The printing machine consist also of an unwinder, a tension control system, a web guiding system Compact Guide (BST eltromat International, 2017a; 2017b) for compensation of lateral web displacements of the unwinder., followed by the infeed pull unit. In the 134 m long printing section are 11 equal PUs. Inks are dried directly after each PU. After PU8 there is an edge cutting unit for cleaning the web edge for packaging converting processes in the sheeter. After the printing section, there is an optional outfeed pull unit for the sheeter or the rewinder.

2.3 Register controller

The register is controlled by two-dimensional feedback register control system regi_star 20 (BST eltromat International, 2015), which is based on a discontinuous 3-state controller with hysteresis and dead band. The register is measured in each PU over one triangle register mark per print cylinder rotation (printing length) on the operating side (OS), see Figure 2. Depending on the control strategy, this measurement is referenced to the first color or to the previous color. This value represents the control systems data input as the control deviation.

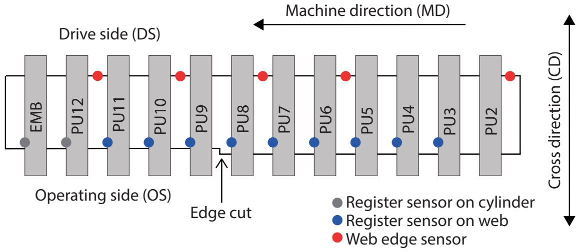

Figure 2: Principal top view drawing of printing machine with web edge and register sensor positions

The MD register is set by a compensator actuator which lengthens the web span between printing units. The CD register is set by a CD movement of the printing cylinder.

For the trials the CD control strategies were variated with 5 different parameter settings marked A to E (Table 2), with constant deadband of 0.02 mm, hysteresis of 0.02 mm and without increasing gain (D-portion equal 0). For MD register control, only the default setting and a deactivated controller was used. The measurements are referenced to the first color or to the previous color, depending on the used control strategy. A praxis relevant maximal register tolerance of ± 0.15 mm in CD and MD was defined for the trial.

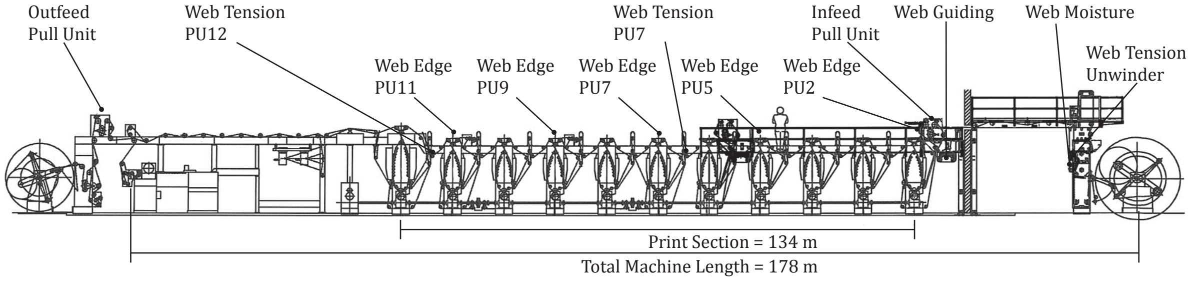

Figure 1: Production scale gravure printing machine equiped for experiments

Table 2: List of register control settings per control strategy

Controller setting	Strategy	Time const. low pass filter	Feedback const. [ms]	Feedback gain [ms]	Ref. color
A	default	3	800	950	first
B	off	–	–	–	–
C	low pass filter	4	950	750	first
D	increasing gain per PU	3	800	450 +200 per PU	first
E	sequential controlling	3	800	450 +200 per PU	previous

2.4 Print job

The trial was performed by running a 10 color and embossing job with 722 mm web width and 32 products per sheet. The first active PU was PU3 and cylinder diameter was 309.24 mm (corresponds to a rapport of 972 mm). Because of the big number of products per sheet, the ink is homogeneously distributed in MD and CD.

In general, ink specific parameters like ink absorbance, ink area coverage or ink sequence for this type of substrate are considered negligible. One reason is that the printed ink layer thickness with approx. 1–5 µm is very small relative to cardboard thickness of 305 µm. Another reason is that ink has not time to penetrate into the cardboard, due to direct drying after each printing unit and the coated surface of the substrate. This is fundamentally different to offset case studies with thin offset papers. This assumption is supported by daily production run observations for this machine. Web run issues occur more frequently with thicker substrate materials than for thinner, independent on ink sequence, ink viscosity and print job. Nevertheless the specific ink sequence, ink types and ink flow rates (viscosities) used in the experiment are listed in Table 3.

Table 3: PU sequence and properties of inks used

Unit	Color	Ink type	Flow rate [s]*
PU2	–	–	–
PU3	spot color	solvent based	27
PU4	magenta	solvent based	24
PU5	cyan	solvent based	25
PU6	yellow	solvent based	25
PU7	spot color	solvent based	28
PU8	spot color	solvent based	29
PU9	black	solvent based	25
PU10	lacquer	solvent based	29
PU11	lacquer	UV curing	31
PU12	lacquer	UV curing	23
EMB	embossing	male/female	–

*(3 mm flow cup DIN 53211)

For a meaningful analysis, only the register controller settings were changed. All other printing conditions were kept constant:

- Web speed: 2.5 m/s
- Print cylinder pressure: 12 kN
- Dryer temperature: ~85 °C
- Pull unit forces: 1st pull unit = 590 N;
  2nd pull unit = 650 N

For this study, the printing machine was specially equipped with the following sensors:

- five web edge sensors CLS Pro 600 (BST eltromat International, 2017c), on the drive side (DS) (Figure 2) after printing units 2, 5, 7, 9, 11 with sampling rate of 100 Hz and resolution of 0.005 mm

- four web tension measurement rollers with strain gauges at the unwinder, 1st pull unit, PU7, PU12 and EMB

- one infrared web moisture sensor NDC IG710e (NDC Infrared Engineering, 2010) directly after unwinding

2.5 Trial plan

The different parameters in the boardmaking process and print process described before, led to trial plan shown in Table 4, where each parameter combination is denoted with an identification number (ID). Each reel was started and ended with the default register controller setting A, to run the reel change with the same controller setting.

2.6 Data recording and pre-processing

All printing machine measurements were collected from a process data recording system (iba System, 2019) with a rate of 100 Hz, independent of the real sensor specific measurement rate. In this context missing values were filled with the last true measurement value. For a web speed independent data analysis, the

Table 4: Trial plan with all combinations of boardmaking conditions and register control strategies in CD and MD, denoted with experiment IDs

Boardmaking Process				**Reel number**	**Printing Process**						
Boardmaking conditions					CD and MD register control strategies						
Name:	Δ*v*	WS	CDP		Name:	A	B	C	D	E	A2
Parameter:	Jet/wire Δ*v* [m/min]	Wire shaker	CD position on tambour		MD:	Default	Off	Default	Default	Default	Default
					CD:	Default	Off	Low pass filter	Increasing gain	Previous color ref.	Default
Value:	Default	Off	Middle	1 (ref.)	Experiment ID:	1	2	4	5	6	7
	2	On	Middle	2		10	11	13	14	15	16
	2	On	Edge	3		19	20	22	23	24	25
	2	Off	Middle	4		28	29	31	32	33	34
	2	Off	Edge	5		37	38	40	41	42	43
	6	Off	Middle	6		46	47	49	50	51	52
	6	Off	Edge	7		55	56	58	59	60	61
	6	On	Middle	8		64	65	67	68	69	70
	6	On	Edge	9		73	74	76	77	78	79
	10	On	Middle	10		82	83	85	86	87	88
	10	On	Edge	11		91	92	94	95	96	97
	10	Off	Middle	12		100	101	103	104	105	106
	10	Off	Edge	13		109	110	112	113	114	115

sensor data were first aligned via their time constant τ, according to its positioning in the printing machine L and the web speed v (Equation [1]).

$$\tau = \frac{L}{v} \qquad [1]$$

Then they were resampled to a new discrete base with a sampling rate of 0.025 m (corresponding to a wavenumber of 40 m^{-1}). In this way the comparison of web movement frequencies in print process and boardmaking process can be done much easily. The register error measurements from setting E were summed up over CD and MD, to make these data comparable to the data of the other register strategies with first color as it’s reference. To eliminate non steady-state conditions due to changes of register control strategy, we eliminated the first and the last 20 % data of each experiment ID.

2.7 Statistical evaluation

The pre-processed data were evaluated quantitatively mainly by two statistical values. Due to the steady-state process conditions without any machine operator intervention it was expected that register data and web movement data are normal distributed around their mean value. Each experiment ID consists of approximately 500 m steady state condition process data. Representative for each experiment ID, we checked register, web edge, web tension and web moisture data of ID1 at PU9 for normal distribution with probability analysis like the example in Figure 3.

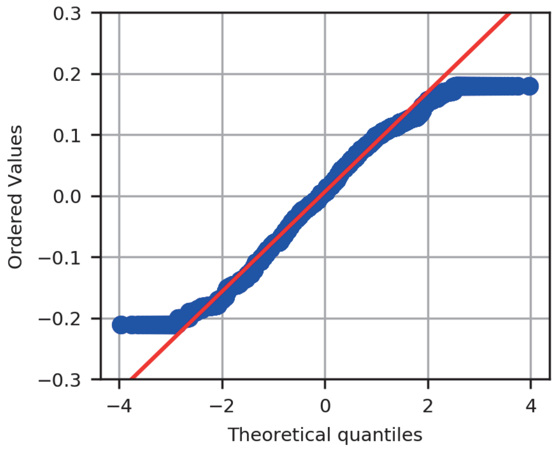

Figure 3: Exemplary probability plot of a pre-processed experiment ID data sample (CD register data of ID1)

Due to the normal distribution and the amount of data, it is permissible to calculate statistical quantities such as the arithmetic mean or the standard deviation (σ) with statistical certainty in order to derive statements about the lateral web shift or web movement.

2.8 Summary

Approximately 72 000 m of experimental paperboard material produced at 13 different process conditions were winded to 13 reels. These reels were then printed at steady-state conditions. The register quality was controlled with five different register control strategies and the lateral web movement was measured with five high-resolution web edge sensors. In addition, the web moisture and the web tension were also measured online.

All measurements had the following objectives:

- Quantify the influence of paperboard production parameters on:
  - Web movement characteristic along the printing press
  - CD and MD register quality depending on different register controller strategies
- Assign the root causes of paperboard-based web movements to board production
- Detect critical web movement wavelength for the register controller used

At the end, the most important quantitative statistical results will be summarized in a single table to assign the conditions in boardmaking process to the effects in printing process.

3. Results and discussion

3.1 Web runnability

The relative lateral web shift along the printing machine was calculated via the mean values per PU of the web edge data, relative to the data of reference reel 1. Only data with deactivated register controller (setting B) were used to get only the natural web movement without any impact of cylinder movements due to register controlling. Figure 4 shows the observed clear clustering of middle (solid black lines) and edge (dashed blue lines) reels. Furthermore, the relative web shift to the reference reel is approximately linear along the press.

The lateral web movement within the general lateral web position was quantified as standard deviation σ of the web edge data per PU. It was found that the web movement basically increases along the printing press (Figure 5). A clear clustering of middle and edge reels can also be observed here. The red line marks the praxis relevant register quality specification limit of 0.15 mm as comparative value.

3.2 Register quality

The CD register quality was determined analogously to lateral web movement via σ over printing units. This analysis was done for all control strategies starting with setting A (Figure 6) as default control strategy, B (Figure 7) as deactivation of register controlling and followed by the experimental strategies of C (Figure 8), D (Figure 9) and E (Figure 10). The red line marks the praxis relevant register quality specification limit of 0.15 mm again.

The CD register quality statistics show similar tendencies to web movement results. The error increases along the printing press and the same clustering of middle and edge reels can be observed in register quality. It becomes obvious that register quality is dependent on web movement characteristics. In our case, the CD register control strategy with the parameter set with the increasing gain (setting D) performed significantly better than the default control setting (setting A), which is optimized for a wideband material portfolio, working sufficiently for most of the production, but it is not optimized for special effects. The experimental setting C shows only slightly better results due to its low pass filter. Setting E as a control strategy, where the previous color is the respective reference color was completely out of tolerance. It underlines that this strategy does not work well for more than three colors, because of its accumulation of errors. In general, it can be assumed that an increasing gain of control can help to keep register error small for long printing machines with this kind of web movement characteristic.

- Regarding the influence of control strategies, setting D is best and setting E is worst for CD register quality.
- Regarding boardmaking conditions, edge reels show best and middle reels show worst register quality. No significant influence of the wire shaker or the jet/wire speed difference in CD register statistics could be observed.

In MD the register quality was nearly constant for activated register controller over all material qualities. Unlike for default CD register (Figure 6), no increasing σ can be observed (Figure 11), although the σ increase is significant for deactivated register controller (Figure 12). As expected, the reference reel shows the best natural runnability result in MD.

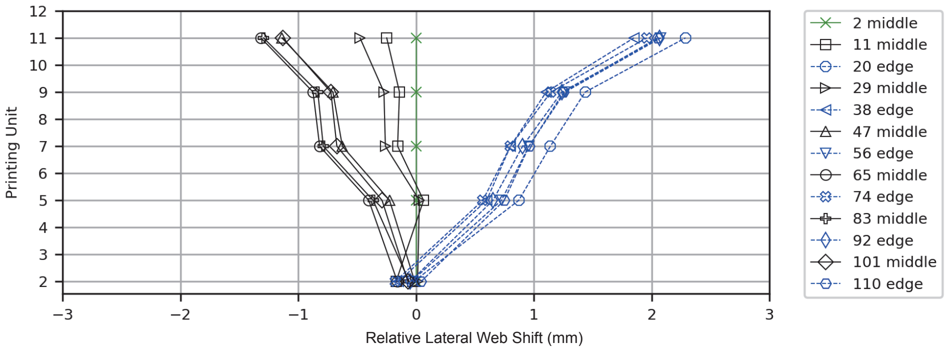

Figure 4: Natural lateral web shift along the printing machine shows clear difference in runnability for middle (solid black lines) and edge (dashed blue lines) reels relative to the reference reel (green)

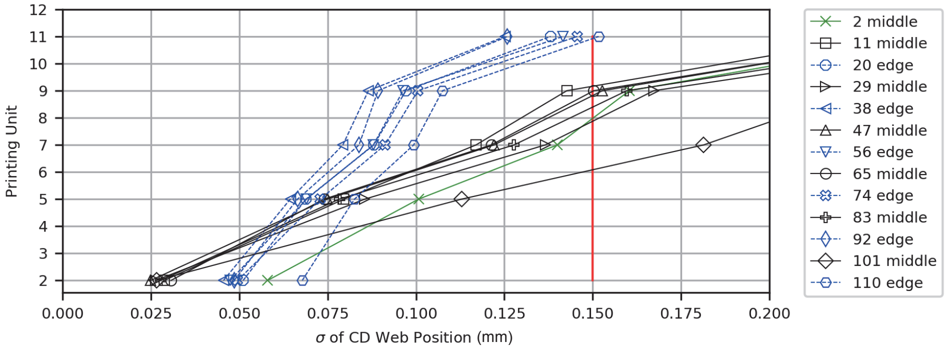

Figure 5: Natural lateral web movement along the printing machine shows clear difference for middle (solid black lines) and edge (dashed blue lines) reels with increasing deviations along the printing machine

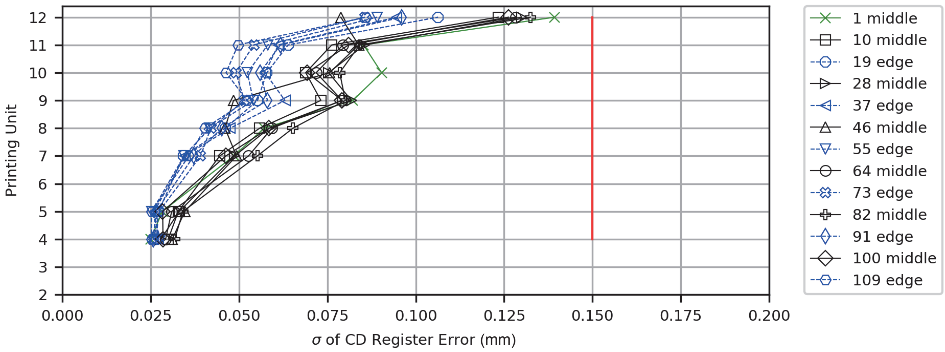

Figure 6: CD register quality standard deviation for register control setting A for middle (solid black lines) and edge (dashed blue lines) reels with increasing deviations along the printing machine

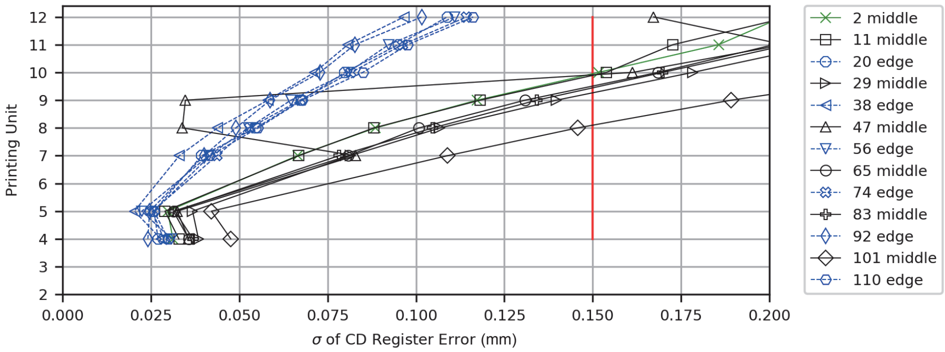

Figure 7: CD register quality standard deviation for register control setting B (natural lateral web movement) for middle (solid black lines) and (dashed blue lines) edge reels with increasing deviations along the printing machine

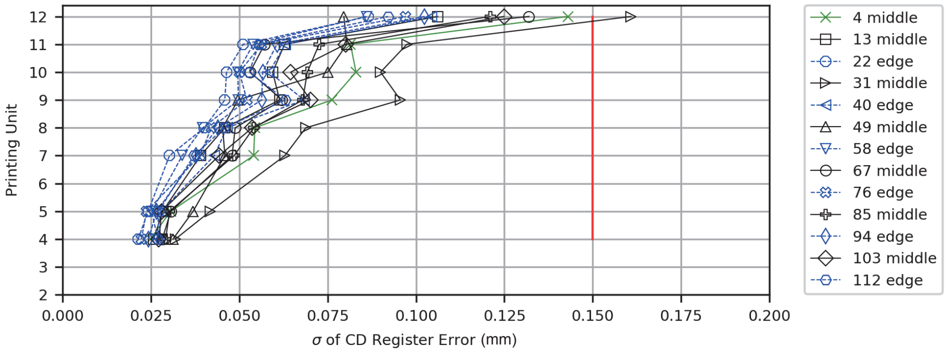

Figure 8: CD register quality standard deviation for register control setting C for middle (solid black lines) and edge (dashed blue lines) reels with increasing deviations along the printing machine

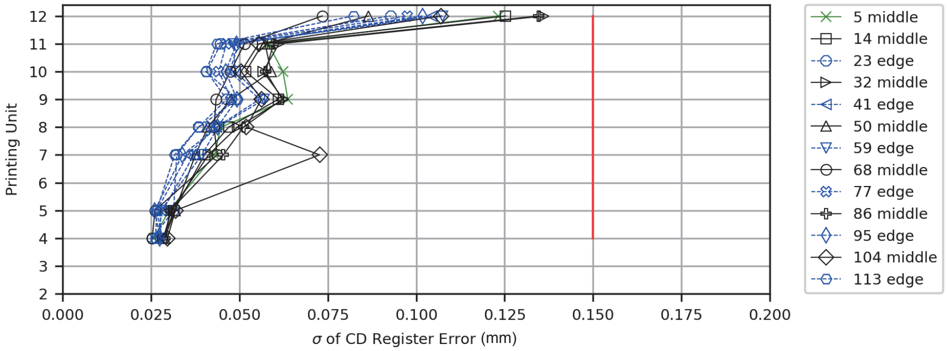

Figure 9: CD register quality standard deviation for register control setting D for middle (solid black lines) and edge (dashed blue lines) reels with increasing deviations along the printing machine

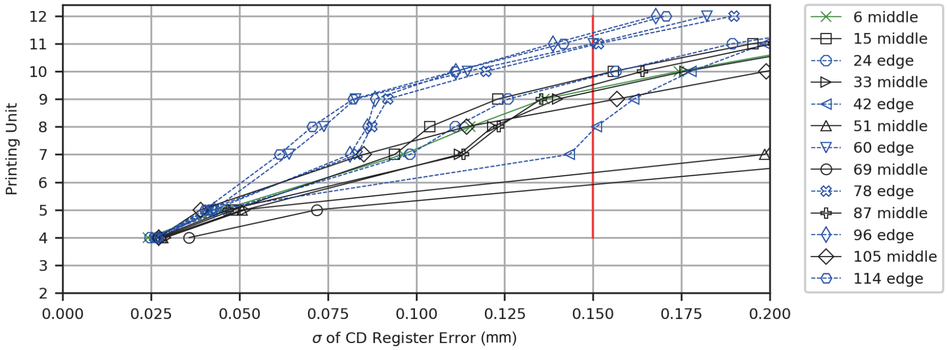

Figure 10: CD register quality standard deviation for register control setting E for middle (solid black lines) and edge (dashed blue lines) reels with increasing deviations along the printing machine

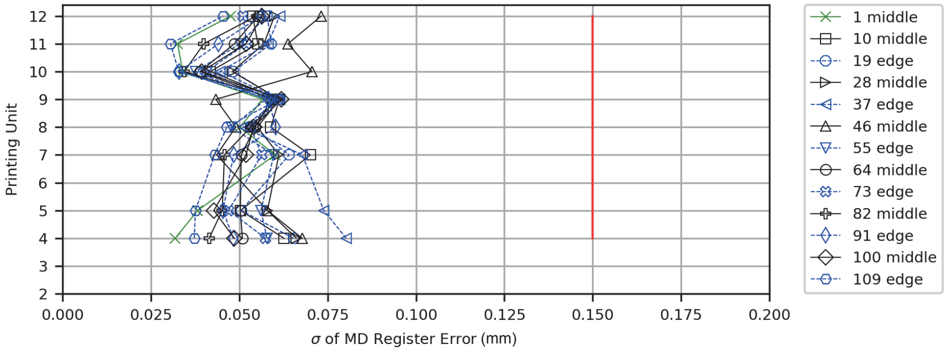

Figure 11: MD register quality standard deviation for register control setting A for middle (solid black lines) and edge (dashed blue lines) reels with similar deviations along the printing machine

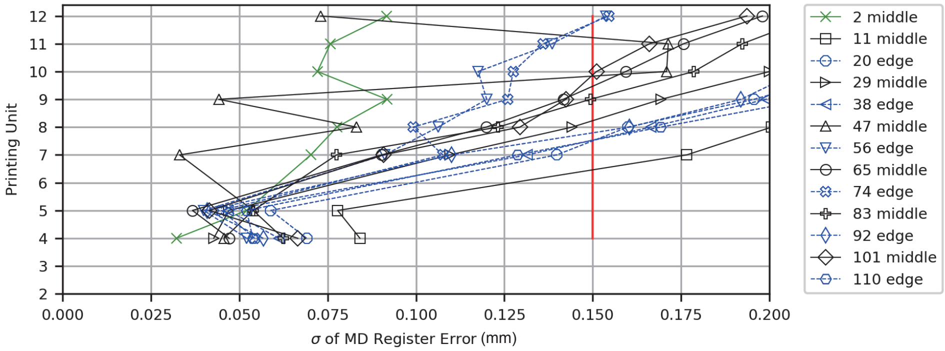

Figure 12: MD register quality standard deviation for register control setting B (natural lateral web movement) for middle (solid black lines) and edge (dashed blue lines) reels with increasing deviations along the printing machine

3.3 Influence of web moisture on web movement

The web moisture measurements in printing machine shows that middle reels had ~1 % more moisture than edge reels, except the reference reel 1 (Figure 13). This observation indicates that the quantities of lateral web movement might have something to do with inhomogeneous web moisture profile in board production.

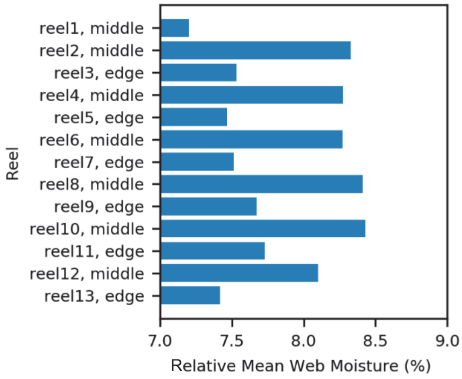

Figure 13: Detected mean web moisture shows clear correlation to CD position of reel on tambour

3.4 Influence of jet/wire speed difference on web tension

A further observation was, that the mean value of web tension in PU7 shows a slight increasing of tension with higher jet/wire speed difference (Figure 14).

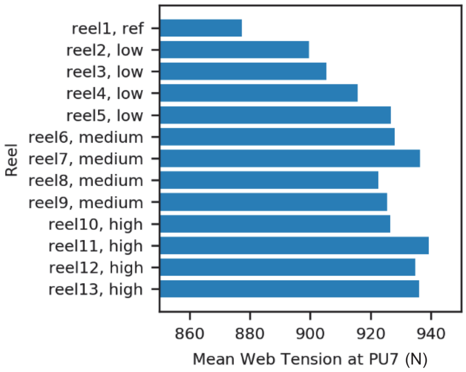

Figure 14: Mean web tension at PU7 shows slight correlation to jet/wire speed difference

This result can be explained by the corresponding TSI_{MD} values due to the different boardmaking conditions

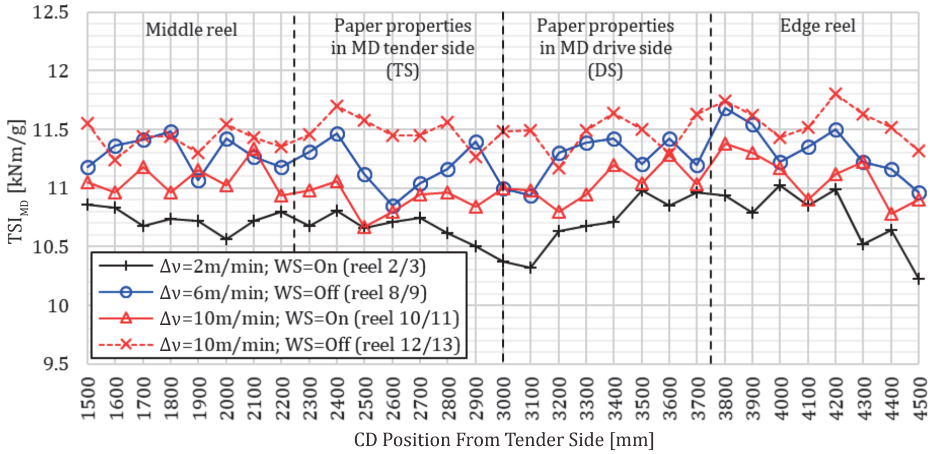

Figure 15: TSI_{MD} profile in CD shows significant influence of jet/wire speed difference and wire shaker (WS) on TSI_{MD} mean value

(Figure 15). As expected, the jet/wire speed difference influenced the TSI_{MD} Level. The higher the speed difference, the higher the TSI_{MD}. However, an activated wire shaker reduces the TSI_{MD} significantly. In addition, the measurements show a typical skew TSI_{MD} profile in CD for edge reels. It is assumed, that this behavior is the main root cause of the different lateral web shift in the printing machine for edge and middle reels.

3.5 Influence of wire shaker on web movement

It was found that the wire shaker parameters have a measureable effect on the fiber orientation. The arrow in (Figure 16) marks the peak in the spectra of reel 3 TSO measurements. The peak at wavenumber 0.8 m^{-1} (1.25 m wavelength) corresponds exactly to shaking frequency of the wire shaker in the board machine.

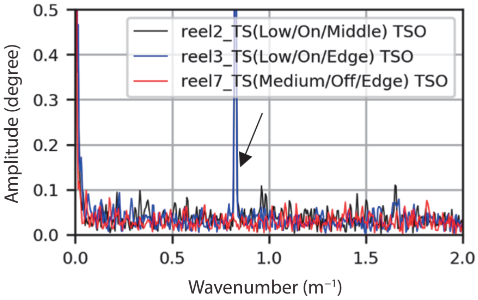

Figure 16: Frequency spectra of TSO_{Angle} in MD

The same peak was also found in web movement spectra of reels with activated wire shaker (Figure 17). But the amplitudes are too small to have a significant impact on the register quality. There are other, much stronger web movement frequencies, which could have a more relevant impact on the register quality. A comprehensive analysis of these frequencies in web edge data is beyond the scope of this work, but it will be part of future work.

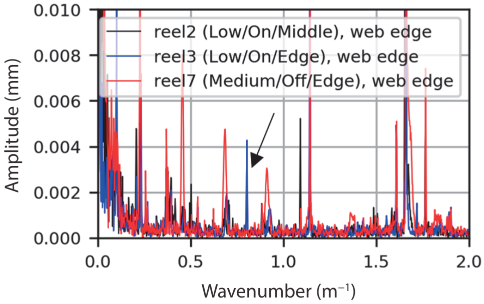

Figure 17: Frequency spectra for web edge data

3.6 Main reason for CD register effects

As most important reason for CD misregister in our study, we detected the web movement characteristics that were slower than 0.1 m^{-1} (corresponds to a wavelength of >10 m) with increasing amplitudes along the printing machine (Figure 18). These growing amplitudes in low frequency range can also be observed in CD register data (Figure 19).

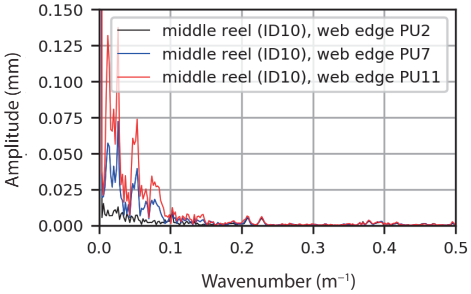

Figure 18: Growing low frequency amplitudes along printing machine in web edge data

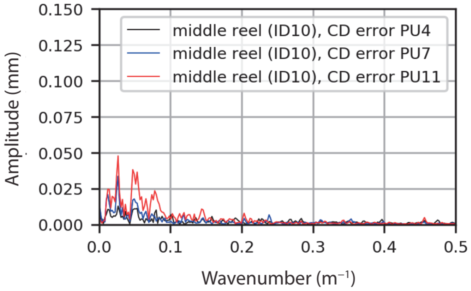

Figure 19: Growing low frequency amplitudes along printing machine in CD register data

The difference in movement behavior in frequency domain of middle reels (black) and edge reels (blue) were analyzed for all register control strategies and show the main reason for differences in web movement characteristic for edge and middle reels (Figure 20).

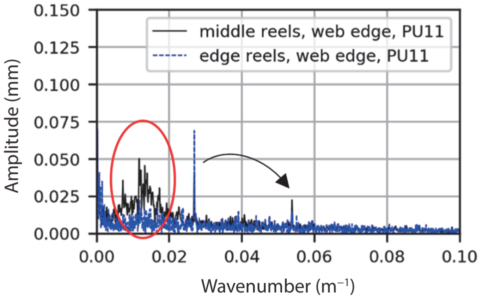

Figure 20: Frequency analysis of dominant slow web movements show significant difference between edge and middle reels

At ~0.015 m^{-1} (67 m wavelength) the spectra of middle reels show a characteristic noisy peak which is much higher than for edge reels. So it seems to be the main reason for differences in register quality between middle and edge reels. The peaks at ~0.025 m^{-1} (40 m wavelength) and ~0.053 m^{-1} (19 m wavelength) appear in both CD positions. It is assumed that the noisy frequency characteristic is originated in the three headboxes at the board machine, due to three paperboard layers. Troubleshooting these pulsations can now be searched for in the boardmaking process.

The most important quantitative results are summarized in Table 5. The table is divided into the boardmaking process and the printing process and shows the results regarding web runnability and register quality by meaningful statistical values, namely the arithmetic mean value (mean) and the standard deviation σ. Lower σ means less web movement or register error issues.

4. Conclusions

The key findings in our research are:

- CD position on tambour is the most influential board parameter on lateral web shift, lateral web movement and CD register quality.
- Jet/wire speed difference has only impact on MD register.
- Wire shaker affects the lateral web movement measurably but has no significant impact on register quality.
- Less lateral web movement results in better register quality for each register control strategy in general.
- The register control strategy with an increasing gain per printing unit resulted in improved register quality with the trial material.
- Board based slow lateral web movements with increasing amplitudes along the press were identified as the main reason for runnability and misregister issues.

In future work we will continue our research to:

- Clarify proportion of web movement within web edge data.
- Investigate dynamic frequency variations in web edge and register data over time.
- Assign frequency components to their root causes in boardmaking or printing process.
- Develop a concept to quantify the register controller efficiency in frequency domain for different web movement signals.
- Search for low frequencies in boardmaking process with noisy characteristic.
- Extend experiment design to evaluate influence of individual paperboard layer regarding headbox pulsation.

Table 5: Heatplot of most important quantitative results seperately in boardmaking and printing process

Boardmaking process				Reel	Printing process										
Production Parameter			Board props.		Web				CD Register					MD Register	
Jet/wire Δv	Wire shaker	CD pos.	TSI_{MD}		Rel. moisture	Tension (PU7)	Lateral shift (PU11)	Lat. movement (PU11)	A (PU11)	B (PU11)	C (PU11)	D (PU11)	E (PU11)	A (PU11)	B (PU11)
			kNm/g		%	N	mm	mm	mm	mm	mm	mm	mm	mm	mm
			mean		mean	mean	mean	σ	σ	σ	σ	σ	σ	σ	σ
x	off	mid.	x	1	7.19	877	0	0.248	0.09	0.19	0.08	0.06	0.22	0.03	0.08
low	on	mid.	10.6	2	8.33	899	−0.558	0.231	0.08	0.17	0.06	0.06	0.20	0.06	0.30
low	on	edge	10.6	3	7.53	905	2.114	0.138	0.06	0.09	0.05	0.04	0.19	0.06	0.24
low	off	mid.	x	4	8.27	915	−0.860	0.270	0.09	0.21	0.10	0.06	0.22	0.06	0.22
low	off	edge	x	5	7.46	926	1.654	0.125	0.06	0.08	0.06	0.05	0.20	0.06	0.25
med.	off	mid.	x	6	8.27	927	−1.435	0.245	0.08	0.20	0.08	0.06	0.26	0.06	0.17
med.	off	edge	x	7	7.50	936	1.938	0.141	0.06	0.09	0.05	0.05	0.15	0.05	0.14
med.	on	mid.	11.3	8	8.40	922	−1.442	0.245	0.08	0.20	0.06	0.05	0.62	0.05	0.18
med.	on	edge	11.3	9	7.67	925	1.809	0.145	0.05	0.10	0.06	0.05	0.15	0.05	0.14
high	on	mid.	11.1	10	8.73	926	−1.458	0.258	0.08	0.21	0.07	0.06	0.20	0.04	0.19
high	on	edge	11.1	11	7.72	939	2.013	0.125	0.06	0.08	0.06	0.05	0.14	0.04	0.23
high	off	mid.	11.5	12	8.10	935	−1.273	0.368	0.08	0.29	0.08	0.06	0.25	0.05	0.17
high	off	edge	11.5	13	7.41	936	1.842	0.151	0.05	0.10	0.06	0.04	0.14	0.03	0.29

Acknowledgements

The authors wish to thank the industrial partners, Gundlach Verpackung, Iggesund Paperboard and BST eltromat International for supporting this research.

References

BST eltromat International, 2015. *Quickly in register: regi_star 20 Register Control*. [pdf] BST eltromat International. Available at: <https://www.bst-eltromat.com/fileadmin/bst-int/download/Brochures/Products/Register_Control/BSTe_B413_EN_regi_star_20_Low.pdf> [Accessed 23 April 2020].

BST eltromat International, 2017a. *Overview: guiding devices*. [pdf] BST eltromat International. Available at: <https://www.bst-eltromat.com/fileadmin/bst-int/download/Brochures/Products/Web_Guiding/BSTe_B403_EN_GuidingDevice_2017_Low.pdf> [Accessed 23 April 2020].

BST eltromat International, 2017b. *Highest precision for guiding your web: BST eltromat Web Guiding*. [pdf] BST eltromat International. Available at: <https://www.bst-eltromat.com/fileadmin/bst-int/download/Brochures/Products/Web_Guiding/BSTe_B303_EN_WebGuiding_2017_Low.pdf> [Accessed 23 April 2020].

BST eltromat International, 2017c. *CLS PRO 600*. [pdf] BST eltromat International. Available at: <https://www.bst-eltromat.com/fileadmin/bst-int/download/Brochures/Products/Web_Guiding/BST_B550_EN_CLS_Pro_600_2017_Low.pdf> [Accessed 23 April 2020].

iba Systems, 2019. *iba System*. [online] Available at: <https://www.iba-ag.com/de/start/> [Accessed April 2020].

Kang, H., Lee, C. and Shin, K., 2010. A novel cross directional register modeling and feedforward control in multi-layer roll-to-roll printing. *Journal of Process Control,* 20(5), pp. 643–652. https://doi.org/10.1016/j.jprocont.2010.02.015.

Loewen, S., 2004. TSO, TSI and fibre orientation optimization. In: *Paper summit, Spring technical, and international environmental conference.* Atlanta, GA, USA, 3–5 May 2004. TAPPI Press.

NDC Infrared Engineering, 2010. *NDC Infrared Engineering: 710e-Reihe Benutzerhandbuch – Messgerättypen: IG710e, SR710e.* [online]. Available at: https://www.directindustry.com/prod/ndc-technologies/product-26204-1806054.html [Accessed 10 May 2020].

Parent, F., 2015. *Troubleshooting with web lateral instability* [online]. Available at: https://flexo-gravure.com/galerie/troubleshooting-with-web-lateral-instability-2/?slide=0 [Accessed 12 September 2015].

Parent, F., and Hamel, J., 2013. Evaluating the impact of non-uniform paper properties on web lateral instability on printing presses. In: *Proceedings of the Twelfth International Conference on Web Handling (IWEB).* Stillwater, OK, USA, 2–5 June 2013. Oklahoma State University, pp. 83–99.

Parola, M., and Beletski, N., 1999. Tension across the paper web – a new important property. In: *Proceedings of the 27th EUCEPA Conference*. Grenoble, France, 11–14 October 1999. Paris, France: ATIP, pp. 293–298.

Parola, M., Sundell, H., Virtanen, J. and Lang, D., 1999. Web tension profile and printing press runnability. In: *Proceedings of the PAPTAC 85th Annual Meeting.* Montreal, Canada, 28–29 January 1999. PAPTAC, pp. 341–348.

Parola, M., Kaljunen, T., Beletski, N. and Paukku, J., 2003. Analysing the printing press runnability by data mining. In: *Proceedings of the 55th TAGA Annual Technical Conference.* Montreal, Canada, 6–9 April 2003. TAGA, pp. 59–60.

Paukku, J., Parola, M. and Vuorinen, S., 2004. Web widening and lateral movements of paper web in a printing press. In: *International Printing & Graphic Arts Conference*. Vancouver, BC, Canada, 4–6 October 2004. IPGAC, pp. 245–250.

Shields, G., Pekarovicova, A., Fleming, P.D. and Pekarovic, J., 2018. Papermaking factors affecting lateral web position during commercial heat set web offset printing. *International Circular of Graphic Education and Research,* 11, pp. 14–23.

TOPICALITIES

Edited by Markéta Držková

CONTENTS

News & more

PRINTING United Alliance

On 1 May 2020, SGIA, the Specialty Graphic Imaging Association primarily serving the graphics, industrial and apparel decorator segments, and PIA, Printing Industries of America primarily serving the commercial printing segment, officially merged and became the largest member-based printing and graphic arts association in the United States. The alliance now works on integration and streamlining of programmes and services from both organisations to better support the graphic arts community.

Much effort has been recently put to activities reacting to the COVID-19 pandemic. In March, PIA demanded print to be considered essential service. Printers and packagers have been specifically included as essential workers in the updated Guidance on the Essential Critical Infrastructure Workforce released on 17 April. Basic facts and situation reports, as well as practical information for both business owners and employees in the graphic arts industry, are provided to assist with safety and recovery.

The countdown to the next drupa continues

While a year ago it was less than 12 months to drupa 2020 and the list of exhibitors featured about 14 hundred companies, the countdown had to be reset due to the COVID-19. Now, ten months before drupa 2021, rescheduled to the end of next April, almost 17 hundred exhibitors are registered. The companies come from over 50 countries, with Germany, China and Italy being the most represented ones. Across the product categories, about 50 exhibitors are currently registered for premedia and multichannel segment, over a hundred for future technologies, and a few hundred in each of the traditional sectors covering prepress and print, post-press, converting and packaging, materials, and equipment, services and infrastructure.

Seventh drupa Global Trends report

The 7th edition of the drupa Global Trends report is based on a survey conducted before the outbreak of the coronavirus, in November 2019. The results published in April build on the responses of 581 printers and 189 suppliers, i.e. a bit less than in the previous edition. When examining the economic confidence, the global net balance was positive, although in the case of printers it was mainly thanks to positive numbers from North America and Europe. The similar pattern across individual regions is seen when comparing the change in revenues, prices, margins and utilisation. Overall, the printer economic confidence shows a decreasing trend in all regions except Africa, where it returned from negative numbers in previous years to a neutral net balance. The decrease is reported in all markets considered, because, besides the market-specific pressures, they all are impacted by broader economic, political and environmental factors. When taking into account the current situation, the need for innovative approaches and adaptability to an ever-evolving demand for print is highlighted.

The annual Intergraf reports

This year, Intergraf, the European Federation for Print and Digital Communication based in Brussels, celebrates its 90th anniversary, being established in Berlin, Germany in 1930 as the International Bureau of the Federations of Master Printers, transformed to Intergraf in 1984, and having a new logo and company brand since last year.

The 2020 Intergraf Economic Report is now available, summarising the available statistical information on the European graphic industry and the related markets, with a new section presenting socio-economic data. The information on current trends in selected European countries is this time provided by Intergraf's member federations from Bulgaria, Denmark, Estonia, France, Germany, Italy, the Netherlands, Norway, Portugal, Sweden, and United Kingdom. Besides the Smithers European print market review with a 4-year forecast (2019–2024), the Intergraf report considers the print market outlook with respect to impacts of Brexit and COVID-19, presenting the UK share in EU print market, UK trade of printed products with EU-27, current European macro-economic forecasts, short-term impacts of COVID-19 situation on advertising, and post-COVID-19 consumption patterns.

These topics are discussed also in the Intergraf Activity Report 2020, together with the restrictions on door-drop advertising, as well as on direct mail and the interpretation and implementation of the General Data Protection Regulation (GDPR) in general, future requirements for printed packaging connected with the introduction of extended producer responsibility schemes and rules on packaging design, review of regulation applicable to food contact materials, the new industrial emissions limit values, and more.

Recent printing-related research at MIT

A study from the Massachusetts Institute of Technology analysed how the perovskite-based solar panels can become competitive with silicon technology. The team from MIT and their co-workers recommend to start with higher-value niche markets and then expand gradually.

Soft, electronically active polymers are 3D-printed in research towards flexible neural implants and other electronic devices at the Department of Mechanical Engineering. To make the low-viscosity conducting polymer solution 3D-printable, it was processed by freeze-drying and embedding into a hydrogel.

Extensive research on 4D printing is carried out by the Self-Assembly Lab and its collaborating partners. Multi-material 3D printing is used to form the objects designed to transform over time as a result of specific conditions, such as due to mechanical stress, water absorption, light exposure, etc.

A method for printing 3D objects that can predictably control living organisms is developed by the Media Lab. In the proof-of-concept experiments, customised combinations of resins and chemicals were printed using a commercially available multi-material inkjet-based 3D printer and the resulting object was spray-coated with a hydrogel containing biologically engineered bacteria. The chemicals then activate certain responses in these microbes, e.g. displaying specific colours or fluorescence. Such hybrid living materials can find a number of applications, including highly specific medical treatments or smart packaging that can detect contamination.

The objects with the structure and function of a breadboard integrated onto their surfaces are 3D-printed by the Computer Science and Artificial Intelligence Laboratory to facilitate testing of circuit functions and user interactions with products such as smart devices and flexible electronics.

Recently completed EU-funded Horizon 2020 projects

The projects finished in 2019 include the large project PI-SCALE – Bringing flexible organic electronics to pilot innovation scale, coordinated by the Dutch research organisation TNO and presented in this section in JPMTR 5(2016)1, and R2R Biofluidics – Large scale micro-and nanofabrication technologies for bioanalytical devices based on R2R imprinting, coordinated by the Austrian FH JOANNEUM. The projects funded within the business innovation support include the two-year SUPPLEPRINT (Super productive line printing inkjet), as well as the short-term ones, such as ATLANT3D (Atomic layer nanoprinter, for rapid micro- and nanoprototyping of complex multi-material 2D/3D structures with high-resolution), T-Sense (Development of temperature sensitive labels for products in cold supply chain), Ribler Technology (Green revolution in bookbinding for print on demand), and PIPER (Printing of ultra-thin, flexible perovskite solar cells and its commercial application). Among the projects funded under the European Research Council (ERC), the Swedish Chalmers University of Technology received the starting grant for its five-year project ThermoTex – Woven and 3D-printed thermoelectric textiles, finished this May. Selected projects are introduced in more detail below.

3DTransducers: Functional 3D printed transducer and sensor systems

The UK University of Strathclyde received the ERC proof-of-concept grant for its 18-month project, utilising the 3D printing techniques from the SASATIN (Soft and Small: Acoustic Transducers Inspired by Nature) ERC project and finished in December 2019. It demonstrated the fabrication of a fully 3D-printed working piezoelectric microphone, comprising conductive, piezoelectric and inert polymer-based parts, in a single integrated build.

HEROIC – High-frequency printed and direct-written organic-hybrid integrated circuits

This five-year project of the Italian IIT research institute finished in this March received the ERC starting grant to radically advance and expand the applicability of polymer-based printed electronics. The published results include complementary organic logic gates on a plastic formed by self-aligned transistors with gravure and inkjet printed dielectric and semiconductors, transparent and highly responsive phototransistors, fully printed photodiodes, ultra-conformable freestanding capacitors, and more.

NECOMADA – Nano-enabled conducting materials accelerating device applicability

This three-year project coordinated by the UK Centre for Process Innovation and finished in December 2019 comprised the development of advanced functional materials for the formulation of customised conductive inks and flexible adhesives, compatible with the roll-to-roll application on flexible substrates via a high-speed pilot line.

InSCOPE – International smart collaborative open-access hybrid printed electronics pilot line

Within another project coordinated by TNO (January 2017 to March 2020), the InSCOPE pilot line comprising printing, component assembly and post-processing was set up and employed for a demonstration of the lighting wall, haptic dashboard, interactive elevator and smart blisters.

Bookshelf

Managing Media and Digital Organizations

Written by an experienced writer and expert in the field, this comprehensive book applies an interdisciplinary approach and provides an in-depth insight into management across the media, communications and information sector. The first part defines the position of media management and introduces the fundamental concepts, presenting the macro-environment of the information economy and the basic microeconomic characteristics of media and information. These include the specific cost structure of media products and services, network effects, divergent cost trends in the value chain, the implications of accelerating progress, excess supply, price deflation, a convergence of technology, non-normal distribution of success, importance of intangible assets, lower emphasis on profitability by many creators, the public-good aspect of information, and high government involvement. Individual chapters in the main three parts of the book then cover the key management functions related to activities in production, marketing and controlling, along with their challenges. All approaches are clearly explained and supported by facts and practical examples. To better illustrate the presented content, a case study following a major media company is included for each chapter. Also, there are review materials to facilitate the use of the book in a course setting.

The main content begins with a chapter on production management. First, it introduces the media production, industries, including print publishing, and success factors. Then it explains the methods and tools for production planning and control. It also covers revenue shares and the impact of next-generation technology. The next chapter discusses technology drivers and trends with their effect on media and communications; it also presents the approaches to research and development management. The following two chapters deal with human resource management, including a discussion of employment in the digital economy, and financing aspects, such as the ownership, partnerships, various funding types, risk reduction strategies and capital structure. Further, intellectual asset management, entertainment law and media regulation are thoroughly discussed, along with the demand analysis and market research for media and information products. The next part brings three chapters that cover in detail the marketing, pricing and distribution of media and information. They deal with product design, positioning, promotion, advertising, marketing performance, pricing strategies, measuring price sensitivity, price discrimination, legal aspects of pricing, distribution networks, distribution management, logistics, distribution channel strategies, etc. Finally, the last part includes the chapters on accounting and strategy planning in media and information firms, discussing profit, liabilities, budgeting, business strategy and internal assessment, among others, and followed by the concluding observations.

While this book is aimed at graduate courses and the professional market, a shorter version for the college level, Media and Digital Management, has been published as well.

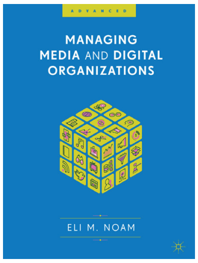

Author: Eli M. Noam

Publisher: Palgrave Macmillan
1st ed., February 2019
ISBN: 978-3-319-71287-1
687 pages, 111 images
Hardcover
Available also as an eBook

3D Printing and Intellectual Property

Author: Lucas S. Osborn

Publisher: Cambridge
University Press
1st ed., September 2019
ISBN: 978-1107150775
242 pages, Hardcover
Also as an eBook

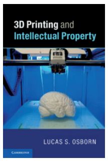

Considering the major intellectual property systems around the world, this book focuses on the issues raised for patent, design, trademark and copyright law by 3D printing, offering ideas for a way forward. First, it outlines the capabilities and effects of 3D printing technology, explaining the way it works and why it matters, and provides the basics of intellectual property law and policy. The next part deals with patents – their applicability to a 3D-printable file and their direct, individual, "digital" and indirect infringement. Further, the book discusses the challenges brought by 3D printing due to the dissociation between design and manufacturing in connection to trademarks, as well as the boundary between copyright and patent protection of 3D-printable files. The last two chapters look at the concepts of design rights, tangibility and free expression, proposing how intellectual property protection can be optimised to better serve as an incentive to innovate.

Jill Enfield's Guide to Photographic Alternative Processes

Popular Historical and Contemporary Techniques

Author: Jill Enfield

Publisher: Routledge
2nd ed., March 2020
ISBN: 978-1138229068
374 pages
Hardcover
Also as an eBook

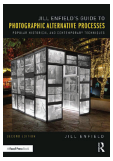

This book on alternative processing of photography is now fully updated to reflect the fast development of technology. The recognised author presents, among others, the

Fundamentals of Image Data Mining

Analysis, Features, Classification and Retrieval

Building upon the author's extensive research in this field, the book provides a timely insight into the approaches to image data mining and helps to gain an understanding of the presented techniques for image analysis, feature extraction, machine learning and image retrieval. The theoretical treatment is complemented by real data and working examples.

The first part explains the Fourier transform, including the short-time Fourier transform and Gabor filters, and wavelet transform. It also demonstrates how these fundamental transforms can be used to capture key information or features in an image. The second part presents the methods for extraction of colour and text features. Further, it describes shape representation and region-based shape feature extraction. The third part then deals with image classification and annotation using four powerful learning machines, presenting the Bayesian classification, support-vector machine, artificial neural network and image annotation with a decision tree. Finally, the fourth part is dedicated to image retrieval and presentation, providing the details on the techniques used for image indexing, ranking and presentation.

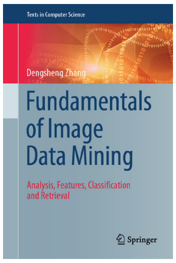

Author: Dengsheng Zhang

Publisher: Springer
1st ed., May 2019
ISBN: 978-3-030-17988-5
314 pages, 202 images
Hardcover
Available also as an eBook

High Dynamic Range Imaging

Sensors and Architectures

Unlike at the time of original publication, much more information on the topic is published now. In ten chapters, this book provides expert knowledge of high dynamic range (HDR) image sensors and techniques for technical applications, in this edition extended by the coverage of CMOS pixel and image sensor design concepts and circuits. After presenting the applications needing a higher dynamic range, main dynamic range concepts and mathematical descriptions, it deals with the existing hardware and software methods to extend the dynamic range, with an emphasis on the commercially utilised ones. Further, the book discusses the optical limitations and automatic HDR control and describes HDR file formats and testing of HDR sensors, cameras and systems. It also covers the dynamic range in infrared and 3D imaging devices and briefly discusses HDR figures of merit.

Author: Arnaud Darmont

Publisher: SPIE Press
2nd ed., April 2019
ISBN: 978-1-5106-2278-4
184 pages
Softcover
Available also as an eBook

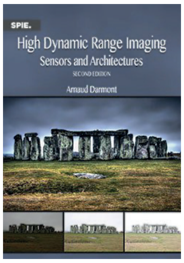

The Cambridge History of the Book in Britain
Volume 7: The Twentieth Century and Beyond

This book is the final volume in the series examining the creation, material production, dissemination and reception of texts in Britain from Roman times to present. Part I deals with the material book and its manufacture, following the development of materials, technologies and the printing industry since the beginning of the 20th century, the format and design of books with respect to illustrations and typography, up to the digital book. Part II is focused on the social, cultural and economic aspects of authorship, publishing, distribution, bookselling, reading and ownership of the book. Part III maps individual market sectors and types of books over the course of the period. Represented sectors or subject areas range from children's books, schoolbooks and textbook publishing, to popular science, popular history, religion, publishing for leisure, museum and art book publishing, music, university presses and academic publishing, scholarly journals, information, reference and government publishing, maps, cartography and geographical publishing, up to magazines and periodicals, comics and graphic novels, i.e. the areas linked more to the newspaper than the book industry. Part IV presents the essays dealing more conceptually with the book in wartime, imperialism and post-imperialism, the book and civil society, sex, race and class, counter-culture and underground, the mass market, intellectual property, books and other media, book events and environments.

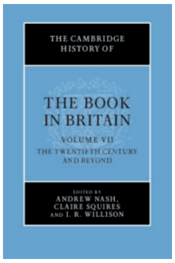

Editors: Andrew Nash, Claire Squires, I. R. Willison

Publisher: Cambridge University Press
1st ed., June 2019
ISBN: 978-1-107-01060-4
780 pages, 17 images
Hardcover
Available also as an eBook

Jan Tschichold and the New Typography
Graphic Design Between the World Wars

This volume highlights the first decades of a career of Jan Tschichold, admired as one of the most influential designers who helped to shape the new typography. Besides his works from this time, the volume is illustrated with images from Tschichold's private collection of illustrations, advertisements, catalogues, posters, magazines and books by both recognised and lesser-known artists and designers. Their analysis provided a new perspective on the work of Jan Tschichold and also on the significant role of advertising designers, members of the group known as "The Ring", in developing a more dynamic, yet balanced language of modern graphic design.

Author: Paul Stirton

Publisher: Yale University Press
1st ed., April, 2019
ISBN: 978-0-300-24395-6
272 pages, 100 images
Softcover

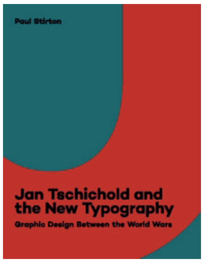

enhanced inkjet prints, utilisation of darkroom techniques in digital image processing, as well as transforming images to 3D installations, showing how all techniques and approaches can be combined to achieve the desired effect.

Ending Book Hunger
Access to Print Across Barriers of Class and Culture

Author: Lea Shaver

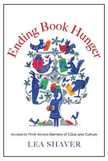

Publisher: Yale University Press
1st ed., February 2020
ISBN: 978-0300226003
224 pages, Hardcover
Also as an eBook

Based on her research on distributive justice aspects of copyright, Lea Shaver stresses the importance of the equal access to books and other educational materials and explores the possible solutions to make them affordable in all languages and regions of the world. The book discusses various distribution models, supply chain innovations, digital publishing, open licenses, copyright exceptions, permissions, and more.

The Art of Coding
The Language of Drawing, Graphics, and Animation

Authors: Mohammad Majid al-Rifaie, Anna Ursyn, Theodor Wyeld

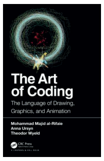

Publisher: CRC Press
1st ed., February 2020
ISBN: 978-0367900373
318 pages
Hardcover
Also as an eBook

The book provides the introduction to coding in general and coding for art, design and applications with different programming languages and data structures. The solutions to the visually oriented tasks show how to create 2D and 3D graphics, modify an image, change the displayed output in time and also how to achieve interactivity and visualise inputs. The complete codes are available online.

Internet of Things
From Hype to Reality
The Road to Digitization

Authors: Ammar Rayes, Samer Salam

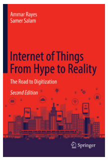

Publisher: Springer
2nd ed., November 2018
ISBN: 978-3319995151
373 pages, 128 images
Hardcover
Also as an eBook

This text presents a timely overview of all important aspects concerning the Internet of Things (IoT) – its core concepts, internet, sensors and actuators, requirements for networking protocols, services, security and privacy, the use cases, the blockchain and open source in IoT, industry organisations and standards.

Applications of Fluoropolymer Films
Properties, Processing, and Products

Author: Jiri George Drobny

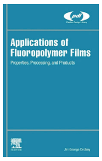

Publisher:
William Andrew
1st ed., February 2020
ISBN: 978-0128161289
314 pages, Hardcover
Also as an eBook

This book provides information about the high-performance films based on fluoroplastic polymers, including the section discussing their printing.

Fluoropolymer Additives

Editors: Sina Ebnesajjad, Richard Morgan

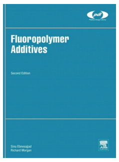

Publisher:
William Andrew
2nd ed., February 2019
ISBN: 978-0128137840
304 pages, Hardcover
Also as an eBook

Published in the same series as the book introduced above, Plastics Design Library, this one presents fluorinated additives, including their applications in printing inks.

Handbook of Silicon Based MEMS Materials and Technologies

With over 130 contributors, this book provides a broad overview of MEMS (micro-electro-mechanical systems) and addresses all areas of concern for the MEMS industry, considering the increasing speed of its development during the last years due to the intense competition and larger business volume, dominated by the consumer business sector. Besides the established technologies, the prospective and emerging ones are also introduced. For the third edition, the content has been reorganised, updated and extended by seven new chapters, reflecting the increasing importance of packaging and reliability of the MEMS devices, and a new part dedicated to process integration and case studies. The individual parts deal with the relevant properties and processing of silicon, modelling methods and micromachining technologies, briefly mentioning also the use of 3D printing technologies and inkjet printing, then with the encapsulation and integration of MEMS, their characterisation, and finally with the examples of applications, namely with accelerometers, gyroscopes, pressure sensors, microphones, micromirrors, and MEMS above CMOS and optical MEMS sensor concepts.

Editors: Markku Tilli, Mervi Paulasto-Krockel, Matthias Petzold, Horst Theuss, Teruaki Motooka, Veikko Lindroos

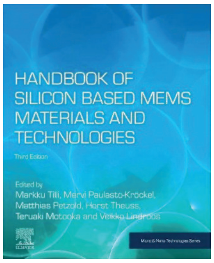

Publisher: Elsevier
3rd ed., April 2020
ISBN: 978-0-12-817786-0
1026 pages
Softcover
Available also as an eBook

3D Printing in Chemical Sciences
Applications Across Chemistry

The authors of this book have attempted to cover as much of the recent research as possible to demonstrate the impact of 3D printing within the chemical sciences. First, they briefly introduce 3D printing and 3D printing techniques, namely stereolithography, selective laser sintering and melting, inkjet printing and fused deposition modelling. Two chapters then describe 3D printing of micro-fluidic and macro-fluidic devices and 3D-printed analytical detectors, including the smartphone optical-sensing platforms, flow-cells for mixing, reaction and detection, electrochemical detector cells and printed electrodes. The following chapters bring an overview of 3D printing in analytical chemistry, pharmaceutical chemistry, biochemistry, synthetic chemistry and physical chemistry. The last chapter presents 3D printing in different areas of chemical education. The authors also discuss the related properties of materials for 3D printing – their biocompatibility, as well as chemical and thermal stability.

Authors: Vipul Gupta, Pavel Nesterenko, Brett Paull

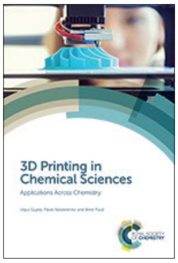

Publisher: Royal Society of Chemistry
1st ed., April 2019
ISBN: 978-1-78801-440-3
250 pages
Hardcover
Available also as an eBook

Bookshelf

Academic dissertations

Device Patterning, Contact, Transport, and Light Emission of Halide Perovskite

To address the issues preventing commercial applications of halide perovskite in optoelectronics, the research work within this thesis comprised the fundamental study on its orthogonal patterning, metal contact, carrier transport and light emission stability. After introducing the background on perovskite technology, the dissertation presents the experimental methods employed for perovskite synthesis, perovskite device fabrication, material and morphology characterisation, as well as the other experimental work. The following four chapters then discuss the results of individual studies. The first one describes an orthogonal electron beam lithography process enabling to fabricate halide perovskite nanodevices. Based upon the examination of the chemical orthogonality of 12 solvents on $CH_3NH_3PbBr_3$ and $(C_6H_5C_2H_4NH_3)_2PbI_4$, i.e. the 3D and 2D single-crystal perovskites, chlorobenzene was utilised to dissolve the poly(methyl methacrylate) resist layer and hexane to clean the samples without degrading the perovskites. A stable 2D perovskite single-crystal photodetector with the channel length of 380 nm was successfully fabricated. In the second experiment, 3D perovskite single crystals with different metal electrodes were prepared to study the transport behaviour at the metal–semiconductor contact interface. It was found that the current injection follows thermionic emission theory, and the Schottky barrier heights for Au, Pt and Ti were determined. The third study gained further insight into the carrier transport behaviour of the bulk perovskite single crystal thanks to a direct measurement using the transfer length method. Finally, highly stable perovskite nanowires for colour-tunable luminescence were fabricated in the nanopores of anodic aluminium oxide substrate using an inkjet printing technique. The photoluminescence operation lifetime of 250 h (19 % degradation) and long-term stability of 100 days (30 % degradation) were achieved.

Doctoral thesis – Summary

Author:
Chun-Ho Lin

Speciality field:
Electrical Engineering

Supervisor:
Jr-Hau He

Defended:
29 January 2019, King Abdullah
University of Science and Technology,
Computer, Electrical and Mathematical
Sciences and Engineering Division
Thuwal, Kingdom of Saudi Arabia

Contact:
chunho.lin@kaust.edu.sa

Coffee-Ring-Effect Based Self-Assembly Mechanism for All-Inkjet Printed Organic Field Effect Transistors With Micron-Sized Channel Length

This thesis, focused on organic field-effect transistors, aimed to minimise the channel length in order to enhance the transistor performance beyond the limits given by the resolution normally achieved in the field of printed electronics. The work tested several possible fabrication routes utilising solution-processed organic materials and based solely on printing and then systematically investigated the influencing factors to optimise the selected approach, which employs the coffee-ring effect to form small hydrophobic twin-lines from printed nanoparticle dispersions.

The first part introduces the topic, provides an overview of related methods and mechanisms, as well as the current knowledge in the field, and then describes the preliminary experiments towards the fabrication of a small-gap electrode. The tested methods included the spontaneous gap formation at contact line proximity during sintering and four methods based on dewetting on thin lines, employing boundary definition by a solvent with a high

Doctoral thesis – Summary

Author:
Chadha Bali

Speciality field:
Functional Inkjet Printing

Supervisors:
Arved Carl Hübler
Ulrich Sigmar Schubert

Defended:
18 June 2019, TU Chemnitz,
Mechanical Engineering, Institute for
Print and Media Technology
Chemnitz, Germany

Contact:
chadha.bali@outlook.com

boiling point, spontaneous gap definition between a liquid contact line and nanoparticles, and dewetting on thin solid lines created either by the slip-stick-motion or by the coffee-ring effect. Based on the overall feasibility and effectivity in terms of time and costs, further work was focused on the last-mentioned one. The development of a theoretical model for twin-line deposition comprised calculation of the deposit ring volume, considering the layout and material parameters, two methods of calculation of the rivulet width, and geometric approximations of the deposit ring cross-section using triangular and circular models. The resulting models were used in single parameter simulations, which included the influence of the number of lines, line length, concentration, drop volume and contact angle. Building upon these findings, the second part deals with the main experiments. After introducing the materials and techniques used, the dissertation describes printing of multiple-droplet line structures to achieve hydrophobic twin-lines and evaluates the practical relevance of the developed model, summarising the influence of material choices and experimental parameters on the fabricated electrodes. Finally, the fabrication of small-channel organic field-effect transistors is presented. Here, also the optimisation of dielectric and semiconductor layers deposition and comparison of different electrode configurations are discussed.

Doctoral thesis – Summary

Studies on Sheet Metal Printing for Metal Packaging

Author:
Stephan Behnke

Speciality field:
Sheet metal printing

Supervisors:
Edgar Dörsam
Peter Groche

Defended:
16 October 2019, Technical University of Darmstadt, Department of Mechanical Engineering, Institute of Printing Science and Technology
Darmstadt, Germany

Language:
German

Original title:
Untersuchungen zum Blechdruck für Metallverpackungen

Contact:
stephan.behnke@web.de

The primary goal of this thesis was to streamline the production of decorated metal packaging, which typically requires several runs and separate machines for varnishing and printing. To enable direct printing with UV-curable inks, the research involved the investigation of surface properties of tinplate and their modification using UV pretreatment to increase the ink adhesion. One of the objectives also was to study the influence of post-processing to take into account the stress during forming.

The dissertation introduces the topic and metal packaging, summarising its types, manufacturing, structure and required properties with a focus on the three-piece design. It also describes the substrate and coating materials, their drying or curing and surface properties, as well as the production lines used for decoration. Three chapters then present the experiments and their results. The work employed the methods for characterisation of wetting and adhesion, X-ray photoelectron spectroscopy to analyse the organic compounds present on a tinplate surface before and after the pretreatment, as well as the methods for characterising formability and other properties. First, 13 different tinplates were printed with a UV-curable white ink specially formulated for this experiment. In the next step, six ink compositions from the same producer were tested with five selected tinplates. On the basis of these results, the ink formulation was further optimised and three ink compositions were used in the laboratory study on formability to test the influence of the mechanical deformation stresses occurring during the post-processing with regard to ink adhesion on five types of tinplate. The impact of sterilization was also investigated. The following experiments with one ink and four tinplates then examined the effect of different pretreatment processes (five methods of UV treatment, thermal treatment, atmospheric-pressure plasma treatment) on wetting and adhesion. Finally, the pretreatment using the xenon excimer lamp (172 nm) was further investigated. The influence of the materials used, the formability test methods and the photochemical mechanisms of UV pretreatment are thoroughly discussed, as well as the resulting line configuration, which allows complete printing and varnishing of tinplate within two runs.

Events

NANOTEXNOLOGY 2020

nano texnology

Thessaloniki, Greece
4–11 July 2020

This year, the organisers offer both live and virtual event, according to participants' preferences and possibilities. All three weekend days that frame the programme are reserved for the 14th International Summer Schools on Nanosciences & Nanotechnologies, Organic Electronics and Nanomedicine, with the courses mostly in virtual mode. The sessions of the 17th International Conference on Nanosciences & Nanotechnologies are scheduled for the whole workweek and opened by the Thomas Webster's keynote 'Nanomedicine and COVID-19: commercializing improved prevention, diagnostic, and therapeutic approaches'. The 3rd International Conference on 3D Printing, 3D Bioprinting, Digital & Additive Manufacturing is organised in the scope of two EU-funded Horizon 2020 projects, SMARTLINE – Smart in-line metrology and control for boosting the yield and quality of high-volume manufacturing of organic electronics, and CORNET – Multiscale modelling and characterization to optimize the manufacturing processes of organic electronics materials and devices. Its Wednesday sessions deal with bioprinting, advanced materials, such as the phosphorescent bio-based resin, characterisation of their properties, and more. Four days of the 13th International Symposium on Flexible Organic Electronics include the keynotes 'Molecular switches at interfaces and in junctions: a theoretical perspective' by Jerome Cornil, 'Emissive and charge-generating donor–acceptor interfaces for organic optoelectronics with low voltage losses' by Koen Vandewal, 'Using molecular doping to enhance the performance of organic optoelectronics' by Thomas D. Anthopoulos, 'Hybrid perovskite crystallization: from in-situ diagnostics to robotic experimentation' by Aram Amassian. The plenary session of the event features Norbert Koch on 'Controlling hybrid inorganic/organic electronic materials interfaces' and Joachim P. Spatz with a lecture 'Matter-to-life: how to build a cell'.

High-Performance Graphics 2020

https://www.highperformancegraphics.org
13–16 July 2020

High-Performance Graphics 2020
July 13-16, hosted online

As many of the events taking place in these months, also this conference in computer graphics is held as a fully virtual event, with the video streams freely available online. Online interactions with speakers are possible after registration (for a small fee). Among the keynotes, Chris Wyman reviews real-time ray tracing and lighting algorithms, while system-level challenges of hardware-accelerated real-time ray tracing are addressed by Holger Gruen; further, Yaser Sheikh describes the early steps towards achieving photorealistic telepresence, Wenzel Jakob discusses differentiable rendering and Manolis Savva 3D graphics systems for simulation. The technical papers deal with high-performance and special rendering, image-based computing, hardware architectures, and more.

Further changes in the calendar of events for 2020

From the events that were originally scheduled earlier this year, the Inkjet Ink Characterisation Practical Course will take place in Hamburg, Germany on 13–16 October 2020 and the FuturePrint fair in São Paulo, Brazil on 24–27 November 2020. The new date still has not been set for the 33rd International Publishers Congress in Lillehammer, Norway, the Printed Electronics Europe in Berlin, Germany, and the CPES2020 conference in Brampton, Ontario, Canada, among others.

Because the COVID-19 situation remains serious in several places worldwide and the restrictions are lifted only to some extent in many countries, almost all events that were planned for the third quarter of 2020 are also impacted.

One of the events fully cancelled for this year is the 47th International iarigai Conference that was to be hosted by Clemson University in Greenville, South Carolina, USA. As the 2021 annual conference should be held in Greece, Clemson University will probably host the next conference in 2022. Other events rescheduled to the next year include the Labelexpo Americas and Brand Print Americas shows (23–25 March 2021 in Chicago, Illinois, USA), the Unique 4 + 1 fair (4–6 September 2021 in Leipzig, Germany), another two co-located events, The Print Show and The Sign Show in Birmingham, UK (28–30 September 2021), and the 11th International Conference on Flexible and Printed Electronics (ICPFE, to be held from 28 September to 1 October 2021 in Niigata, Japan). The Print Event in Minneapolis, Minnesota, USA, the 6th Digital Textile Congress in Ghent, Belgium and the 12th Image Processing and Communications conference in Bydgoszcz, Poland belong to those with a date yet to be announced.

PRINTING United Alliance Events

A series of the Color Management Boot Camps, organised originally by SGIA and now by the PRINTING United Alliance, take place during July and August 2020 as the online workshops conducted by certified instructors.

WAN-IFRA Events

The July events start with the two supported by the Google News Initiative – the webinar presenting the data-driven journalism skills on 2 July and the briefing on Round 2 of the 12-month programme for local and regional news publishers, Table Stakes Europe, on 8 July. The 2020 editions of the Asian Media Leaders Summit (20–23 July) and LATAM Media Leaders eSummit for Latin America (27–29 July) are then organised also as virtual events, discussing the decline in advertising revenues, post-COVID media outlook along with the appropriate business and editorial strategies.

In September, an online edition of Digital Media Africa 2020 is organised (8–9 September), with free registration and the African Digital Media Awards on the first day. Later, several Indian events are held online as well: the 28th annual conference WAN-IFRA India 2020 Printing Summit and the Future of News Summit (21–22 September), followed by the Indian Media Leaders eSummit (23–24 September).

IEEE VLSI DCS 2020
2nd International Conference on VLSI Device, Circuit and System

http://site.ieee.org/sb-msitceds
18–19 July 2020

A wide range of topics covered by this event dedicated to VLSI (very large-scale integration) technology include also the flexible, printed, large-area and organic electronics, advanced nanomaterials and emerging devices.

CGDIP 2020
4th International Conference on Computer Graphics and Digital Image Processing

https://www.cgdip.org
24 July 2020

While originally planned as a three-day event held jointly with the Workshop on Applications and Technologies of Computer Vision, the 2020 edition had to be eventually transformed to the online conference organised during one day. Among the speakers, Paul Craig has the invited lecture presenting the research investigating how information visualisation could be better supported on mobile devices and demonstrating the potential of information visualisation techniques to make even larger-scale data more accessible for mobile device users and users in multi-device environments.

CIE Tutorials on Colorimetry and Visual Appearance

http://cie.co.at
28–29 July 2020

This summer, the International Commission on Illumination (CIE) offers the set of 19 tutorials, with the pre-recorded presentations available for viewing from 17 July and the opportunity to submit questions to be answered during the live question and answer sessions – those for CIE colorimetry and 3D printing on 28 July and those dealing with the measurement of advanced BRDF (Bidirectional Reflectance Distribution Function), sparkle and graininess on 29 July. The registered participants also receive a bundle of five CIE publications on the tutorial topics and have an option to acquire another one at a substantially discounted price.

Four 30-minute colorimetric tutorials include the introduction to CIE colorimetry, explaining the main concepts. The other topics deal with colorimetric representations based on cone fundamentals, spectra of typical LED lamps together with an explanation why one LED-illuminant is under study to complement the CIE standard illuminant A for calibration use in photometry, and the CIE 2017 Colour Fidelity Index.

In connection with 3D printing, besides a brief introduction of the research strategy for measurement and reproduction of 3D objects, four 20-minute tutorials cover the recent development of 3D colour printing technologies and colour appearance reproduction, the image-based colour measurement for 3D objects and factors that affect its accuracy, assessing chromatic adaptation in a 3D scene, and colour difference evaluation for 3D-printed objects.

From five tutorials on BRDF, three 20-minute ones explain the basics of reflectance and BRDF measurements, polarisation effects in BRDF measurement and an approach to BRDF measurement in the area of the specular peak; the other two present the use and challenges of BRDF measurement in automotive and cosmetic industries, each in 15 minutes.

The last set of tutorials includes a brief description of the physics behind sparkle and graininess, the evolution of automotive coatings and the challenge of texture measurements, characterisation of visual texture by reflectance measurements, and the design of experiment for visual assessment of sparkle and graininess (in 20 or 25 minutes).

FLEPS 2020
IEEE International Conference on Flexible and Printable Sensors and Systems

https://2020.ieee-fleps.org/
16–19 August 2020

This event organised by the Institute of Electrical and Electronics Engineers also had to be transformed into a virtual meeting for its 2nd edition. The keynote speakers feature Joseph Wang, sharing his deep insight into the flexible printable bioelectronics devices from wearable biosensors to on-body biofuel cells, John Rogers, presenting the soft electronic and microfluidic systems for the skin enabled by the recent advances in materials and technology, with specific examples in wireless monitoring for neonatal intensive care and capture, storage and biomarker analysis of sweat, and Richard Price, demonstrating the potential for innovations with low-cost, smart and flexible electronic objects. The topics of the invited talks are 'Sustainable sensor solutions through printed and hybrid manufacturing' by Maria Smolander, 'Inkjettable, polydimethylsiloxane based soft electronic' by Matti Mäntysalo, 'Emerging sustainable sensors based on nanostructures on flexible and disposable substrates' by Magnus Willander, 'Ultra-low power on skin ECG using RFID communication' by John Batchelor, 'Variation-tolerant digital circuit design for printed/flexible electronics' by Joseph Chang, 'Advancing the sense of touch for collaborative robots' by Kaspar Althoefer, and 'TFT-based IP cores for flexible electronic applications' by Kris Myny.

Further, besides the contributed lectures and posters, the programme offers six 90-minute tutorial presentations, dealing with component integration and product design for printable electronics, a pathway to ubiquitous electronic sensing using printed electronics from nanomaterials, current trends and outlook for wearable electronics and e-textile, materials and technologies for flexible and printed IoT sensors, materials, devices and applications for organic narrowband photodetectors, and technology, materials and selected applications for 3D printing.

SIGGRAPH 2020
The 47th International Conference & Exhibition on Computer Graphics & Interactive Techniques

https://s2020.siggraph.org/
17–28 August 2020

This year organised as a virtual two-week event, SIGGRAPH 2020 held by a special interest group of the Association for Computing Machinery (ACM) traditionally offers the rich programme aiming to present the most transformative advancements in the field. The participants can join workshops, beginner and expert courses, production sessions, panel discussions, presentations of emerging technologies and interactive projects as well as scientific contributions, Frontiers Talks highlighting problems where the ACM SIGGRAPH's expertise can help create solutions, the awards recognising exceptional achievements in computer graphics and interactive techniques, the ACM SIGGRAPH Student Research Competition, Educator's Forum, the Job Fair, and much more. Marco Tempest is announced as a keynote speaker with a virtual presentation combining mixed reality, storytelling, gestural sensing and swarm robotics.

XVI Color Conference

https://gruppodelcolore.org
3–4 September 2020

XVI COLOR CONFERENCE
September 3rd-4th 2020

In 2020, the conference is held as a virtual event with a significant reduction in the registration fees. The programme includes many contributions in English or Italian concerning a wide range of aspects of colour and light.

The topics are, for example, the Euclidean colour-difference formula for small to medium colour differences in the log-compressed OSA-UCS space, geometric models of colour perception, colorimetric and material analysis of surfaces, a novel hyperspectral imaging system, identification of natural dyes through fibre optic reflectance spectroscopy and hyperspectral imaging techniques, colours in marketing education, the contribution of black colour to visual rhetoric of packaging, a systematic bibliographic review into colour psychology, a test on colour discrimination in complex scenes towards a wider understanding of colour blindness, etc.

FMTX 2020
Future Manufacturing Technologies

https://www.fmtexpo.org/
16 September 2020

For its 2nd edition, the joint FMTX conference and expo had to be rescheduled and changed to an online event. The programme offers the plenary talks on digital transformation and sophisticated analytics enabled by connecting to all data sources to acquire real-time data, panel discussions on the challenges of creating the connected factory of the future and empowering the workforce of tomorrow, 3D Printing Live Stage with sessions on industrialisation, advanced materials, quality assurance and testing, and more.

FESPA Events

For September 2020, only one FESPA print and signage show is currently scheduled: the FESPA Africa exhibition taking place in Johannesburg, South Africa (9–11 September) and co-located with Sign Africa, Africa Print, Africa LED and the Modern Marketing Expo. The FESPA Brasil event held in São Paulo and normally organised a half year earlier was at first postponed to September but eventually its 2020 edition had to be cancelled.

Packaging Events by EasyFairs

The 18th edition of Empack is announced for 15–17 September 2020 in Utrecht, The Netherlands. The event dedicated to premium packaging, Packaging Innovations & Luxury Packaging, is held in London, UK one week later (23–24 September 2020).

20th International Coating Science and Technology Symposium

Minneapolis, Minnesota, USA
20–23 September 2020

The announced programme of this event features also the session focused on printing, with contributions dealing with hybrid manufacturing of high-resolution and high-performance metal conductors on plastic substrates and the study of pressure and shear stress distribution of drop impact, for example.

12th 3D Printing Days

Kielce, Poland
22–24 September 2020

This Polish exhibition for 3D printing also hosts manufacturers and distributors representing 3D scanning industry and rapid prototyping sector.

SPIE Optics & Photonics 2020

https://spie.org
24–28 August 2020

As each other SPIE Digital Forum, this one is also freely accessible via the SPIE Digital Library online platform that brings live plenary presentations and on-demand technical talks; it also enables collaboration with exhibiting companies and connecting with colleagues through online networking events. The plenary session on Organic Photonics + Electronics is scheduled for 25 August. It starts with a presentation on quantum dots by Changhee Lee, discussing especially the technical challenges and development opportunities of inkjet-printed QLED displays. The second lecture by Karl Leo reviews the key features of solid-state organic solar cells and recent progress in the field along with the remaining challenges hindering the achievement of broad commercial impact, discussing the main aspects important for mass production and possible application scenarios. The last presentation by Niyazi S. Sariciftci then stresses how important is to use environmentally friendly materials as the organic electronic devices are maturing from the academic research into the industrial development, presenting the advances in bio-organic materials. Furthermore, the lecture presents the bio-organic systems that utilise enzymes immobilised on graphene.

Across individual conferences, the contributions employing printing technology include the invited talks on printed transistors for ocean sensing and on the commercialisation of QLEDs with their inkjet printing manufacturing, as well as the papers dealing with 3D-printed computer-generated volume holograms, printable thermally activated delayed fluorescence polymer light-emitting diode, perovskite solar cells with all-inkjet-printed absorber and extraction layers, a novel transfer printing approach for solution-processable perovskite heterostructures, fully printed flexible perovskite photodetector arrays, formation of highly crystalline organic semiconductor thin films by inkjet printed thickness gradients, and more.

London Imaging Meeting 2020

http://www.imaging.org
30 September to 1 October 2020

This new topic-based conference in imaging science, being launched this year and originally scheduled for April, had to be postponed and transformed into the online format. The theme for 2020 is “Future Colour Imaging”. The 90-minute pre-conference workshop on the first morning provides background on colour theory and discusses its relationship to the in-camera processing pipeline and imaging applications. The conference programme offers two keynote presentations – ‘Surface color perception in realistic scenes: previews of a future color science’ by Laurence Maloney and ‘Designing cameras to detect the “invisible”: towards domain-specific computational imaging’ by Felix Heide. The sessions deal with the visibility, colour science and applications, perception, image reproduction and computer vision. The announced topics of the corresponding focal talks are focused on imaging the visible beyond RGB (Jon Hardeberg), the recent developments on colour science (Ronnier Luo), perception (Hannah Smithson), the challenges, solutions and applications for graphical 3D printing (Philipp Urban), and image quality assessment based on convolutional neural networks (Raimondo Schettini).

Journal of
Print and Media Technology
Research
A PEER-REVIEWED QUARTERLY

ISSN 2414-6250 (Online)
ISSN 2223-8905 (Print)
CODEN JPMTBI
UDC 665

Call for papers

The Journal of Print and Media Technology Research is a peer-reviewed periodical, published quarterly by iarigai, the International Association of Research Organizations for the Information, Media and Graphic Arts Industries.

JPMTR is listed in Emerging Sources Citation Index, Scopus, Index Copernicus International, PiraBase (by Smithers Pira), Paperbase (by Innventia and Centre Technique du Papier), NSD – Norwegian Register for Scientific Journals, Series and Publishers.

Authors are invited to prepare and submit complete, previously unpublished and original works, which are not under review in any other journals and/or conferences.

The journal will consider for publication papers on fundamental and applied aspects of at least, but not limited to, the following topics:

- **Printing technology and related processes**
  Conventional and special printing; Packaging; Fuel cells, batteries, sensors and other printed functionality; Printing on biomaterials; Textile and fabric printing; Printed decorations; 3D printing; Material science; Process control
- **Premedia technology and processes**
  Colour reproduction and colour management; Image and reproduction quality; Image carriers (physical and virtual); Workflow and management
- **Emerging media and future trends**
  Media industry developments; Developing media communications value systems; Online and mobile media development; Cross-media publishing
- **Social impact**
  Environmental issues and sustainability; Consumer perception and media use; Social trends and their impact on media

Submissions for the journal are accepted at any time. If meeting the general criteria and ethic standards of scientific publishing, they will be rapidly forwarded to peer-review by experts of relevant scientific competence, carefully evaluated, selected and edited. Once accepted and edited, the papers will be published as soon as possible.

There is no entry or publishing fee for authors. Authors of accepted contributions will be asked to sign a copyright transfer agreement.

Authors are asked to strictly follow the guidelines for preparation of a paper (see the abbreviated version on inside back cover of the journal).

Complete guidelines can be downloaded from: <http://www.iarigai.org/publications/journals/>
Papers not complying with the guidelines will be returned to authors for revision.

Submissions and queries should be directed to: journal@iarigai.org

Journal of
Print and Media Technology
Research
A PEER-REVIEWED QUARTERLY

Vol. 9, 2020

Prices and subscriptions

Since 2016, the journal is published in digital form; current and archive issues are available at: <https://iarigai.com/publications/journals/>.

Since 2020, the journal will be published as "open access" publication, available free of charge for iarigai members, subscribers, authors, contributors and all other interested public users.

A print version is available on-demand. Please, find below the prices charged for the printed Journal, for four issues per year as well as for a single issue

Regular prices

Four issues, print JPMTR (on-demand)	400 EUR
Single issue, print JPMTR (on-demand)	100 EUR

Subscription prices

Annual subscription, four issues, print JPMTR (on-demand)	400 EUR

Prices for iarigai members

Four issues, print JPMTR (on-demand)	400 EUR
Single issue, print JPMTR (on-demand)	100 EUR

Place your order online at: <http://www.iarigai.org/publications/subscriptions-orders/>
Or send an e-mail order to: office@iarigai.org

Guidelines for authors

Authors are encouraged to submit complete, original and previously unpublished scientific or technical research works, which are not under reviews in any other journals and/or conferences. Significantly expanded and updated versions of conference presentations may also be considered for publication. In addition, the Journal will publish reviews as well as opinions and reflections in a special section.

Submissions for the journal are accepted at any time. If meeting the general criteria and ethical standards of the scientific publication, they will be rapidly forwarded to peer-review by experts of high scientific competence, carefully evaluated, and considered for selection. Once accepted by the Editorial Board, the papers will be edited and published as soon as possible.

When preparing a manuscript for JPMTR, please strictly comply with the journal guidelines. The Editorial Board retains the right to reject without comment or explanation manuscripts that are not prepared in accordance with these guidelines and/or if the appropriate level required for scientific publishing cannot be attained.

A – General

The text should be cohesive, logically organized, and thus easy to follow by someone with common knowledge in the field. Do not include information that is not relevant to your research question(s) stated in the introduction.

Only contributions submitted in English will be considered for publication. If English is not your native language, please arrange for the text to be reviewed by a technical editor with skills in English and scientific communications. Maintain a consistent style with regard to spelling (either UK or US English, but never both), punctuation, nomenclature, symbols etc. Make sure that you are using proper English scientific terms. Literal translations are often wrong. Terms that do not have a commonly known English translation should be explicitly defined in the manuscript. Acronyms and abbreviations used must also be explicitly defined. Generally, sentences should not be very long and their structure should be relatively simple, with the subject located close to its verb. Do not overuse passive constructions.

Do not copy substantial parts of your previous publications and do not submit the same manuscript to more than one journal at a time. Clearly distinguish your original results and ideas from those of other authors and from your earlier publications – provide citations whenever relevant.

For more details on ethics in scientific publication consult Guidelines, published by the Committee on Publication Ethics (COPE):
<https://publicationethics.org/resources/guidelines>

If it is necessary to use an illustration, diagram, etc. from an earlier publication, it is the author's responsibility to ensure that permission to reproduce such an illustration, diagram, etc. is obtained from the copyright holder. If a figure is copied, adapted or redrawn, the original source must be acknowledged.

Submitting the contribution to JPMTR, the author(s) confirm that it has not been published previously, that it is not under consideration for publication elsewhere and – once accepted and published – it will not be published under the same title and in the same form, in English or in any other language. The published paper may, however, be republished as part of an academic thesis to be defended by the author. The publisher retains the right to publish the printed paper online in the electronic form and to distribute and market the Journal containing the respective paper without any limitations.

B – Structure of the manuscript

Preliminary

Title: Should be concise and unambiguous, and must reflect the contents of the article. Information given in the title does not need to be repeated in the abstract (as they are always published jointly), although some overlap is unavoidable.

List of authors: I.e. all persons who contributed substantially to study planning, experimental work, data collection or interpretation of results and wrote or critically revised the manuscript and approved its final version. Enter full names (first and last), followed by the present address, as well as the E-mail addresses. Separately enter complete details of the corresponding author – full mailing address, telephone number, and E-mail. Editors will communicate only with the corresponding author.

Abstract: Should not exceed 500 words. Briefly explain why you conducted the research (background), what question(s) you answer (objectives), how you performed the research (methods), what you found (results: major data, relationships), and your interpretation and main consequences of your findings (discussion, conclusions). The abstract must reflect the content of the article, including all keywords, as for most readers it will be the major source of information about your research. Make sure that all the information given in the abstract also appears in the main body of the article.

Keywords: Include three to five relevant scientific terms that are not mentioned in the title. Keep the keywords specific. Avoid more general and/or descriptive terms, unless your research has strong interdisciplinary significance.

Scientific content

Introduction and background: Explain why it was necessary to carry out the research and the specific research question(s) you will answer. Start from more general issues and gradually focus on your research question(s). Describe relevant earlier research in the area and how your work is related to this.

Methods: Describe in detail how the research was carried out (e.g. study area, data collection, criteria, origin of analyzed material, sample size, number of measurements, equipment, data analysis, statistical methods and software used). All factors that could have affected the results need to be considered. Make sure that you comply with the ethical standards, with respect to the environmental protection, other authors and their published works, etc.

Results: Present the new results of your research (previously published data should not be included in this section). All tables and figures must be mentioned in the main body of the article, in the order in which they appear. Make sure that the statistical analysis is appropriate. Do not fabricate or distort any data, and do not exclude any important data; similarly, do not manipulate images to make a false impression on readers.

Discussion: Answer your research questions (stated at the end of the introduction) and compare your new results with published data, as objectively as possible. Discuss their limitations and highlight your main findings. At the end of Discussion or in a separate section, emphasize your major conclusions, pointing out scientific contribution and the practical significance of your study.

Conclusions: The main conclusions emerging from the study should be briefly presented or listed in this section, with the reference to the aims of the research and/or questions mentioned in the Introduction and elaborated in the Discussion.

Note: Some papers might require different structure of the scientific content. In such cases, however, it is necessary to clearly name and mark the appropriate sections, or to consult the editors. Sections from Introduction until the end of Conclusions must be numbered. Number the section titles consecutively as 1., 2., 3., ... while subsections should be hierarchically numbered as 2.1, 2.3, 3.4 etc. Only Arabic numerals will be accepted.

Acknowledgments: Place any acknowledgements at the end of your manuscript, after conclusions and before the list of literature references.

References: The list of sources referred to in the text should be collected in alphabetical order on at the end of the paper. Make sure that you have provided sources for all important information extracted from other publications. References should be given only to documents which any reader can reasonably be expected to be able to find in the open literature or on the web, and the reference should be complete, so that it is possible for the reader to locate the source without difficulty. The number of cited works should not be excessive - do not give many similar examples.

Responsibility for the accuracy of bibliographic citations lies entirely with the authors. Please use exclusively the Harvard Referencing System. For more information consult the Guide to Harvard style of Referencing, 6th edition, 2019, used with consent of Anglia Ruskin University, available at:
<https://libweb.anglia.ac.uk/referencing/files/Harvard_referencing_201718.pdf>

C – Technical requirements for text processing

For technical requirement related to your submission, i.e. page layout, formatting of the text, as well of graphic objects (images, charts, tables etc.) please see detailed instructions at:
<http://www.iarigai.org/publications/journals/>

D – Submission of the paper and further procedure

Before sending your paper, check once again that it corresponds to the requirements explicated above, with special regard to the ethical issues, structure of the paper as well as formatting.

Once completed, send your paper as an attachment to:
journal@iarigai.org

If necessary, compress the file before sending it. You will be acknowledged on the receipt within 48 hours, along with the code under which your submission will be processed.

The editors will check the manuscript and inform you whether it has to be updated regarding the structure and formatting. The corrected manuscript is expected within 15 days.

Your paper will be forwarded for anonymous evaluation by two experts of international reputation in your specific field. Their comments and remarks will be in due time disclosed to the author(s), with the request for changes, explanations or corrections (if any) as demanded by the referees.

After the updated version is approved by the reviewers, the Editorial Board will decide on the publishing of the paper. However, the Board retains the right to ask for a third independent opinion, or to definitely reject the contribution.

Printing and publishing of papers, once accepted by the Editorial Board, will be carried out at the earliest possible convenience.

2-2020

Journal of Print and Media Technology Research

A PEER-REVIEWED QUARTERLY

The journal is publishing contributions in the following fields of research

- Printing technology and related processes
- Premedia technology and processes
- Emerging media and future trends
- Social impacts

For details see the Mission statement inside

JPMTR is listed in

- Emerging Sources Citation Index
- Scopus
- Index Copernicus International
- PiraBase (by Smithers Pira)
- Paperbase (by Innventia and Centre Technique du Papier)
- NSD – Norwegian Register for Scientific Journals, Series and Publishers

Submissions and inquiries

journal@iarigai.org

Subscriptions

office@iarigai.org

More information at

www.iarigai.org/publications/journal

Publisher

The International Association of Research Organizations
for the Information, Media and Graphic Arts Industries
Magdalenenstrasse 2
D-64288 Darmstadt
Germany